Parallel 3-D Method of Characteristics with Linear Source and Advanced Transverse Integration

by

Andrew P. Fitzgerald

A dissertation submitted in partial fulfillment
of the requirements for the degree of
Doctor of Philosophy
(Nuclear Engineering and Radiological Sciences)
in the University of Michigan
2019

Doctoral Committee:

Professor Thomas Downar, Co-Chair,
Dr. Brendan Kochunas, Co-Chair,
Professor Edward Larsen,
Professor Venkat Raman,

apfitzge@umich.edu
ORCID ID: 0000-0002-4066-0949

2019

TABLE OF CONTENTS

List of Algorithms

LIST OF APPENDICES

LIST OF ABBREVIATIONS

MoC Method of Characteristics

FS Flat Source

LS Linear Source

FSA flat-source approximation

LSA linear-source approximation

FSMoC flat-source method of characteristics

LSMoC linear-source method of characteristics

LIFA linear isotropic flat anisotropic

CASL Consortium for the Advanced Simulation of Light Water Reactors

LWR Light Water Reactor

NEAMS Nuclear Energy Advanced Modeling and Simulation Program

PDE Partial Differential Equation

ODE Ordinary Differential Equation

P_N Spherical Harmonics

CP Collision Probability

CDP method of Characteristic Direction Probabilities

S_N Discrete Ordinates

NDA non-linear diffusion acceleration

CMFD coarse mesh finite-difference

T/H thermal-hydraulic

TCP0 transport-corrected P_0

DNPL direct neutron path linking

MRMB memory reduction technique for macroband

MRT modular ray-tracing

LEAF Legendre polynomial expansion of angular flux

VERA Virtual Environment for Reactor Analysis

UO_2 UO_2

CPU central processing unit

GPU graphics processing unit

GPGPU general purpose graphics processing unit

RSB recursive spectral bisection

RIB recursive intertial bisection

REB recursive expansion bisection

SOI sphere of influence

ABSTRACT

In the design and analysis of nuclear fission reactor systems, simulations are an essential tool for improving efficiency as well as safety. Neutronics simulations have always been limited by the available computational resources. This is because of the large discretizations that are needed for the neutron transport equation, which has a 6-dimensional phase space for steady-state eigenvalue problems.

The "gold standard" for 3-D neutron transport simulations is Monte Carlo with explicit geometry representation because it treats all dependent variables continuously. However, there are significant remaining challenges for Monte Carlo methods that prohibit their widespread use, and put them at a disadvantage compared to deterministic methods. The "gold standard" for deterministic 3-D neutron transport is the 3-D Method of Characteristics (MoC). Numerous deterministic methods exist for solving the 3-D transport equation. Each of them has their own drawback. 3-D MoC is considered the "best" due to its ability to accurately model the exact geometry and neutron scattering physics (other methods do just one of these well or become undesirably complex). The downside of the 3-D MoC method is the substantial computational resources required to discretize the problem.

In 2-D, MoC solutions of the transport equation are the preferred method for reactor applications because:

- they can model the geometry exactly
- they easily accommodate much of the desired physics
- their implementation on a computer is one of the most efficient and often the fastest
- the method is highly parallelizable

The MoC method for neutron transport, first converts the transport equation (a PDE) to an ODE in terms of the "characteristic" dependent variable (a combination of space and direction of flight). As a consequence, MoC methods have a unique discretization that requires discretization of the "characteristic" variable in addition to the usual spatial variables. The discretization of the characteristics (commonly called rays) involves tracking rays through the spatial mesh and computing the lengths of the segments made by the intersections of the rays with the spatial mesh. Then for each segment the solution of the transport equation is evaluated. These solutions are then ultimately integrated to compute the engineering figures of merit.

Over the past decade, there has been renewed interest in assessing the state of the art for 3-D MoC and the tractability of this problem on the newest computer architectures. Previous work made significant strides in parallelizing the MoC algorithm for 100,000's of processors, but ultimately did not prove viable due to the extreme compute resources required. Since then there has been progress in making 3-D MOC a less computationally burdensome by adopting more advanced discretization methods that overall, lead to fewer spatial mesh regions and rays; namely the linear source approximation, and ray-categorization or on-the-fly ray-tracing.

The goal of this thesis is to continue progress in reducing the burden of 3-D MoC calculations by extending a ray-tracing technique previously used for 2-D MoC calculations: the macroband. The macroband ray-tracing method lays down characteristic tracks in the domain such that transverse integration over these tracks is more accurate. By doing so, the same accuracy can be achieved with fewer rays, and thus less computational work. It has been observed in 2-D calculations that the average distance between rays can be increased by up to 5 times (3-5 times fewer rays). In 3-D, the average distance between rays is expected to be increased in both axial and radial directions leading to 9-25 times fewer rays overall.

The macroband approach also offers several more advantages compared to traditional "modular" ray-tracing methods. In modular ray-tracing methods the discretization of the angular variable via a quadrature is slightly perturbed to guarantee rays are aligned at certain geometric interfaces. This angular perturbation has not been observed to cause significant error in 2-D calculations, but for 3-D it has, meaning more discrete angles are required to obtain an accurate result. The macroband approach does not suffer from this because rays are not forced to be aligned at geometric interfaces, though this does require new approximations be introduced at mesh interfaces. Addi-

tionally, modular ray-tracing techniques require the same density of rays everywhere in the domain. For certain nuclear reactor designs, some components may require a highly resolved discretization in some areas, but not others. Therefore, with modular ray tracing the same fine ray-spacing is necessary everywhere. However, in the macroband approach it is possible to assign a finer ray-spacing only in these special regions, while using a coarser spacing/discretization everywhere else. Both of these advantages are expected to reduce the amount of work compared to traditional MoC ray-tracing techniques and succeed in making the 3-D MoC problem more tractable.

CHAPTER 1

Introduction

1.1 Motivation

Computer simulations have played an important role in the design and analysis of nuclear reactor systems over the past 60 years [1]. The methods used by these simulations have always been limited by the available computational resources; as such, in the 1950's two-group diffusion theory was used as a basis for simulation tools [1]. As computers became more powerful, multi-group diffusion calculations became the method of choice for Light Water Reactor (LWR) design calculations.

More accurate and detailed simulation tools allow for designs to have higher power density, and thus be more profitable, without compromising safety. However, computational resources have always limited the level of detail of simulation tools. Exponential increases in computing power, and high-performance computing clusters have made whole-core transport calculations possible [2–9]. Programs such as Consortium for the Advanced Simulation of Light Water Reactors (CASL) and Nuclear Energy Advanced Modeling and Simulation Program (NEAMS) have focused on development of modern advanced simulation tools to address certain challenge problems. Large computing clusters are generally unavailable to reactor analysts in industry, and so using direct whole-core 3-D transport methods is not common outside academia or national laboratories.

The "gold standard" of deterministic methods has been the 3-D Method of Characteristics (MoC) [10] due to its' ability to exactly model complicated geometries. At the time of writing, whole-core 3-D MoC calculations are generally not possible without use of large computing clusters. This is due to the large discreteizations that are necessary for the neutron transport equation, which has a 6-dimensional phase space for stead-state eigenvalue problems. In the past decade, there has been renewed interest in making 3-D MoC more efficient and performant by using parallelism [11], modern graphics processing unit (GPU) architectures [7], and ray-tracing storage techniques [12, 13]. There has also been work done to make MoC faster by improving the efficiency of the calculations by using higher-order approximations [9, 14].

The bulk of this thesis work is comprised of three distinct, yet connected, topics, all with a focus

on improving the feasibility of 3-D MoC calculations. It is the author's opinion, that improving efficiency of 3-D MoC calculations should be the primary focus of current research, as it is not feasible for industry to use thousands of processors. Thus, two techniques are utilized as part of this thesis work: the linear-source approximation (LSA), and the macroray.

The LSA has been studied by other research groups [9, 14, 15], and has been worked on as part of this thesis project; specifically, this work has led to improvements of the method for stability in near-void regions [16], and efficiency in multi-physics simulations [17]. The LSA is an approximation that is used to improve MoC efficiency by reducing the number of computational cells required for accurate results.

The macroray is a new ray-tracing technique under development as part of this thesis work; this technique is an extension of the two-dimensional macroband [18] ray-tracing technique. This technique has been shown to reduce the number of characteristic rays required for accurate results in two-dimensional flat-source calculations [19, 20]. To the best of the author's knowledge, there have been no studies of this ray-tracing technique in three-dimensional ray-tracing calculations. Fewer characteristic rays results in more efficient calculations; the improvement in efficiency is expected to be more significant in 3-D calculations due to the square scaling of tracks with ray-spacing, rather than linear scaling in 2-D. Additionally, efficiency should be improved further by the Linear Source (LS) which allows for coarser cells and fewer track-segments.

The third contribution of this thesis is work in improving parallel efficiency. While large scale parallelism on thousands of processors may not be feasible for industry, some degree of parallelism is necessary for whole-core calculations due to memory constraints. An automated spatial decomposition scheme based on graph theory, is developed leading to significantly improved parallel efficiency [21, 22].

1.2 Outline

The remainder of this document is structured as follows. Chapter 2 gives an overview of neutron transport theory, with a focus on what is relevant to this work. The derivation and details on the Method of Characteristics (MoC) are provided in Chapter 3, with a focus on the contributions made in this work. Ray-tracing is an important aspect of Method of Characteristics (MoC) calculations, and details about ray-tracing techniques are provided in Chapter 4. Finally, initial results are presented in Chapter 6 with an overview of future work that needs to be done.

CHAPTER 2

Neutron Transport Theory

In this chapter, the basic theory behind the neutron transport equation, and the numerical methods used to solve it are introduced.

2.1 Neutron Transport Equation

The fundamental equation for all neutron transport methods is the neutron transport equation:

$$\begin{aligned}\Big[\frac{1}{v(E)}\frac{\partial}{\partial t} + \widehat{\boldsymbol{\Omega}}\cdot\boldsymbol{\nabla} + \Sigma_t(\boldsymbol{x},E,t)\Big]\psi(\boldsymbol{x},\widehat{\boldsymbol{\Omega}},E,t) = \\ \frac{1}{4\pi}\Bigg[Q(\boldsymbol{x},\widehat{\boldsymbol{\Omega}},E,t) \\ + \int_0^\infty\int_{4\pi}\Sigma_s(\boldsymbol{x},\widehat{\boldsymbol{\Omega}}'\cdot\widehat{\boldsymbol{\Omega}},E'\to E,t)\psi(\boldsymbol{x},\widehat{\boldsymbol{\Omega}}',E',t)\,\mathrm{d}\Omega'\,\mathrm{d}E' \\ + \chi(\boldsymbol{x},E)\int_0^\infty\nu\Sigma_f(\boldsymbol{x},E',t)\int_{4\pi}\psi(\boldsymbol{x},\widehat{\boldsymbol{\Omega}}',E',t)\,\mathrm{d}\Omega'\,\mathrm{d}E'\Bigg], \\ \forall\boldsymbol{x},\quad \forall\widehat{\boldsymbol{\Omega}}\in 4\pi,\quad \forall E\in[0,\infty),\quad \forall t\geq 0,\end{aligned} \tag{2.1}$$

where $\boldsymbol{x}$ is the location vector, $\widehat{\boldsymbol{\Omega}}$ is the direction vector, E is the neutron energy, t is the time, v is the neutron velocity, Σ quantities are the cross sections, ψ is the angular flux, ν is the average number of neutrons produced per fission, and χ is the fission spectrum.

The location vector, $\boldsymbol{x}$, is a column vector of the spatial coordinates:

$$\boldsymbol{x} \equiv \begin{bmatrix} x \\ y \\ z \end{bmatrix}. \tag{2.2}$$

The direction vector, $\widehat{\boldsymbol{\Omega}}$, is a column unit-vector which gives the direction of flight for neutrons, and

is defined by

$$\widehat{\boldsymbol{\Omega}} \equiv \begin{bmatrix} \Omega_x \\ \Omega_y \\ \Omega_z \end{bmatrix} = \begin{bmatrix} \sqrt{1-\mu^2}\cos(\varphi) \\ \sqrt{1-\mu^2}\sin(\varphi) \\ \mu \end{bmatrix}, \tag{2.3a}$$

where φ is the azimuthal angle, and μ is the cosine of the polar angle θ,

$$\mu \equiv \cos(\theta). \tag{2.3b}$$

This spatial and angular coordinates system is depicted visually in Fig. 2.1.

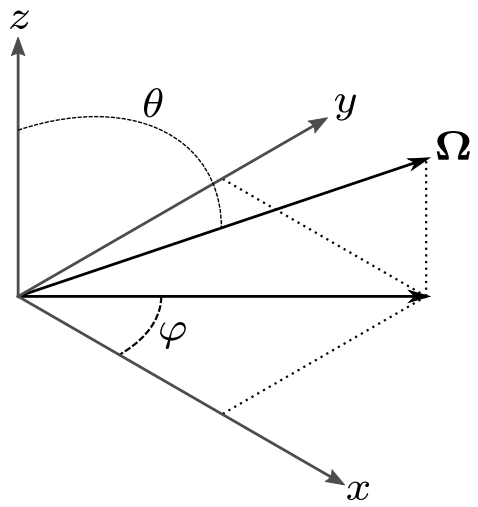

Figure 2.1: Depiction of the spatial and directional coordinate system used in the neutron transport equation.

The transport equation, given by Eq. (2.1), is an equation that represents the balance of neutrons. The first term represents the change of neutron density in time, where $\psi(\boldsymbol{x}, \widehat{\boldsymbol{\Omega}}, E)/v(E)$ is the neutron density. The streaming term, $\widehat{\boldsymbol{\Omega}} \cdot \boldsymbol{\nabla}\psi(\boldsymbol{x}, \widehat{\boldsymbol{\Omega}}, E)$, gives the rate at which neutrons are moving in or out of the of a point in phase-space due to flight through space. The collision term, $\Sigma_t(\boldsymbol{x}, E, t)\psi(\boldsymbol{x}, \widehat{\boldsymbol{\Omega}}, E)$, gives the rate at which neutrons have interactions (collisions) with a nucleus of the surrounding material. The source terms make up the right-hand side of the equation, and are separated into three components: an external source, the scattering source, and the fission source. The scattering source, $\int_0^\infty \int_{4\pi} \Sigma_s(\boldsymbol{x}, \widehat{\boldsymbol{\Omega}}' \cdot \widehat{\boldsymbol{\Omega}}, E' \to E, t)\psi(\boldsymbol{x}, \widehat{\boldsymbol{\Omega}}', E', t)\,\mathrm{d}\Omega'\,\mathrm{d}E'$, gives the rate at which neutrons are scattered into the given direction and energy at a set point in space. The fission source, $\chi(\boldsymbol{x}, E)\int_0^\infty \nu\Sigma_f(\boldsymbol{x}, E', t)\int_{4\pi}\psi(\boldsymbol{x}, \widehat{\boldsymbol{\Omega}}', E', t)\,\mathrm{d}\Omega'\,\mathrm{d}E'$, gives the production rate of neutrons due to *immediate* (prompt) fission events. The vast majority of fission events are prompt, though a small fraction of fission events emit *delayed* neutrons. Generally, in steady-state calculations the difference between prompt and delayed fission neutrons is ignored. However, for

transient calculations for accident events, capturing this difference is essential. The external source, $Q(\boldsymbol{x}, \widehat{\boldsymbol{\Omega}}, E, t)$, is a generic term that accounts for neutrons produced by all other processes that are not directly dependent on the angular flux.

Generally, reactor physicists are interested in reaction rates, which are useful for determining power production, rather than the angular flux. A reaction rate at a specific point, direction, and energy can be computed as the product of the reaction cross section and the angular flux. Integration over a volume, energy range, and direction gives a total reaction rate which can be used in reactor physics calculations. For convenience, it is useful to define derived quantities that are used in these calculations. The *scalar flux*

$$\phi(\boldsymbol{x}, E) \equiv \int_{4\pi} \psi(\boldsymbol{x}, \widehat{\boldsymbol{\Omega}}, E)\, \mathrm{d}\Omega, \tag{2.4}$$

is the zeroth order angular moment. The neutron *current* is a vector quantity, and is the first order angular moment of the angular flux

$$\boldsymbol{J}(\boldsymbol{x}, E) \equiv \int_{4\pi} \widehat{\boldsymbol{\Omega}} \psi(\boldsymbol{x}, \widehat{\boldsymbol{\Omega}}, E)\, \mathrm{d}\Omega. \tag{2.5}$$

Generally, the higher order angular moments of the angular flux are defined as

$$\Phi_\ell^n(\boldsymbol{x}, E) \equiv \int_{4\pi} R_\ell^n(\widehat{\boldsymbol{\Omega}}) \psi(\boldsymbol{x}, \widehat{\boldsymbol{\Omega}}, E)\, \mathrm{d}\Omega, \tag{2.6}$$

where $R_\ell^n(\widehat{\boldsymbol{\Omega}})$ are the real spherical harmonics functions defined by

$$R_\ell^n(\widehat{\boldsymbol{\Omega}}) \equiv \sqrt{(2 - \delta_{n,0}) \frac{(\ell - |n|)!}{(\ell + |n|)!}} P_\ell^{|n|}(\mu) \mathcal{T}(\varphi), \tag{2.7a}$$

where $P_\ell^{|n|}(\mu)$ is the Ferrer definition of the associated Legendre Polynomial defined as

$$P_\ell^{|n|}(\mu) \equiv \left(1 - \mu^2\right)^{n/2} \frac{\mathrm{d}^n}{\mathrm{d}\mu^n} P_\ell(\mu), \quad n \geq 0, \tag{2.7b}$$

and

$$\mathcal{T}(\varphi) \equiv \begin{cases} \cos(n\varphi), & \text{if } n \geq 0, \\ \sin(|n|\varphi), & \text{otherwise.} \end{cases} \tag{2.7c}$$

2.2 k-Eigenvalue Problems

One of the most common calculations done by reactor analysts is the simulation of reactor systems at operating conditions. A reactor operating at normal conditions is effectively unchanging in time,

i.e. the derivative in time of Eq. (2.1) is zero. The common technique for solving this class of problems is to transform Eq. (2.1) into an eigenvalue problem, such that the fission source is scaled to preserve neutron balance:

$$\begin{aligned}\left[\widehat{\boldsymbol{\Omega}}\cdot\boldsymbol{\nabla}+\Sigma_t(\boldsymbol{x},E)\right]\psi(\boldsymbol{x},\widehat{\boldsymbol{\Omega}},E)=\frac{1}{4\pi}\Bigg[&Q(\boldsymbol{x},\widehat{\boldsymbol{\Omega}},E)\\&+\int_0^\infty\int_{4\pi}\Sigma_s(\boldsymbol{x},\widehat{\boldsymbol{\Omega}}'\cdot\widehat{\boldsymbol{\Omega}},E'\to E)\psi(\boldsymbol{x},\widehat{\boldsymbol{\Omega}}',E')\,\mathrm{d}\Omega'\,\mathrm{d}E'\\&+\chi(\boldsymbol{x},E)\int_0^\infty\nu\Sigma_f(\boldsymbol{x},E')\phi(\boldsymbol{x},E')\,\mathrm{d}E'\Bigg],\end{aligned}\tag{2.8}$$

$$\forall\boldsymbol{x},\quad\forall\widehat{\boldsymbol{\Omega}}\in 4\pi,\quad\forall E\in[0,\infty),$$

where k_{eff} is the inverse of the largest eigenvalue of the system λ_1. The multiplication factor, k_{eff}, indicates the criticality of the system. If k_{eff} is 1, then the system is critical and will remain at the current conditions unless otherwise changed. A k_{eff} less than one indicates that the system is subcritical and indicates the reactor system is unable to sustain the chain reaction of nuclear fission reactions to produce power. Finally, a k_{eff} greater than one indicates that a system is supercritical and, if not changed, will increase in power.

Generally, this class of problems are solved iteratively, this will be discussed in more detail in Section 2.4. Given an initial guess for the neutron flux, and eigenvalue, a "fixed source" can be computed by integrating over angle and energy. Given the source, an updated neutron flux can be solved for, allowing for update of the eigenvalue and source terms. Because it is an eigenvalue problem, the angular flux requires a normalization. This process can be repeated until the eigenvalue and angular flux are sufficiently converged.

Still, Eq. (2.8) has a six-dimensional phase space and cannot, in general systems, be solved exactly. Approximations, and numerical techniques must be used to obtain approximate solutions to this equation in calculations for realistic reactor systems. In the Section 2.3, an overview of several methods for solving this equation, or approximate forms of this equation, is provided.

2.3 Computational Methods

Generally, transport methods are divided into two broad categories: stochastic and deterministic. Stochastic methods, also called "Monte Carlo" methods, rely on random sampling to emulate the "life" of individual neutrons. Deterministic methods rely on making further approximations to the transport equation. Overviews of these different approaches are given in the subsequent subsections.

2.3.1 Monte Carlo

Stochastic, or "Monte Carlo" methods are methods that simulate individual neutrons in the system. The simulation of each neutron relies on the random sampling of probability distributions for all aspects such as, where the *free* neutron is born, which direction it is traveling in, the energy of the neutron, the distance to the next collision, and the type of collision event. This process is repeated until the neutron leaks out of the system or is absorbed, possibly inducing a fission event with other neutrons to simulate, for many different neutrons.

Monte Carlo methods give a probabilistic estimate of the true solution as well as an associated uncertainty in that result. This class of methods is generally considered to be the most accurate because they are capable of representing the phase-space exactly. As more particles are simulated the uncertainty in the estimated solution is reduced.

For whole-core reactor analysis, the quantities of interest would typically require an extremely large number of individual neutron histories to be simulated. Variance reduction techniques are an area of active research that allow for quantities of interest to be estimated accurately with fewer histories. However, generally Monte Carlo methods remain too expensive for whole-core calculations.

2.3.2 Deterministic Methods

Deterministic methods rely on making approximations to the transport equation. Discretization approximations are among the most common approximations used in deterministic methods. In these methods, it is generally not possible to represent the phase-space as continuous; it is necessary to discretize space, angle, and energy.

2.3.2.1 The Multi-group Approximation

The multi-group approximation is an approximation that is common in nearly every deterministic neutron transport methods. This approximation discretizes the continuous energy spectrum into discrete energy groups. Generally, cross sections have strong dependence on the energy of incident neutrons; this dependence is typically not smooth due to the presence of resonances. Around resonance energies, the cross sections are increased significantly, as observed in Fig. 2.2.

The complicated dependence on energy would require hundreds of thousands of energy points to faithfully represent for the energies of interest in thermal reactors. Modeling of this many energy points in whole-core simulations would require too much memory. The multi-group approximation divides this energy space into several energy groups; within each group cross sections are averaged. The multi-group eigenvalue transport equation can be found by integrating the Eq. (2.8) over an

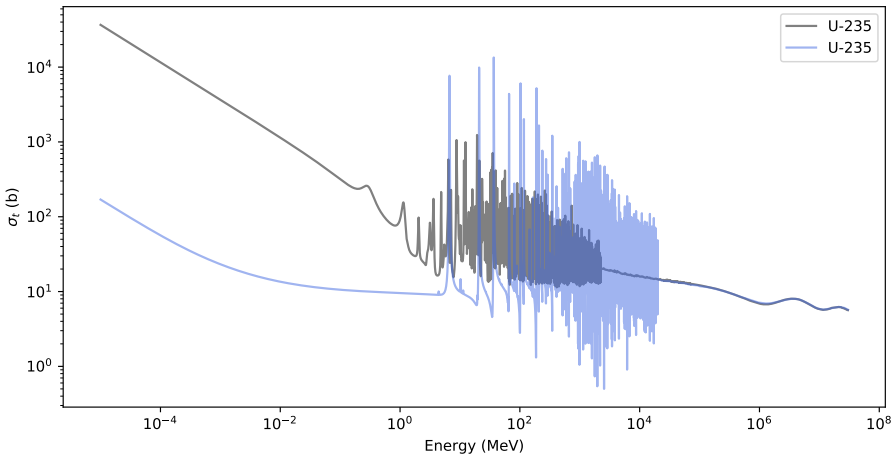

Figure 2.2: Uranium 235 and 238 total microscopic cross sections as a function of energy. Data provided through the ENDF-8.0 nuclear reaction data library [23].

energy energy interval $[E_g, E_{g-1})$.

$$\left[\widehat{\boldsymbol{\Omega}} \cdot \boldsymbol{\nabla} + \Sigma_t^g(\boldsymbol{x}, \widehat{\boldsymbol{\Omega}})\right] \psi^g(\boldsymbol{x}, \widehat{\boldsymbol{\Omega}}) = \frac{1}{4\pi}\left[\sum_{g'=1}^{G} \int_{4\pi} \Sigma_s^{g' \to g}(\boldsymbol{x}, \widehat{\boldsymbol{\Omega}}, \widehat{\boldsymbol{\Omega}}') \psi^{g'}(\boldsymbol{x}, \widehat{\boldsymbol{\Omega}}')\, \mathrm{d}\Omega' + \frac{\chi^g(\boldsymbol{x})}{k_{\text{eff}}} \sum_{g'=1}^{G} \nu \Sigma_f^{g'}(\boldsymbol{x}, \widehat{\boldsymbol{\Omega}}) \phi^{g'}(\boldsymbol{x})\right] \tag{2.9}$$

$$\forall \boldsymbol{x}, \quad \forall \widehat{\boldsymbol{\Omega}} \in 4\pi, \quad \forall g \in \{1, 2, \ldots, G\},$$

where the multi-group quantities are defined by

$$\psi^g(\boldsymbol{x}, \widehat{\boldsymbol{\Omega}}) \equiv \int_{E_g}^{E_{g-1}} \psi(\boldsymbol{x}, \widehat{\boldsymbol{\Omega}}, E)\, \mathrm{d}E, \tag{2.10a}$$

$$\chi^g(\boldsymbol{x}) \equiv \int_{E_g}^{E_{g-1}} \chi(\boldsymbol{x}, E)\, \mathrm{d}E, \tag{2.10b}$$

$$\Sigma_t^g(\boldsymbol{x}, \widehat{\boldsymbol{\Omega}}) \equiv \frac{\int_{E_g}^{E_{g-1}} \Sigma_t(\boldsymbol{x}, E) \psi(\boldsymbol{x}, \widehat{\boldsymbol{\Omega}}, E)\, \mathrm{d}E}{\psi^g(\boldsymbol{x}, \widehat{\boldsymbol{\Omega}})}, \tag{2.10c}$$

$$\nu\Sigma_f^g(\boldsymbol{x}, \widehat{\boldsymbol{\Omega}}) \equiv \frac{\int_{E_g}^{E_{g-1}} \nu\Sigma_f(\boldsymbol{x}, E) \psi(\boldsymbol{x}, \widehat{\boldsymbol{\Omega}}, E)\, \mathrm{d}E}{\psi^g(\boldsymbol{x}, \widehat{\boldsymbol{\Omega}})}, \tag{2.10d}$$

$$\Sigma_s^{g'\to g}(\boldsymbol{x},\widehat{\boldsymbol{\Omega}},\widehat{\boldsymbol{\Omega}}') \equiv \frac{\int_{E_g}^{E_{g-1}}\int_{E_{g'}}^{E_{g'-1}} \Sigma_s(\boldsymbol{x},\widehat{\boldsymbol{\Omega}}'\cdot\widehat{\boldsymbol{\Omega}},E'\to E)\psi(\boldsymbol{x},\widehat{\boldsymbol{\Omega}}',E')\,\mathrm{d}E'\,\mathrm{d}E}{\psi^{g'}(\boldsymbol{x},\widehat{\boldsymbol{\Omega}}')}. \tag{2.10e}$$

By defining the cross sections in this way, no approximations have been made, and the reaction rates of each energy group are preserved. However, this approach has two issues: the cross sections are dependent on the angular flux which is not known *a priori*, and have dependence on the neutron direction of flight. Generally, the dependence on the angular flux is addressed by solving a simplified problem to generate a continuous or fine-group neutron energy spectrum. This spectrum is then used to "collapse" the cross sections into coarser multi-group values [24]. This introduces approximation into the transport equation.

To eliminate the directional dependence of the multi-group cross sections, an additional approximation is made: isotropic angular flux spectrum,

$$\psi(\boldsymbol{x},\widehat{\boldsymbol{\Omega}},E) \approx \frac{1}{4\pi}\Phi(\boldsymbol{x},E). \tag{2.11}$$

Using this approximate angular flux as the weighting function for multi-group cross sections in Eqs. (2.9) and (2.10) can be simplified to

$$\begin{aligned}\left[\widehat{\boldsymbol{\Omega}}\cdot\boldsymbol{\nabla}+\Sigma_t^g(\boldsymbol{x})\right]\psi^g(\boldsymbol{x},\widehat{\boldsymbol{\Omega}}) = \frac{1}{4\pi}\Bigg[&\sum_{g'=1}^{G}\int_{4\pi}\Sigma_s^{g'\to g}(\boldsymbol{x},\widehat{\boldsymbol{\Omega}}'\cdot\widehat{\boldsymbol{\Omega}})\psi^{g'}(\boldsymbol{x},\widehat{\boldsymbol{\Omega}}')\,\mathrm{d}\Omega' \\ &+\frac{\chi^g(\boldsymbol{x})}{k_{\text{eff}}}\sum_{g'=1}^{G}\nu\Sigma_f^{g'}(\boldsymbol{x})\int_{4\pi}\psi^{g'}(\boldsymbol{x},\widehat{\boldsymbol{\Omega}}')\,\mathrm{d}\Omega'\Bigg], \\ \forall\boldsymbol{x},\quad \forall\widehat{\boldsymbol{\Omega}}\in 4\pi,\quad &\forall g\in\{1,2,\ldots,G\},\end{aligned} \tag{2.12}$$

where the approximated multigroup cross sections are defined as

$$\Sigma_t^g(\boldsymbol{x}) \equiv \frac{\int_{E_g}^{E_{g-1}}\Sigma_t(\boldsymbol{x},E)\Phi(\boldsymbol{x},E)\,\mathrm{d}E}{\int_{E_g}^{E_{g-1}}\Phi(\boldsymbol{x},E)\,\mathrm{d}E}, \tag{2.13a}$$

$$\nu\Sigma_f^g(\boldsymbol{x}) \equiv \frac{\int_{E_g}^{E_{g-1}}\nu\Sigma_f(\boldsymbol{x},E)\Phi(\boldsymbol{x},E)\,\mathrm{d}E}{\int_{E_g}^{E_{g-1}}\Phi(\boldsymbol{x},E)\,\mathrm{d}E}, \tag{2.13b}$$

$$\Sigma_s^{g'\to g}(\boldsymbol{x},\widehat{\boldsymbol{\Omega}}'\cdot\widehat{\boldsymbol{\Omega}}) \equiv \frac{\int_{E_g}^{E_{g-1}}\int_{E_{g'}}^{E_{g'-1}}\Sigma_s(\boldsymbol{x},\widehat{\boldsymbol{\Omega}}'\cdot\widehat{\boldsymbol{\Omega}},E'\to E)\Phi(\boldsymbol{x},E')\,\mathrm{d}E'\,\mathrm{d}E}{\int_{E_{g'}}^{E_{g'-1}}\Phi(\boldsymbol{x},E')\,\mathrm{d}E'}. \tag{2.13c}$$

2.3.2.2 Spatial Discretization

Nearly all computational transport methods involve some form of spatial discretization. Reactor designs include many different material regions, and nearly all simulation tools will discretize the spatial domain into these different material regions. Deterministic methods will generally apply a finer meshing within these material regions, into transport cells. For the purposes of this work, a cell $\mathcal{R}_i$ is indexed with i. A visualization of the material and hypothetical meshing for a single pin-cell are shown in Fig. 2.3. In deterministic codes, the typical assumption is that material properties (cross sections) are constant within each computational cell.

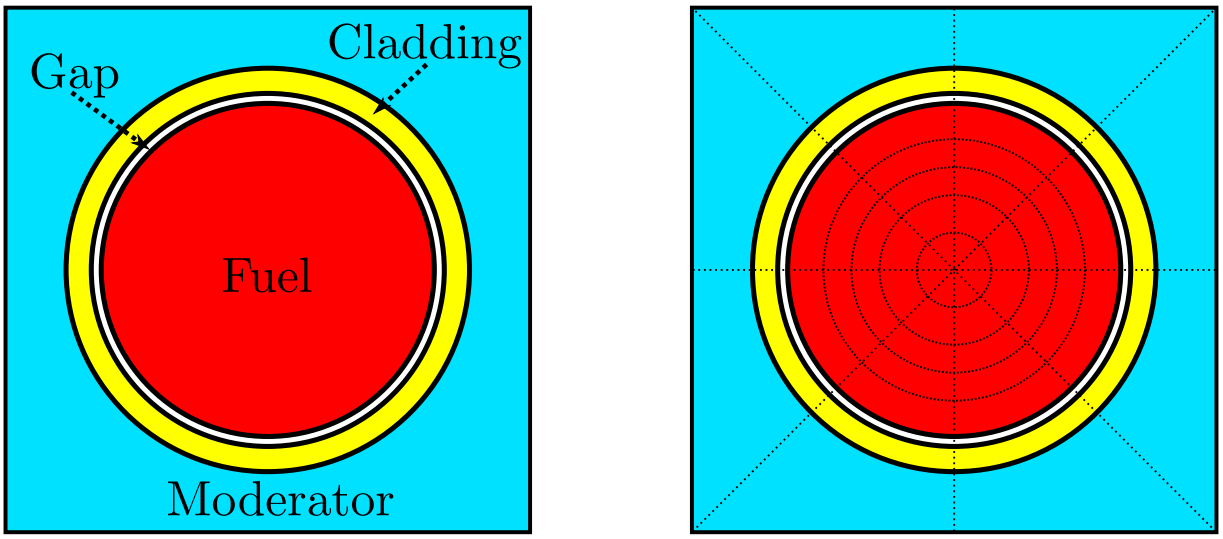

(a) Material regions

(b) Hypothetical computational cell mesh

Figure 2.3: Material and mesh spatial discretization examples for a single pin cell.

2.3.2.3 Directional Discretization

Typically, the directional variable cannot be treated exactly in deterministic methods. There are two common methods of approximating behavior as a function of direction $\widehat{\mathbf{\Omega}}$:

1. Spherical Harmonics (P_N) Expansion
2. Discrete Ordinates (S_N)

Expansion in spherical harmonics, often referred to as P_N, is one of the oldest transport methods, where N indicates the order of the expansion. In this method, the angular flux is expanded as a linear combination of spherical harmonics moments. The simplest expansion of order 1, reduces to the diffusion approximation.

The Discrete Ordinates (S_N) method is a discretization of the directional variable $\widehat{\mathbf{\Omega}}$; typically, the discrete direction values are determined using a set of quadrature points. Let the $\mathcal{M}_N$ be the set of discrete directions, and weights,

$$\mathcal{M}_N \equiv \left\{ \widehat{\mathbf{\Omega}}_m \in \{\widehat{\mathbf{\Omega}}_1, \widehat{\mathbf{\Omega}}_2, \ldots, \widehat{\mathbf{\Omega}}_N\}, w_m \in \{w_1, w_2, \ldots, w_N\} \right\}, \tag{2.14a}$$

such that a directional integration can be approximated as

$$\int_{4\pi} f(\widehat{\mathbf{\Omega}}) \, \mathrm{d}\Omega \approx 4\pi \sum_{m \in \mathcal{M}_N} w_m f(\widehat{\mathbf{\Omega}}_m), \tag{2.14b}$$

where

$$\sum_{m \in \mathcal{M}_N} w_m = 1. \tag{2.14c}$$

There are two common forms of quadrature sets that are commonly used in transport calculations: level-symmetric and product quadratures. The level-symmetric quadratures include directions that are evenly distributed over the unit-sphere; this is optimal in situations where each direction has similar variation. However, typical reactor designs have significantly less variation in the axial (z) direction which fuel rods are oriented along. In this situation, neutrons with directions close to the z-axis are modeled poorly because there are few azimuthal angles at these polar levels, as is demonstrated in Fig. 2.4a. These steep polar angles are important in reactor analysis due to self-shielding effects, which are strongly dependent on polar angle.

Product quadratures are generated by a multiplicative combination of separate quadrature sets in the azimuthal and polar directions. The azimuthal quadrature set in generated over the domain $[0, 2\pi]$, while the polar quadrature set is generated for the polar cosine μ over the domain $[-1, 1]$. This quadrature generation technique does not suffer from the same issue for steep polar directions, as each polar level has the same number of azimuthal directions. A common choice for the azimuthal quadrature generation in the Chebyshev quadrature set, which gives evenly spaced azimuthal angles. The polar cosine quadrature set typically uses a Gauss-Legendre quadrature set, or an optimized quadrature set such as the Tabuchi-Yamamoto quadrature [25]. Figure 2.4b shows an example of a product quadrature's set of directions using a Chebyshev azimuthal quadrature and Gauss-Legendre polar quadrature.

2.3.2.4 The Method of Characteristics

The Method of Characteristics (MoC) is a technique used in mathematics to solve Partial Differential Equations (PDEs), by transforming a PDE into a system of Ordinary Differential Equations (ODEs). The method was first applied to the neutron transport problem by Askew in 1972 [10], but only

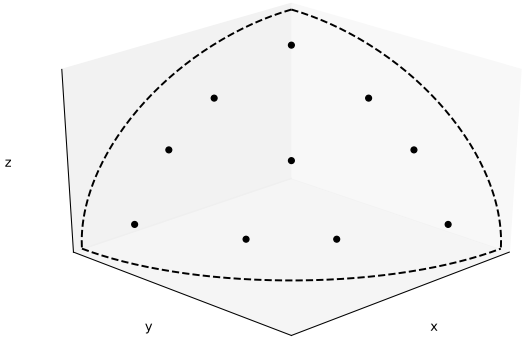

(a) Level-Symmetric Quadrature (S_8)

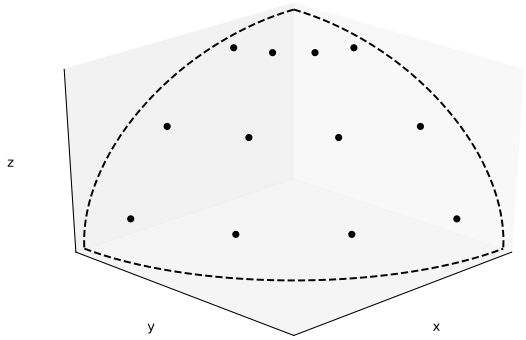

(b) Chebyshev-Gauss Product Quadrature with 4 azimuthal and 3 polar angles

Figure 2.4: (a) Level-Symmetric and (b) product quadrature direction set examples shown for a single octant of the unit-sphere.

began to see real use in the 1980's [26]. The MoC transforms the transport equation into the characteristic form, by examining the equation along straight neutron paths through the spatial domain.

Typically, the spatial domain is discretized into cells that have uniform material data (cross sections). By examining the equation along one of these characteristic "tracks" or "rays", the average angular flux along the track within a cell can be calculated. The scalar flux can then be found by collecting the average angular flux along all tracks passing through this region, in a numerical integration over space and angle.

Like the Collision Probability (CP) method, MoC is able to handle completely arbitrary geometry; however, it is also able to account for anisotropic scattering. Additionally, the MoC does not produce the large matrices in realistic applications as the CP method does. For problems that contain more than a few hundred cells, the MoC is generally preferred over CP methods [27].

The method of Characteristic Direction Probabilities (CDP) is a method similar to both CP method and the MoC [28, 29]; the major difference from CP is that CDP only couples together cells are traversed by characteristic tracks. This significantly cuts down on the computational resources required by traditional CP methods. This method has also shown improvements over MoC in cases with few unique geometries and constant material properties throughout the simulation; however these conditions are not applicable in problems of interest to industry.

The MoC is the primary subject of this thesis work. As such, Chapter 3 has been devoted to the details of the method, and Chapter 4 expands upon the details of ray-tracing that is central to the MoC.

2.4 Source Iteration

Generally, the k-eigenvalue transport problems, introduced in Section 2.2, are solved iteratively. Given an initial guess for the k-eigenvalue, boundary conditions, and interior flux-moments, an estimate of the source can be computed. A transport "sweep" can be performed, in which updated boundary conditions and flux-moments are computed. Given these updated flux-moments a new estimate of the eigenvalue can be calculated. This process can be repeated until the eigenvalue and flux-moments are converged within some tolerance. For simplicity, this process is shown for a isotropic mono-energetic, continuous-space, one-dimensional transport problem in Algorithm 1.

Algorithm 1 Source Iteration algorithm for the k-eigenvalue transport problem.

1: Begin iteration j with a known boundary conditions, scalar flux estimate, $\phi^{(j)}(x)$, and a k-eigenvalue estimate, k_{eff}^{j}.
2: Perform a transport sweep:

$$\left[\mu\frac{\partial}{\partial x} + \Sigma_t(x)\right]\psi^{(j+1)}(x,\mu) = \frac{1}{2}\left[\Sigma_s(x) + \frac{1}{k_{\text{eff}}^{(j)}}\nu\Sigma_f(x)\right]\phi^{(j)}(x), \tag{2.15}$$

$$\forall x \in [0, X], \quad \forall \mu \in [-1, 1].$$

3: Update the scalar flux, and the eigenvalue for the next iteration:

$$\phi^{(j+1)}(x) = \int_{-1}^{1}\psi^{(j+1)}(x,\mu)\,\mathrm{d}\mu\frac{\Phi_0}{\frac{1}{X}\int_0^X\int_{-1}^{1}\psi^{(j+1)}(x',\mu)\,\mathrm{d}\mu\,\mathrm{d}x'}, \tag{2.16a}$$

$$k_{\text{eff}}^{(j+1)} = \frac{\int_0^X \nu\Sigma_f\phi^{(j+1)}(x)\,\mathrm{d}x}{\int_0^X \Sigma_a\phi^{(j+1)}(x)\,\mathrm{d}x}. \tag{2.16b}$$

4: Repeat steps 1. - 3. until sufficient convergence.

2.4.1 Transport Acceleration

While Algorithm 1 is valid, it typically converges very slowly, requiring many iterations to get reasonable results. In full-core calculations, a single transport sweep can become computationally expensive and using Algorithm 1 is not feasible. There has been considerable effort in developing methods that accelerate transport calculations by using a lower-order calculation, typically based on the diffusion approximation. While other acceleration methods exist [30], the most common are non-linear diffusion acceleration (NDA) methods [31], typically using the coarse mesh finite-difference (CMFD) method [32].

The CMFD acceleration method has been shown to significantly reduce computational transport

run-times [8, 31, 33]. Improvements upon the original CMFD formulation [32]. The pCMFD method preserves partial currents rather than net currents, and has been shown to be unconditionally stable for transport problems at fixed conditions [34]. The odCMFD method generalizes the CMFD and pCMFD methods by adding an artificial term to the diffusion coefficient, and has faster convergence properties than pCMFD [35].

Utilization of CMFD acceleration in transport calculations with thermal-hydraulic (T/H) feedback has not had the favorable stability and convergence properties as calculations without feedback [36]. Many transport codes have required under-relaxation of the scalar flux in the iteration schemes for stability in these calculations; there is ongoing research investigating a less ad-hoc approach [36]. This instability and convergence slow-down in problems with feedback has prevented full utilization of more advanced multi-level solvers [37].

CHAPTER 3

The Method of Characteristics

3.1 Fundamentals

The Method of Characteristics (MoC) is a technique used in mathematics to solve PDEs, by transforming a PDE into a system of ODEs. The method was first applied to the neutron transport problem by Askew in 1972 [10], but only began to see real use in the 1980's [26]. The MoC transforms the transport equation into the characteristic form, by examining the equation along straight neutron paths through the spatial domain. For simplicity, the derivation of this method will begin with the multi-group S_N k-eigenvalue transport equation with spatially discretized mesh with constant material properties within each cell.

$$\left[\widehat{\boldsymbol{\Omega}}_m \cdot \boldsymbol{\nabla} + \Sigma_{t,i}^g\right] \psi_{mi}^g(\boldsymbol{x}) = \frac{1}{4\pi} q_{mi}^g(\boldsymbol{x}) \,, \tag{3.1}$$

$$\forall \boldsymbol{x} \in \mathcal{R}_i, \quad \forall m \in \mathcal{M}_N, \quad \forall i, g,$$

where $\mathcal{R}_i$ is the spatial cell, $\mathcal{M}_N$ is the directional quadrature, as described in Section 2.3.2.3, and the fixed-source, $q_{mi}^g(\boldsymbol{x})$ can be found by applying the discrete-to-moment operator, $\mathcal{S}_{i,m}^g$, defined by

$$\mathcal{S}_{i,m}^g(f) \equiv \sum_{g'} \sum_{\ell=0}^{L} \sum_{n=-\ell}^{\ell} R_\ell^n(\widehat{\boldsymbol{\Omega}}_m) \Sigma_{s,\ell,i}^{g' \to g} f_{n,i}^{\ell,g'}(\boldsymbol{x}) + \frac{\chi_i^g}{k_{\text{eff}}} \sum_{g'} \nu \Sigma_{f,i}^{g'} f_i^{g'}(\boldsymbol{x}), \tag{3.2}$$

to get

$$q_{mi}^g(\boldsymbol{x}) \equiv \left[\sum_{g'} \sum_{\ell=0}^{L} \sum_{n=-\ell}^{\ell} R_\ell^n(\widehat{\boldsymbol{\Omega}}) \Sigma_{s,\ell,i}^{g' \to g} \Phi_{i,n}^{\ell,g}(\boldsymbol{x}) + \frac{\chi_i^g}{k_{\text{eff}}} \sum_{g'} \nu \Sigma_{f,i}^{g'} \phi_i^{g'}(\boldsymbol{x}) \right]. \tag{3.3}$$

Consider a point, $\boldsymbol{x}_0$, and a line passing through this point in direction $\widehat{\boldsymbol{\Omega}}_m$. Any location along this *characteristic* line (also referred to as a ray, or track), can be described as

$$\boldsymbol{x} = \boldsymbol{x}_0 + s\widehat{\boldsymbol{\Omega}}_m, \tag{3.4}$$

where s is the distance along the track from $\boldsymbol{x}_0$. Applying this transformation, Eq. (3.1) is put into the characteristic form

$$\left[\frac{\mathrm{d}}{\mathrm{d}s} + \Sigma_{t,i}^g\right] \psi_{mi}^g\Big(\boldsymbol{x}_0 + s\widehat{\boldsymbol{\Omega}}_m\Big) = \frac{1}{4\pi} q_{mi}^g\Big(\boldsymbol{x}_0 + s\widehat{\boldsymbol{\Omega}}_m\Big)\,. \tag{3.5}$$

As described in Section 2.1, reactor physicists are generally interested in integrated angular flux quantities rather than the angular flux. It is thus typical in the MoC to have many different characteristic tracks through our problem; in this work separate tracks will be subscripted with the index k. The characteristic form of the transport equation then becomes

$$\left[\frac{\mathrm{d}}{\mathrm{d}s} + \Sigma_{t,i}^g\right] \psi_{mki}^g(s) = \frac{1}{4\pi} q_{mi}^g(s)\,, \tag{3.6}$$

$$\forall s \in [0, s_{mki}], \forall m \in \mathcal{M}_N, \forall i, k, g,$$

where s_{mki} is the total length of the track-segment, as depicted in Fig. 3.1.

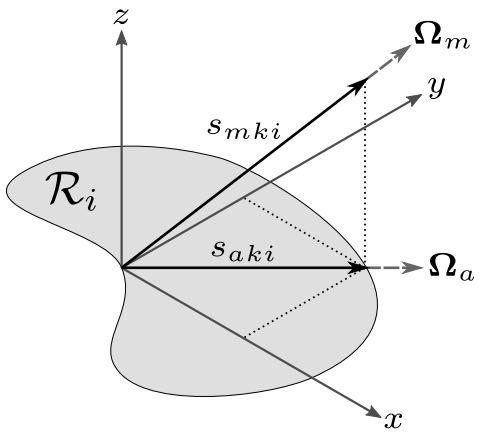

Figure 3.1: Depiction of a single characteristic track through a cell i.

Equation (3.6) can be solved analytically along a characteristic track-segment using an integrating factor,

$$M(s) = \exp\left(\int_0^s \Sigma_{t,i}^g \,\mathrm{d}s'\right) = \exp(\tau_m^g)\,, \tag{3.7}$$

where the *optical thickness*, τ_m^g, is defined by

$$\tau_m^g \equiv \Sigma_{t,i}^g s. \tag{3.8}$$

Using this integrating factor, the generic solution to the MoC equation, given in Eq. (3.6), is

$$\psi^g_{mki}(s) = \psi^{g,\text{in}}_{mki} \exp(-\tau^g_m) + \int_0^s \frac{1}{4\pi} q^g_{mi}(s') \exp\left(-\Sigma^g_{t,i}\left[s - s'\right]\right) \mathrm{d}s', \tag{3.9}$$

where $\psi^{g,\text{in}}_{mki}$ is the incident angular flux, $\psi^g_{mki}(0)$. If a source shape is provided, Eq. (3.9) can be evaluated for every track-segment in the problem. The next subsection introduces formal methods to approximate the integration of quantities over both space and direction. These procedures can be used to determine the scalar flux or other quantities necessary in MoC calculations.

3.1.1 Track-Based Integration

Determining the angular flux along a single characteristic track is typically not very useful for reactor physics calculations. It is most often necessary to evaluate reaction rates, and therefore the scalar flux through integration of the angular flux. This section aims to provide a formal basis for the integration process used in the MoC calculations in this work.

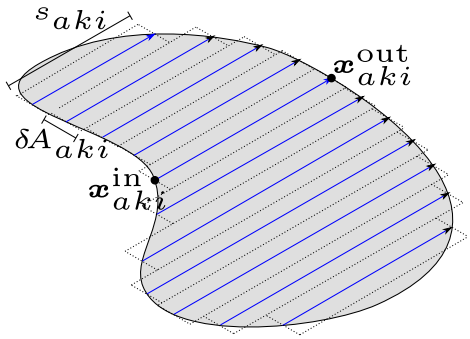

Figure 3.2: Example characteristic tracks (2D) through a cell for a single direction.

The MoC is based on the Discrete Ordinates (S_N) approximation; integration over the directional variable simply becomes a quadrature integration:

$$\int_{4\pi} f(\widehat{\boldsymbol{\Omega}})\, \mathrm{d}\Omega \approx 4\pi \sum_m w_m f(\widehat{\boldsymbol{\Omega}}_m). \tag{3.10}$$

Within a cell, $\mathcal{R}_i$, there are many characteristic track-segments in each direction in the directional quadrature, as is shown for a single direction in Fig. 3.2. Thus, the spatial discretization is different for each direction, and spatial integration is linked with directional integration. For a single direction, the integration over the spatial domain can be approximated by the weighted summation of track-averaged values, with the weight being equal to the area of the track-segment. The average value of

a function, $f(\boldsymbol{x}, \widehat{\boldsymbol{\Omega}}_m)$, along a track-segment is given as

$$\Big\langle f(\boldsymbol{x}, \widehat{\boldsymbol{\Omega}}_m) \Big\rangle_{mki} \equiv \frac{1}{s_{mki}} \int_0^{s_{mki}} f(s, \widehat{\boldsymbol{\Omega}}_m)\, \mathrm{d}s, \tag{3.11}$$

where s_{mki} is the total length of the track-segment. The spatial integration for a single direction becomes

$$\frac{1}{V_i} \int_{\boldsymbol{x} \in \mathcal{R}_i} f(\boldsymbol{x}, \widehat{\boldsymbol{\Omega}}_m)\, \mathrm{d}^3\boldsymbol{x} \approx \Big\langle f(\boldsymbol{x}, \widehat{\boldsymbol{\Omega}}_m) \Big\rangle_{mi} \equiv \frac{1}{V_i} \sum_k \delta A_{mki} s_{mki} \Big\langle f(\boldsymbol{x}, \widehat{\boldsymbol{\Omega}}_m) \Big\rangle_{mki}, \tag{3.12}$$

where δA_{mki} is the cross-sectional area of the track (width in 2D). In this notation, the integral is divided by the volume such that $\langle f \rangle_{mi}$ is approximately the mean value in the region, for the direction $\widehat{\boldsymbol{\Omega}}_m$. Finally, an integration over both space and angle can be defined as

$$\Big\langle f(\boldsymbol{x}, \widehat{\boldsymbol{\Omega}}) \Big\rangle_i = 4\pi \sum_m w_m \Big\langle f(\boldsymbol{x}, \widehat{\boldsymbol{\Omega}}_m) \Big\rangle_{mi}. \tag{3.13}$$

These integrations have been expressed as 3-D MoC equations. For 2-D calculations, the form remains the same, except that in Eq. (3.12), which requires a scaling factor on the cell volume (now area):

$$\frac{1}{V_i} \int_{\boldsymbol{x} \in \mathcal{R}_i} f(\boldsymbol{x}, \widehat{\boldsymbol{\Omega}}_m)\, \mathrm{d}^3\boldsymbol{x} \approx \Big\langle f(\boldsymbol{x}, \widehat{\boldsymbol{\Omega}}_m) \Big\rangle_{mi} \equiv \frac{\sin(\theta_p)}{V_i} \sum_k \delta A_{mki} s_{mki} \Big\langle f(\boldsymbol{x}, \widehat{\boldsymbol{\Omega}}_m) \Big\rangle_{mki} \tag{3.14}$$

3.1.2 Track-Length Renormalization

In general, the spatial integration described in Section 3.1.1 does not preserve the cell volume; this is visually apparent in Fig. 3.2. In order to preserve spatial volumes within a cell, track-lengths are often "renormalized". There are three renormalization methods which become obvious through the notation presented in Section 3.1.1:

1. segment-volume preservation
2. angle-volume preservation
3. volume preservation

Track-length renormalization involves adjusting the lengths of track-segments such that volume is preserved. Let us define a renormalization factor, ξ_{mki}, such that the renormalized track-length is

given by

$$t_{mki} = \xi_{mki} s_{mki}. \tag{3.15}$$

The spatial integration schemes given by Eqs. (3.11) and (3.12) become

$$\left\langle f(\boldsymbol{x}, \widehat{\boldsymbol{\Omega}}_m) \right\rangle_{mki} \equiv \frac{1}{t_{mki}} \int_0^{t_{mki}} f(s, \widehat{\boldsymbol{\Omega}}_m) \, \mathrm{d}t_m, \tag{3.16a}$$

and

$$\left\langle f(\boldsymbol{x}, \widehat{\boldsymbol{\Omega}}_m) \right\rangle_{mi} \equiv \frac{1}{V_i} \sum_k \delta A_{mki} t_{mki} \left\langle f(\boldsymbol{x}, \widehat{\boldsymbol{\Omega}}_m) \right\rangle_{mki}, \tag{3.16b}$$

where the spatial variable $\boldsymbol{x}$ can now be written as a function of the renormalized track-distance, t_m, as

$$\boldsymbol{x} = \boldsymbol{x}^{\text{in}}_{mki} + t_m \widehat{\boldsymbol{\Omega}}_m / \xi_{mki}, \tag{3.16c}$$

where $\boldsymbol{x}^{\text{in}}_{mki}$ is the starting point of the track-segment.

Segment-volume preservation is a renormalization method in which the track-length is adjusted such that the analytic volume within the cross-sectional area of each track-segment is preserved. This renormalization technique is the most "correct" method of renormalization, but is very expensive as each track is renormalized separately. It is also more difficult to implement, as the analytic area of each track-segment must be found. To the best of our knowledge, this method is not implemented in any production-level MoC code.

Angle-volume preservation is the next "best" renormalization technique. In this method, every mono-directional spatial integration should preserve the cell volume, i.e.

$$\langle 1 \rangle_{mi} = 1. \tag{3.17}$$

This constraint leads to the renormalization factor given by

$$\xi_{mi} = \frac{V_i}{\sum_k \delta A_{mki} s_{mki}}. \tag{3.18}$$

This method is significantly less expensive in terms of memory, computational time, and difficulty of implementation.

The simplest renormalization technique, volume preservation, only preserves the volume over the spatial and directional integration, i.e.

$$\langle 1 \rangle_i = 4\pi. \tag{3.19}$$

This constraint leads to the renormalization factor given by

$$\xi_i = \frac{V_i}{\sum_m w_m \sum_k \delta A_{mki} s_{mki}}. \tag{3.20}$$

Renormalization is not the only technique used for volume preservation. Another method is to use the numerical volume, $\sum_k \delta A_{mki} s_{mki}$ in place of V_i in Eq. (3.12). This seems to be a more consistent method; however, a detailed comparison of these methods has not taken place, to the best of my knowledge. The renormalization technique generally seems to be the faster approach, and is the approach used in MPACT [8], which is used extensively in this work.

3.2 The Flat-Source Approximation

The simplest approximation to the spatial shape of the source, $q^g_{mi}(\boldsymbol{x})$, within each cell is the flat-source approximation (FSA). The MoC has been widely used in lattice physics and neutron transport codes [24], many of which have utilized the flat-source method of characteristics (FSMoC) [7, 8, 26, 31, 38–41].

3.2.1 Derivation

The Flat Source (FS) approximation is simply the assumption that within each cell, $\mathcal{R}_i$, the source, $q^g_{mi}(\boldsymbol{x})$, is uniform. This can be expressed as

$$q^g_{mi}(\boldsymbol{x}) \approx q^g_{mi} = q^g_i + \sum_{\ell=0}^{L} \sum_{n=-\ell}^{\ell} R^n_\ell(\widehat{\boldsymbol{\Omega}}_m) q^{g,n}_{i,\ell} \tag{3.21}$$

Thus, to get a source in this form, Eq. (3.3) requires, that the region averaged scalar flux and higher-order angular moments (up to order L) be determined. In mathematical terms, the flat-source can be determined as

$$q^g_{mi} = \left[\sum_{g'} \sum_{\ell=0}^{L} \sum_{n=-\ell}^{\ell} R^n_\ell(\widehat{\boldsymbol{\Omega}}_m) \Sigma^{g'\to g}_{s,\ell,i} \Phi^{\ell,g'}_{i,n} + \frac{\chi^g_i}{k_{\text{eff}}} \sum_{g'} \nu \Sigma^{g'}_{f,i} \phi^{g'}_i \right], \tag{3.22}$$

where the $\phi^{g'}_i$ is the region-averaged scalar flux, and $\Phi^{\ell,g'}_{i,n}$ are the region-averaged higher-order angular moments of the flux.

In order to get these region-averaged flux moments, the spatial and directional integration

operators, introduced in Section 3.1.1, are used. The region-averaged scalar flux is then given by

$$\phi_i^g = \langle \psi^g \rangle_i = \frac{4\pi}{V_i} \sum_m w_m \sum_k t_{mki} \delta A_{mki} \langle \psi^g \rangle_{mki}, \tag{3.23a}$$

and the higher-order angular moments of the flux are given by

$$\Phi_{i,n}^{\ell,g} = \left\langle R_\ell^n(\widehat{\mathbf{\Omega}}) \psi^g \right\rangle_i = \frac{4\pi}{V_i} \sum_m w_m R_\ell^n(\widehat{\mathbf{\Omega}}_m) \sum_k t_{mki} \delta A_{mki} \langle \psi^g \rangle_{mki}. \tag{3.23b}$$

To evaluate these flux moments, the track-averaged angular flux, $\langle \psi^g \rangle_{mki}$, must be found. By applying the FSA, Eq. (3.6) becomes

$$\left[\frac{\mathrm{d}}{\mathrm{d}t_m} + \Sigma_{t,i}^g \right] \psi_{mki}^g(t_m) = \overline{q}_{mi}^g, \tag{3.24}$$

where

$$\overline{q}_{mi}^g \equiv \frac{1}{4\pi} q_{mi}^g. \tag{3.25}$$

This can be solved analytically for the angular flux along the track,

$$\psi_{mki}^g(t_m) = \psi_{mki}^{g,\text{in}} + \left(\frac{\overline{q}_{mi}^g}{\Sigma_{t,i}^g} - \psi_{mki}^{g,\text{in}} \right) F_1(\tau_m^g), \tag{3.26a}$$

where

$$F_1(\tau_m^g) \equiv 1 - \exp(-\tau_m^g), \tag{3.26b}$$

and τ_m^g is the (renormalized) optical thickness,

$$\tau_m^g \equiv t_m \Sigma_{t,i}^g. \tag{3.26c}$$

One approach to find $\langle \psi^g \rangle_{mki}$, is to plug Eq. (3.26a) to explicitly evaluate the track-average value, resulting in

$$\langle \psi^g \rangle_{mki} = \frac{\overline{q}_{mi}^g}{\Sigma_{t,i}^g} - \left(\frac{\overline{q}_{mi}^g}{\Sigma_{t,i}^g} - \psi_{mki}^{g,\text{in}} \right) \frac{F_1(\tau_{mki}^g)}{\tau_{mki}^g}. \tag{3.27}$$

Another, approach, which in the author's opinion is simpler, is use the track-averaging operator on the characteristic form of the equation, Eq. (3.24), which then simplifies to

$$\langle \psi^g \rangle_{mki} = \frac{\overline{q}_{mi}^g}{\Sigma_{t,i}^g} + \frac{\psi_{mki}^{g,\text{in}} - \psi_{mki}^{g,\text{out}}}{\tau_{mki}^g}. \tag{3.28}$$

Note, that these two forms are equivalent; by evaluating the outgoing flux in Eq. (3.26a) at the outgoing position, Eq. (3.28) can be put into the form of Eq. (3.27). The track-averaged angular flux can be used in Eq. (3.23) to evaluate the flux moments, which can then be used to compute the source. A transport calculation can then be carried out using the source iteration algorithm defined by Algorithm 1.

3.2.2 Particle Conservation

The neutron transport equation, Eq. (2.1), is a statement of particle balance within the defined phase-space. Previous works [15, 42] have examined the FSMoC with respect to *particle conservation*. Le Tellier and Hébert [42] defined necessary constraints on the directional quadrature and the characteristic tracks (trajectories) in order to ensure particle conservation for the anisotropic FSMoC. The constraints can be found by requiring

$$\frac{1}{4\pi}\left\langle R_\ell^n(\widehat{\mathbf{\Omega}})q_{mi}^g\right\rangle_i = q_{i,\ell}^{g,n}. \tag{3.29}$$

Substituting Eq. (3.21) into Eq. (3.29), requires that

$$\sum_m w_m R_\ell^n(\widehat{\mathbf{\Omega}}_m)R_{\ell'}^{n'}(\widehat{\mathbf{\Omega}}_m) = \delta_{\ell\ell'}\delta_{nn'}, \tag{3.30a}$$

and

$$\sum_k t_{mki}\delta A_{mki} = V_i. \tag{3.30b}$$

Equation (3.30a) is a constraint on the directional quadrature, requiring orthogonality of the real spherical harmonics [42]. Equation (3.30b) requires that direction-dependent renormalization, Eq. (3.18), is used.

If the constraints on directional quadrature, and characteristic tracks, are satisfied several simplifications to Eq. (3.23) can be made.

$$\phi_i^g = \frac{q_i^g}{\Sigma_{t,i}^g} + \frac{4\pi}{V_i\Sigma_{t,i}^g}\sum_m w_m \sum_k \delta A_{mki}\Delta\psi_{mki}^g, \tag{3.31a}$$

$$\Phi_{i,n}^{\ell,g} = \frac{q_{i,\ell}^{g,n}}{\Sigma_{t,i}^g} + \frac{4\pi}{V_i\Sigma_{t,i}^g}\sum_m w_m R_\ell^n(\widehat{\mathbf{\Omega}}_m)\sum_k \delta A_{mki}\Delta\psi_{mki}^g, \tag{3.31b}$$

where

$$\Delta\psi_{mki}^g \equiv \psi_{mki}^{g,\text{in}} - \psi_{mki}^{g,\text{out}}. \tag{3.31c}$$

3.2.3 Isotropic Simplifications

While anisotropic scattering is necessary for accurate calculations, it is also common for isotropic source calculations to be performed. Typically, these account for anisotropic behavior by using the transport-corrected P_0 (TCP0) approximation [43]. While not as accurate as truly anisotropic calculations, use of an isotropic source results in significantly fewer calculations, and allows for additional simplifications to be made.

Equation (3.29) is now only of concern for the isotropic component of the source. This results in the following constraint,

$$\sum_m w_m \sum_k t_{mki} \delta A_{mki} = V_i, \tag{3.32}$$

which is equivalent to the direction-independent renormalization, given by Eq. (3.20).

3.2.4 Applications

The FSMoC has been utilized in many MoC production codes [7, 8, 26, 31, 38–41]. However, previous studies on the FSMoC have found that a fine mesh must be used to obtain accurate results, particularly in the presence of control rods or blades, strong absorber rods, gadolinia poisoned fuel rods [44], as well as in the presence of large reflector regions (such as in critical experiments) [14]. As the number of mesh elements increase, so does the number of track-segments (on which the MoC computations are performed), which may result in large run-times. This has motivated the development of LSAs to the MoC, which are discussed in detail in Section 3.3.

3.3 The Linear-Source Approximation

3.3.1 Overview

The linear-source approximation (LSA), in the MoC, assumes the shape of the source along a characteristic track-segment is linear. There has long been motivation for the development of LSAs for the MoC, as previous work [45] indicated that a spatially linear source was able to achieve faster computational performance in S_N calculations. There have been many different variants of this approximation. The first instance of the LSA was the *gradient source approximation* introduced by Halsall [46]. This early linear-source method of characteristics (LSMoC) was based on the averaging of the angular flux gradient along tracks, and was implemented in the WIMS [46], and PEACH [47] MoC transport codes. These averaged gradients were then used as estimates to the gradient of the scalar flux, which were used to compute the source shape as spatially linear.

Petkov and Takeda devised a LSA that estimated the gradient of the scalar flux based on the P_1

approximation in the MARIKO code [44, 48]. In this approximation, the gradient of the scalar flux is computed from the neutron current, the total cross section, and the linearly anisotropic scattering matrix:

$$\boldsymbol{\nabla}\phi_i^g \approx -3\left(\Sigma_{t,i}^g \boldsymbol{J}_i^g - \sum_{g'} \Sigma_{s,1,i}^{g'\to g} \boldsymbol{J}_i^{g'}\right). \tag{3.33}$$

A similar approach, using the diffusion approximation to compute the scalar flux gradient, was used in the so called "quasi-linear" source implemented by Rabiti et al. [49]. In this approach, the $\Sigma_{s,1,i}^{g'\to g}$ matrix is diagonalized, turning the P_1 approximation into the diffusion approximation. Due to their basis on the P_1 and diffusion approximations, these early LSAs are inaccurate in situations where more transport-like effects are present. It can be shown, even in simple cases, that this approximation can be predict the opposite direction for the scalar flux gradient.

Santandrea and Sanchez [50] introduced the positive linear and nonlinear surface characteristics scheme, which constructed a linear source by interpolating between source values on the surfaces of cell regions. Various improvements have been made to this surface characteristics scheme for conservation [50], as well as coupling in APOLLO2 [51]. Le Tellier and Hébert [52] introduced a simplification to the linear characteristics scheme for conservation, by using a diamond-differencing scheme. This work was extended by Hébert [53], to include higher-order diamond difference schemes, as well as allowing for acceleration [30].

The most recent LSA examined in this work was introduced as a 2-D general high-order method for unstructured meshes by Masiello et al. [54]. The approximation uses track-based integration, defined in Section 3.1.1, in order to compute spatial moments of the angular flux. This LSA was shown to reduce memory and computation times in 3-D MoC calculations [55]. The general method was simplified in the case of the isotropic and anisotropic LS by Ferrer and Rhodes [14]; this also introduced the "LS-P0" method in which the isotropic source is spatially linear, but the anisotropic source components are spatially uniform within each cell. This LSA was also to be consistent with particle conservation, under certain constraints, and shown to be compatible with CMFD acceleration [15].

As part of this thesis work, significant effort has been spent on improvements to this moment-based LSA in problems with near-void regions [16], and for the multi-physics problems that are of interest in the CASL program [17]. While this method is capable of modeling general spatially linear anisotropic source, previous work has shown that treating only the isotropic source as spatially linear is more practical [14]; thus, the derivation provided in the next section is for such a source.

3.3.2 Derivation

The moment-based LSA assumes the shape of the source, $q^g_{mi}(\boldsymbol{x})$, is spatially linear within each cell, $\mathcal{R}_i$. This can be expressed as

$$q^g_{mi}(\boldsymbol{x}) \approx q^g_{mi} + \boldsymbol{x} \cdot \underline{\widehat{\boldsymbol{q}}}^g_i, \tag{3.34a}$$

where $\underline{\widehat{\boldsymbol{q}}}^g_i$ is a column vector of source spatial expansion coefficients,

$$\underline{\widehat{\boldsymbol{q}}}^g_i \equiv \begin{bmatrix} \widehat{q}^g_{i,x} \\ \widehat{q}^g_{i,y} \\ \widehat{q}^g_{i,z} \end{bmatrix}, \tag{3.34b}$$

and $\boldsymbol{x}$ is the position in *local* coordinates. A similar spatial expansion of the angular moments of the flux can be performed,

$$\phi^{\ell,g}_{i,n}(\boldsymbol{x}) = \overline{\phi}^{\ell,g}_{i,n} + \boldsymbol{x} \cdot \underline{\widehat{\boldsymbol{\phi}}}^{\ell,g}_{i,n}, \tag{3.35}$$

the source can then be expressed as

$$q^g_{mi}(\boldsymbol{x}) = \sum_{g'} \sum_{\ell=0}^{L} \sum_{n=-\ell}^{\ell} R^n_\ell(\widehat{\boldsymbol{\Omega}}_m) \Sigma^{g' \to g}_{s,\ell,i} \phi^{\ell,g'}_{i,n}(\boldsymbol{x}) + \frac{\chi^g_i}{k_{\text{eff}}} \sum_{g'} \nu \Sigma^{g'}_{f,i} \phi^{g'}_i(\boldsymbol{x}), \tag{3.36}$$

and the linear expansion coefficients are explicitly given by

$$\underline{\widehat{\boldsymbol{q}}}^g_i = \sum_{g'} \sum_{\ell=0}^{L} \sum_{n=-\ell}^{\ell} R^n_\ell(\widehat{\boldsymbol{\Omega}}_m) \Sigma^{g' \to g}_{s,\ell,i} \underline{\widehat{\boldsymbol{\phi}}}^{\ell,g'}_{i,n} + \frac{\chi^g_i}{k_{\text{eff}}} \sum_{g'} \nu \Sigma^{g'}_{f,i} \underline{\widehat{\boldsymbol{\phi}}}^{g}_{g'}. \tag{3.37}$$

In the spatial moment-base LSA, it is convenient to define the spatially linear source (and flux) in terms of a cell-local coordinate system. Allow $\boldsymbol{X}$ to be the position variable in the global coordinate system, the local coordinates are then defined as

$$\boldsymbol{x} = \boldsymbol{X} - \boldsymbol{X}^{\text{c}}_{mi}, \tag{3.38}$$

where $\boldsymbol{X}^{\text{c}}_{mi}$ is the numerical centroid of the cell i.

These numerical centroids can be defined as either direction-dependent, or direction-independent, which will have implications on particle conservation, as discussed in Section 3.3.3. The direction-dependent centroids are defined by

$$\boldsymbol{X}^{\text{c}}_{mi} \equiv \langle \boldsymbol{X} \rangle_{mi} = \frac{1}{V_i} \sum_k \delta A_{mki} t_{mki} \boldsymbol{X}^{\text{c}}_{mki}, \tag{3.39}$$

where $\boldsymbol{X}^{\mathrm{c}}_{mki}$ is the global coordinate vector of the track-segment mid-point. Similarly, the direction-independent centroids are defined by

$$\boldsymbol{X}^{\mathrm{c}}_{i} \equiv \frac{1}{4\pi}\langle \boldsymbol{X} \rangle_{i} = \frac{1}{V_i}\sum_{m} w_m \sum_{k} \delta A_{mki} t_{mki} \boldsymbol{X}^{\mathrm{c}}_{mki}. \tag{3.40}$$

Following the same approach as the FSMoC derivation, in Section 3.2.1, computing the source the region-averaged flux moment, $\overline{\phi}^{\ell,g}_{i,n}$, and the flux expansion coefficients, $\underline{\widehat{\phi}}^{\ell,g}_{i,n}$, are required. The region-averaged flux moment can be found using the same definition as previously,

$$\overline{\phi}^{\ell,g}_{i,n} \equiv \left\langle R^n_\ell(\widehat{\boldsymbol{\Omega}})\psi^g \right\rangle_i = \frac{4\pi}{V_i}\sum_{m} w_m R^n_\ell(\widehat{\boldsymbol{\Omega}}_m) \sum_{k} \delta A_{mki} t_{mki} \langle \psi^g \rangle_{mki}. \tag{3.41a}$$

In order to determine the spatial expansion coefficients of the flux moments, Eq. (3.35) is operated on by $\left\langle R^n_\ell(\widehat{\boldsymbol{\Omega}})(\cdot)\boldsymbol{x}^T \right\rangle_i$. Recognizing that this should be directly proportional to angular flux operated on by $\left\langle R^n_\ell(\widehat{\boldsymbol{\Omega}})\psi^g\boldsymbol{x}^T \right\rangle_i$, a system of equations is found

$$\boldsymbol{M}_i \underline{\widehat{\boldsymbol{\phi}}}^{\ell,g}_{i,n} = \left\langle R^n_\ell(\widehat{\boldsymbol{\Omega}})\boldsymbol{x}\psi^g \right\rangle_i, \tag{3.41b}$$

where

$$\boldsymbol{M}_i \equiv \left\langle \boldsymbol{x}^T\boldsymbol{x} \right\rangle_i. \tag{3.41c}$$

The spatial angular flux moments, $\left\langle R^n_\ell(\widehat{\boldsymbol{\Omega}})\boldsymbol{x}\psi^g \right\rangle_i$, are then defined as

$$\left\langle R^n_\ell(\widehat{\boldsymbol{\Omega}})\boldsymbol{x}\psi^g \right\rangle_i = \frac{4\pi}{V_i}\sum_{m} w_m R^n_\ell(\widehat{\boldsymbol{\Omega}}_m) \sum_{k} \delta A_{mki} t_{mki} \left(\boldsymbol{x}^{\mathrm{in}}_{mki}\langle \psi^g \rangle_{mki} + \widehat{\boldsymbol{\Omega}}_m \langle t_m \psi^g \rangle_{mki}/\xi_{mi} \right). \tag{3.41d}$$

In order to evaluate the flux moments defined in Eq. (3.41), the track-averaged angular flux values, $\langle \psi^g \rangle_{mki}$, and $\langle t_m\psi^g \rangle_{mki}$, must be determined. First, the transport equation must be put into characteristic form, using Eq. (3.16c) the spatially expanded source, Eq. (3.34a), can be defined along the characteristic. The characteristic transport equation becomes

$$\left[\frac{\mathrm{d}}{\mathrm{d}t_m} + \Sigma^g_{t,i} \right] \psi^g_{mki}(s) = \overline{q}^g_{mki} + \widehat{q}^g_{mi}\left(t_m - \frac{t_{mki}}{2} \right), \tag{3.42a}$$

where

$$\overline{q}^g_{mki} \equiv \frac{1}{4\pi}\left[q^g_{mi} + \boldsymbol{x}^{\mathrm{c}}_{mki} \cdot \underline{\widehat{\boldsymbol{q}}}^g_i \right], \tag{3.42b}$$

and

$$\widehat{q}^{g}_{mi} \equiv \frac{1}{4\pi}\left[\frac{\widehat{\mathbf{\Omega}}_m \cdot \widehat{\underline{\boldsymbol{q}}}^{g}_{i}}{\xi_{mi}}\right]. \tag{3.42c}$$

This can be solved analytically for the angular flux along the track,

$$\psi^{g}_{mki}(s) = \psi^{g,\text{in}}_{mki} + \left(\frac{\overline{q}^{g}_{mki}}{\Sigma^{g}_{t,i}} - \psi^{g,\text{in}}_{mki}\right) F_1(\tau^{g}_{m}) + \frac{\widehat{q}^{g}_{mi}}{2(\Sigma^{g}_{t,i})^2} F_2(\tau^{g}_{m}), \tag{3.43a}$$

where

$$F_1(\tau^{g}_{m}) \equiv 1 - \exp(-\tau^{g}_{m}), \tag{3.43b}$$

and

$$F_2(\tau^{g}_{m}) \equiv 2[\tau^{g}_{m} - F_1(\tau^{g}_{m})] - \tau^{g}_{mki} F_1(\tau^{g}_{m}). \tag{3.43c}$$

As discussed in Section 3.2.1, there are two *equivalent* methods with which one could determine the track-averaged angular flux values. However, it is the author's opinion that defining these moments implicitly, by taking the moments of the characteristic equation (Eq. (3.42a)), results in a form that is simpler. The original basis of this work [14], evaluated the linear moment explicitly; for brevity, the derivation will only be shown here with the implicitly defined moment. Previous work [17] has also shown that by using the form given by the implicit definition, there are significant benefits in multi-physics applications. The implicitly defined moments, given by operating on Eq. (3.42a) by $\langle(\cdot)\rangle_{mki}$ and $\langle t_m(\cdot)\rangle_{mki}$, are given by

$$\langle \psi^{g} \rangle_{mki} = \frac{\overline{q}^{g}_{mki}}{\Sigma^{g}_{t,i}} + \frac{\Delta\psi^{g}_{mki}}{\tau^{g}_{mki}}, \tag{3.44a}$$

and

$$\langle t_m \psi^{g} \rangle_{mki} = \frac{\langle \psi^{g} \rangle_{mki} - \psi^{g,\text{out}}_{mki}}{\Sigma^{g}_{t,i}} + \frac{t_{mki}}{2}\left[\frac{\overline{q}^{g}_{mki}}{\Sigma^{g}_{t,i}} + \frac{\widehat{q}^{g}_{mi}}{\Sigma^{g}_{t,i}}\frac{t_{mki}}{6}\right]. \tag{3.44b}$$

Due to the presence of the $\Delta\psi^{g}_{mki}/\tau^{g}_{mki}$ term in Eq. (3.44b), it is beneficial to stability and performance [16, 17] to compute this quantity directly, rather than computing $\Delta\psi^{g}_{mki}$ (as is done for FSMoC). This can be found explicitly by subtracting Eq. (3.43a) evaluated at the exiting location from $\psi^{g,\text{in}}_{mki}$ and dividing by τ^{g}_{mki}, to get

$$\frac{\Delta\psi^{g}_{mki}}{\tau^{g}_{mki}} = \left(\psi^{g,\text{in}}_{mki} - \frac{\overline{q}^{g}_{mki}}{\Sigma^{g}_{t,i}}\right) E_1(\tau^{g}_{mki}) - \frac{t_{mki}}{2}\frac{\widehat{q}^{g}_{mi}}{\Sigma^{g}_{t,i}} T_2(\tau^{g}_{mki}), \tag{3.45a}$$

where

$$E_1(\tau^{g}_{mki}) \equiv \frac{F_1(\tau^{g}_{mki})}{\tau^{g}_{mki}}, \tag{3.45b}$$

$$T_2(\tau^g_{mki}) \equiv 2E_2(\tau^g_{mki}) - E_1(\tau^g_{mki}), \tag{3.45c}$$

and

$$E_2(\tau^g_{mki}) \equiv \frac{1 - E_1(\tau^g_{mki})}{\tau^g_{mki}}. \tag{3.45d}$$

3.3.3 Particle Conservation

In consideration to particle balance, use of the LSA results in additional constraints on the calculations. Similarly to Section 3.2.2, the track-based integration of the source must exactly integrate to the spatial and angular moments of the source. The conservation of spatial moments is the basis of this LSA [15], so this constraint is satisfied without additional constraints on the method. The angular moment constraint is expressed as

$$\frac{1}{4\pi}\left\langle R^n_\ell(\widehat{\boldsymbol{\Omega}}) q^g_{mi}(\boldsymbol{x}) \right\rangle_i = q^{g,n}_{i,\ell}. \tag{3.46}$$

In addition to the constraints introduced in Section 3.2.2, namely direction-dependent renormalization, and directional quadrature restrictions, this places constraints on the definition of the local coordinate system:

$$\langle \boldsymbol{x} \rangle_{mi} = 0. \tag{3.47}$$

This is equivalent to stating that the local coordinate system must be defined with respect to direction-dependent global centroids, as is given by Eq. (3.39).

If these constraints are satisfied, Eq. (3.41) can be simplified,

$$\phi^g_i = \frac{q^g_i}{\Sigma^g_{t,i}} + \frac{4\pi}{V_i \Sigma^g_{t,i}} \sum_m w_m \sum_k \delta A_{mki} \Delta\psi^g_{mki}, \tag{3.48a}$$

$$\overline{\phi}^{\ell,g}_{i,n} = \frac{\overline{q}^{g,n}_{i,\ell}}{\Sigma^g_{t,i}} + \frac{4\pi}{V_i \Sigma^g_{t,i}} \sum_m w_m R^n_\ell(\widehat{\boldsymbol{\Omega}}_m) \sum_k \delta A_{mki} \Delta\psi^g_{mki}, \tag{3.48b}$$

and

$$\begin{aligned}\left\langle \boldsymbol{x} R^n_\ell(\widehat{\boldsymbol{\Omega}}) \psi^g \right\rangle_i = &\sum_m w_m R^n_\ell(\widehat{\boldsymbol{\Omega}}_m) \boldsymbol{M}_{mi} \frac{\widehat{\overline{\boldsymbol{q}}}^g_{mi}}{\Sigma^g_{t,i}} \\ &+ \frac{4\pi}{V_i \Sigma^g_{t,i}} \sum_m w_m R^n_\ell(\widehat{\boldsymbol{\Omega}}_m) \sum_k \delta A_a \left[\boldsymbol{x}^{\text{in}}_{mki} \Delta\psi^g_{mki} + \widehat{\boldsymbol{\Omega}}_m s_{mki} \left(\frac{\Delta\psi^g_{mki}}{\tau^g_{mki}} - \psi^{g,\text{out}}_{mki} + \frac{\overline{q}^g_{mki}}{\Sigma^g_{t,i}} \right) \right]\end{aligned} \tag{3.48c}$$

where

$$\Delta\psi^g_{mki} \equiv \psi^{g,\text{in}}_{mki} - \psi^{g,\text{out}}_{mki}, \tag{3.48d}$$

and

$$\boldsymbol{M}_{mi} \equiv \left\langle \boldsymbol{x}^T \boldsymbol{x} \right\rangle_{mi}. \tag{3.48e}$$

3.3.4 Spatial and Isotropic Simplifications

The work introducing the original formulation of the moment-based LSA suggests that it is beneficial to allow only the isotropic moments of the source and flux to be spatially linear, while higher order moments are spatially flat. The reformulation introduced as part of this work [17] was extended to make this simplification in the so called linear isotropic flat anisotropic (LIFA) source [CITATION]. The linear moment equations can then be simplified to

$$\left\langle \boldsymbol{x}\psi^g \right\rangle_i = \boldsymbol{M}_i \frac{\widehat{\boldsymbol{q}}^g_i}{\Sigma^g_{t,i}} + \frac{4\pi}{V_i \Sigma^g_{t,i}} \sum_m w_m \sum_k \delta A_a \left[\boldsymbol{x}^{\text{in}}_{mki} \Delta\psi^g_{mki} + \widehat{\boldsymbol{\Omega}}_m s_{mki} \left(\frac{\Delta\psi^g_{mki}}{\tau^g_{mki}} - \psi^{g,\text{out}}_{mki} + \frac{\overline{q}^g_{mki}}{\Sigma^g_{t,i}} \right) \right]. \tag{3.49}$$

In the case of an isotropic source, the constraints for particle balance are relaxed. Track-length renormalization as well as numerical centroid definitions can be direction-independent while still preserving particle conservation [15], as given by Eq. (3.20), and Eq. (3.40) respectively. The calculation of angular flux spatial moments, given in Eq. (3.48c), can also be simplified into the form

$$\left\langle \boldsymbol{x}\psi^g \right\rangle_i = \boldsymbol{M}_i \frac{\widehat{\boldsymbol{q}}^g_i}{\Sigma^g_{t,i}} + \frac{4\pi}{V_i \Sigma^g_{t,i}} \sum_m w_m \sum_k \delta A_a \left(\widehat{\boldsymbol{\Omega}}_m s_{mki} \left[\frac{\Delta\psi^g_{mki}}{\tau^g_{mki}} - \psi^{g,\text{out}}_{mki} \right] + \boldsymbol{x}^{\text{in}}_{mki} \Delta\psi^g_{mki} \right). \tag{3.50}$$

3.3.5 Applications

Various different LSAs to the MoC have been developed and implemented in transport codes [7, 14, 16, 44, 46, 47, 49, 50]. Result have indicated that by using a LSA, the spatial mesh discretization can be made coarser, relative to with a FSA, while maintaining accuracy. Although each segment calculation is more expensive when using a LSA, the number of calculations (due to the coarser spatial mesh) can be significantly reduced, leading to reduced run-times. Additionally, the reduction in spatial mesh elements generally reduces the amount of memory used by the calculation. As part

of this work, a spatial mesh discretization study was performed on problems with multi-physics applications in mind [17]; this is presented in more detail in Section 6.1.

3.4 Parallelism

High-fidelity transport methods, such as the MoC, can require significant computational resources for full core calculations; this is particularly true for 3-D calculations. While processing power has increased exponentially since the MoC was first conceived in 1972 [10], since the early 2000's, single-core processing power has largely leveled off. System architectures, as well as code design, have become more focused on *parallel* computations. Previous works [11] made significant progress in the efficient parallelization of the MoC.

Kochunas [11] developed a hybrid-parallel algorithm for the MoC that included thread-based parallelism over characteristic tracks, as well as spatial and angular decomposition. This work showed that the MoC was able to scale well up to 10000's of processors. While this work is important, and has led to significant advancement, the use of 1000's of processors is not feasible for industrial use. It is thus the author's opinion that the primary focus of research on 3-D MoC techniques should be on serial efficiency, such as the Linear Source (LS) (Section 3.3), and macroray (Section 4.4.4); however, moderate levels of parallelism are feasible for industry, and so more efficient parallelism should also be a focus of research.

In MoC calculations, each characteristic track calculation is nearly independent from others; previous works have indicated that loops over characteristic tracks can be parallelized efficiently by using threads on traditional central processing units (CPUs) [11] or on general purpose graphics processing units (GPGPUs) [7]. This type of parallelism is most generally called *shared-data parallelism*, as data is shared between the parallel threads.

Large neutronics calculations may require significant amounts of memory, and thus *distributed-data parallelism* is necessary. In general, this type of parallelism separates (partitions) a domain of the problem, and separate computing nodes are assigned a subdomain. Only data for the assigned subdomain is stored, and thus whole-core simulations become possible; additionally, because each subdomain can be processed in parallel, overall runtimes typically decrease with increasing numbers of subdomains (processors).

MPACT has the capabilities for domain decomposition/parallelism over two separate domains: space and direction. In MPACT, each discrete direction has an easily calculable amount of work, and the decomposition is trivial; in general the same cannot be said of the spatial domain. As part of this thesis work, a more efficient method of spatial decomposition has been investigated and developed in MPACT [22]. A journal article on this work has been submitted to the Annals of Nuclear Energy; for now, the submitted manuscript is attached in **??**.

CHAPTER 4

Ray-Tracing

The Method of Characteristics (MoC) [10] is based on solving the transport equation along many characteristic tracks or rays. These rays are followed through the reactor geometry in a process generally referred to as "ray-tracing". The placement and storage of these tracks is significant with respect to both calculation accuracy as well as computational performance. This section servers to give an overview of the ray-tracing methods that have been developed, as well as motivate the use of the proposed 3-D "MacroRay" ray-tracing method.

4.1 Modular Ray-Tracing

The most straight-forward approach to perform a MoC calculation is to create rays which span the domain of the transport problem being solved. However, in this approach, the information of each ray-segment must be stored, or computed on-the-fly. In large problems the number of ray-segments can become exceedingly large, and this approach is not feasible due to memory constraints.

This led to the development of so-called "modular" ray-tracing methods [11, 39, 56, 57], in which the regularity of reactor designs is utilized to reduce memory usages. In typical reactor designs, certain geometries (like assemblies) are repeated throughout the core. Rather than laying tracks down for the global geometry, the transport problem is partitioned into "modules" which represent a small often repeated geometries in the problem. The ray-tracing data is generated for each module, in such a way there is direct linking of tracks on module interfaces; this is the direct neutron path linking (DNPL) technique devised by Kosaka and Saji [39]. This significantly reduces the amount of ray-tracing data that needs to be stored in MoC calculations, and has been widely adopted in MoC transport codes [4, 38, 47, 58–61]. Tracks spanning the global domain are then constructed by connecting multiple modular rays, as is depicted in Fig. 4.1.

The modular ray-tracing technique, with DNPL, requires that the number of tracks on a modular boundary is an integer. This additionally requires that all modules have the same spatial dimensions, given by the pitches P_x and P_y, and that the spacing between all tracks in a direction are constant.

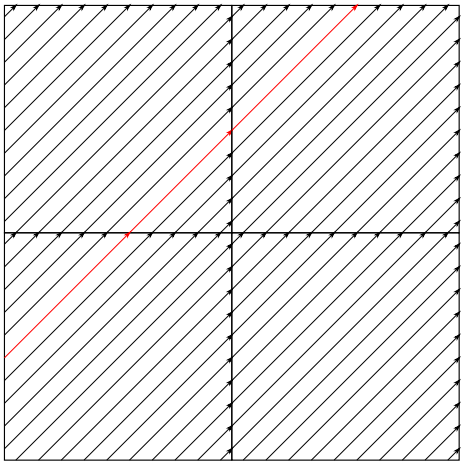

Figure 4.1: Depiction of modular ray-tracing method. Global (long) rays can be constructed by connecting multiple modular rays, as is shown in red.

Let δA_{a0} be the desired ray-spacing for an azimuthal angle a, and φ_{a0} be the desired azimuthal angle. The number of rays on the x and y module boundaries can be determined as

$$N_x = \left\lceil \frac{P_x \sin(\varphi_{a0})}{\delta A_{a0}} \right\rceil, \tag{4.1a}$$

and

$$N_y = \left\lceil \frac{P_x \cos(\varphi_{a0})}{\delta A_{a0}} \right\rceil. \tag{4.1b}$$

The x and y distance between rays can be determined by

$$\delta_x = \frac{P_x}{N_x}, \tag{4.2a}$$

and

$$\delta_y = \frac{P_y}{N_y}. \tag{4.2b}$$

The azimuthal angle is then "corrected" to represent the true angle at which the rays are placed,

$$\varphi_a = \tan^{-1}\left(\frac{\delta_y}{\delta_x}\right), \tag{4.3}$$

and the corrected ray-spacing is then given by

$$\delta A_a = \delta_x \sin(\varphi_a). \tag{4.4}$$

Due to the constraint of DNPL, the directional quadrature is perturbed in the process of ray-tracing. As described in Section 3.2.2, this has implications on particle conservation in calculations. To maintain accuracy, a higher-order directional quadrature may need to be used would otherwise have been necessary.

4.2 Mobile Chords

The mobile chord method was introduced by Villarino et al. [18] in the HELIOS code for CP calculations, and adapted to the MoC by Yamamoto [62]. In the typical equidistant ray-tracing method, a ray is placed at the center of the ray-width. The mobile chord method offsets the ray from the center, with differing offsets in each direction. This has generally shown to be more accurate than the typical equidistant ray-tracing method [62], but is not directly compatible with the DNPL technique. While ray widths are still linked, the ray-traces are not; though, this does not seem to introduce significant discretization errors [62].

4.3 Macroband

The *macroband* method was originally proposed by Villarino et al. [18] for CP calculations in HELIOS. In this method, characteristic rays placed within "macrobands" which are separated by tangential and intersection points in the mesh. There is no material or geometric discontinuities within each macroband segment (macrosegment), and thus the direction-of-flight averaged angular flux in each macrosegment is smooth with regards to the transverse direction. Since integration in the MoC is akin to a quadrature integration, this indicates that a more advanced quadrature, for ray placement and width, can be used to reduce discretization error [19].

Macrobands are determined by the computational mesh; for large heterogeneous assemblies, this results in very thin macrobands, which would result in significantly increased computation time. In the related CDP Hong and Cho [28] proposed that macroband ray-tracing data only be generated on unique subsystems. Similarly, Yamamoto et al. [19] proposed the memory reduction technique for macroband (MRMB) in which macroband ray-tracing data is only generated for unit-cells. These techniques are similar to the modular ray-tracing technique in that ray-tracing data is only generated for unique subsystems, which significantly reduces the amount of ray-tracing data. The macroband ray-tracing process is displayed for a single pin-cell mesh in Fig. 4.3.

However, these techniques are fundamentally incompatible with the DNPL technique, at thus an approximation of angular flux must be made on subsystem interfaces. Yamamoto et al. [19] proposed linearly interpolating the angular flux on cell boundaries, though other techniques involving

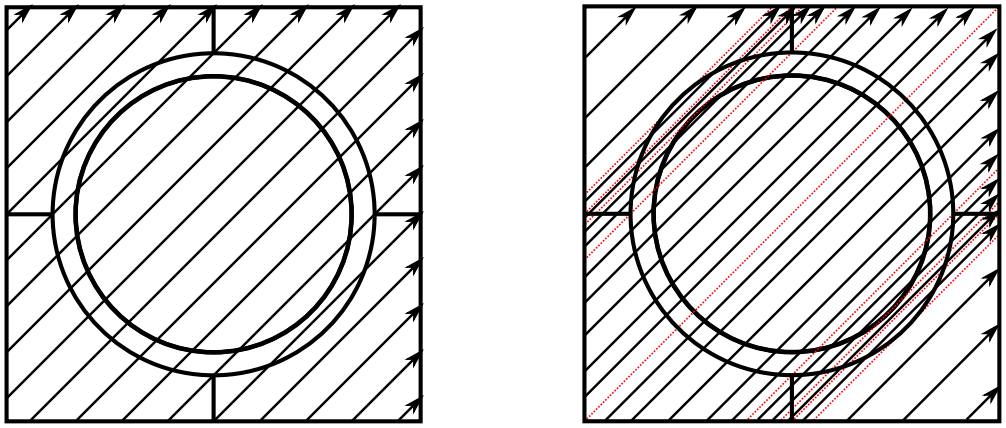

(a) Equidistant (b) Macroband

Figure 4.2: Visualization of hypothetical tracks for (a) equidistant and (b) macroband ray-tracing methods. Boundaries between macrobands are shown as red dotted lines.

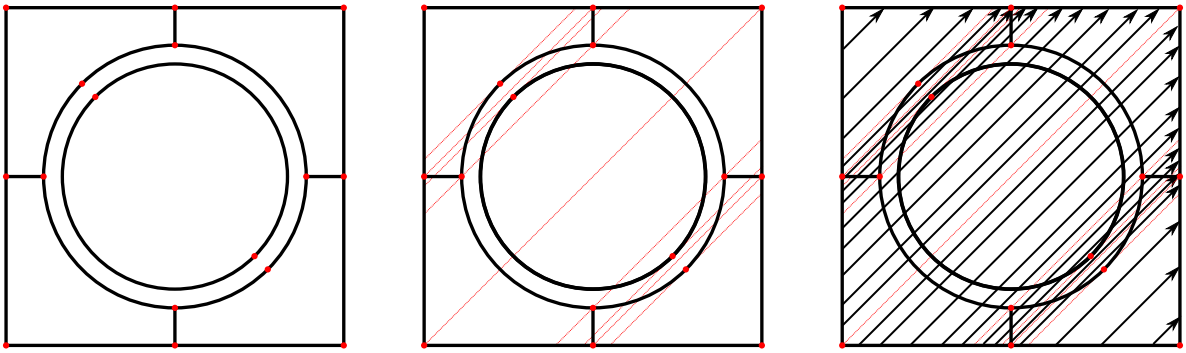

(a) Determine intersection and tangent points (b) Determine macroband boundaries (through identified points) (c) Perform ray-tracing within macroband boundaries

Figure 4.3: Ray-tracing process for macroband.

averaging the angular flux on sub-boundaries have been utilized in the CDP [29]. Alternatively, these methods do not require adjustment to the angular quadrature.

Yamamoto et al. [19] found that the macroband method (using a Gauss-Legendre quadrature for ray placement), was more accurate than conventional ray-tracing methods with equidistant ray-spacing. Févotte et al. [20] proposed a new tracking technique similar to the macroband method, in which rays (placed equidistantly) are divided into sub-bands, which are effectively *locally* projected macrobands, and the average flux of the sub-bands is propagated along each ray. Studies of ray-spacing with macroband, and Févotte et al.'s [20] method, have indicated that coarser ray-spacing can be used while maintaining accuracy [19, 20, 62].

4.4 Three-Dimensional Ray-Tracing Techniques

The MoC is naturally extended to three-dimensional calculations along characteristic tracks spanning three-dimensions. However, 3-D MoC presents significant computational challenges. This has led to significant research effort into developing more efficient approaches to three-dimensional MoC [11, 63–66]. One of the main focuses of this research has been in reducing the complexity introduced by three-dimensional ray-tracing.

4.4.1 3-D Modular Ray-Tracing

In three-dimensional MoC calculations, characteristic rays must be laid down through the three-dimensional domain; Generally, three-dimensional tracks are generated by first creating a set to two-dimensional tracks, and generating three-dimensional tracks that project onto these two-dimensional tracks [11, 67]. The generation of these two-dimensional tracks can be simplified as viewing each of the two-dimensional tracks as a plane in the axial and characteristic directions, z and s respectively. Three-dimensional tracks are then produced by performing two-dimensional ray-tracing on this characteristic plane [11], as is shown in Fig. 4.4

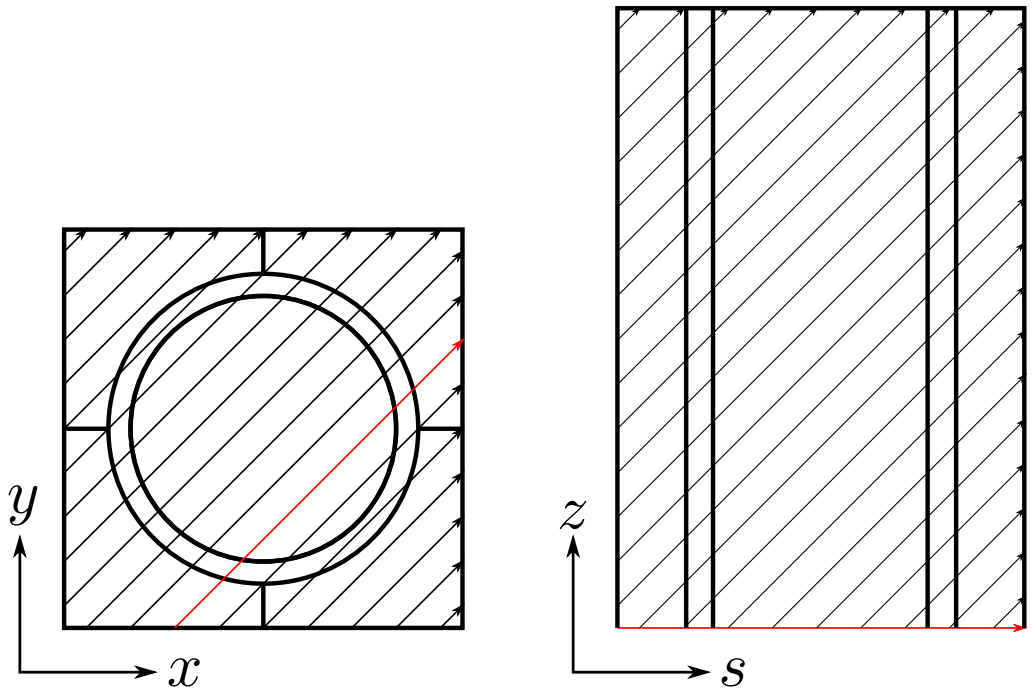

Figure 4.4: 3-D ray-tracing process. Generate 2-D tracks, these become characteristic planes. Along each plane, perform 2-D ray-tracing. The highlighted (red) characteristic track in the 2-D pin-cell on the left becomes the characteristic plane on the right.

There are subtleties in the generation of three-dimensional tracks, which have led to the development of different 3-D modular ray-tracing techniques [11, 67]. Previous work had reported that direct use of the modular ray-tracing (MRT) method in 3-D, required that tracks be stored separately for the forward and backward directions [11]; this has, however, been shown not to be the case [67]. The simplified MRT was developed to avoid this issue [11], but generates significantly more characteristic tracks [67].

As discussed in Section 4.1, 2-D MRT perturbs the azimuthal angles in the directional quadrature to ensure DNPL. For 3-D MRT, this also perturbs the polar angles in the directional quadrature. Kochunas [11] also found that modularization of the directional quadratures led to clustering of the discrete directions, which introduces significant error in the integration of spherical harmonics moments [11], and has implications on particle conservation in anisotropic calculations (Section 3.2.2). In order to avoid this issue, the axial ray-spacing can be reduced until the modularized polar angle is only perturbed within some error criteria [11]; however, this leads to significant increases in the number of tracks (and thus increases computational costs).

4.4.2 Chord-Classification

While MRT significantly reduces the storage requirements of ray-tracing data, in realistic calculations, the data cannot fully be stored in a processors cache. Loading this data from main memory is slow, and in general, the movement of this ray-tracing data into different levels of cache uses significant amounts of time in these calculations. This led to the development of a technique called *chord-classification* for locally axially extruded geometries [12]. Chord-classification recognizes that reactors typically have regularities in the 3-D geometries; this allows for characteristic track-segments to be classified into sets which share the same length. As shown in Fig. 4.5, rays on the same characteristic plane that intersect two vertical mesh boundaries will have the same lengths. Similarly for rays which intersect horizontal planes (though, as axial meshes are usually tall, this is not as common).

By classifying chords of the same length, the length can be stored only once. Additionally, this means that the exponential functions ($F_1(\tau^g_{mki})$ for FSMoC), only need to be calculated once as well. This adds irregularity to the data accessing, which is generally not optimal for computation, and thus is only expected to improve calculation speeds if a large number of chords can be classified [12]. Indeed, it was observed that most rays (96%) could be categorized as "V-chords" which intersect two vertical surfaces, which led to a 40% reduction in transport sweep time [12].

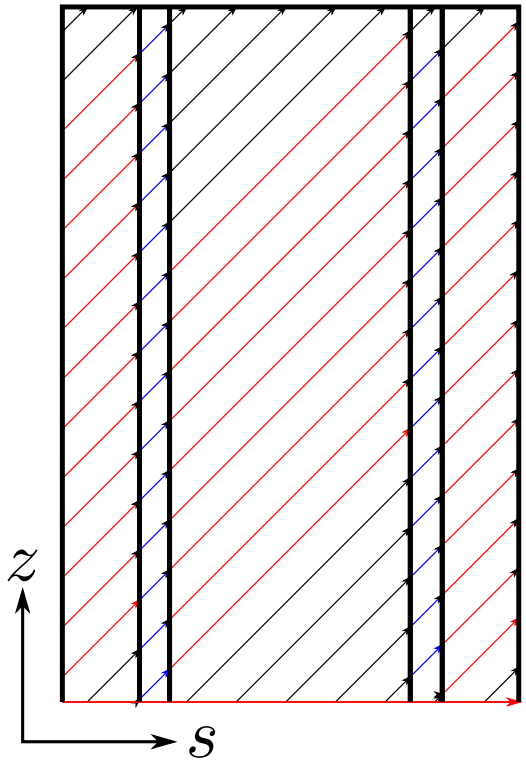

Figure 4.5: 3-D example of chord-classification. Colored (red and blue) characteristic tracks represent groups of "V-chords", rays between two vertical surfaces.

4.4.3 On-the-Fly Ray-Tracing

The on-the-fly ray-tracing technique [13] uses some of the ideas of the chord-classification method [12], and only stores two-dimensional track information. All three-dimensional tracks are generated and temporarily stored during the transport sweep (on-the-fly), leading to significant memory savings (94% reduction), with minimal computational overhead [13].

4.4.4 Macroray

The *macroray* method is a three-dimensional extension of the two-dimensional macroband method. This method is currently being implemented as part of this work, and, to the best of the author's knowledge, has never been studied. The name has been changed to the more general "macroray" as three-dimensional tracks are no longer two-dimensional "bands".

The motivation for investigating this method is for three primary reasons. The first, is that 2-D results [19, 20, 62] have indicated that the macroband method allows for coarser ray-spacing (thus fewer rays) while maintaining accuracy. This is expected to increase computational efficiency, and lead to faster MoC calculations. However, an extension to three-dimensions, if coarser ray-spacing

can be used in both the axial and radial directions, the increase in computational efficiency is expected to be greater.

Second, MRT methods require adjustments to the directional quadrature, which is expected to decrease accuracy of numerical integrals over directions [11]. The macroband and macroray methods require no such adjustment. Typically, it is the polar angle that has a more advanced quadrature (Gauss-Legendre, or Tabuchi-Yamamoto [25]), and is thus more sensitive to perturbations than the azimuthal angles. Without the perturbation of the polar (and azimuthal) quadratures, it may be possible to maintain accuracy while using fewer directions than is possible with 3-D MRT methods.

Finally, MRT methods require that the same ray-spacing parameters are used throughout the entire problem domain. Problems which have strong absorbers typically require a very fine mesh [17], which then requires that finer ray-spacing be used. This finer ray-spacing, which may only be required for a small percentage of the problem domain, is then used for the entire domain, leading to a significant increase in the number tracks. The macroband and macroray methods allow for use of different ray-spacing parameters in each subsystem; additionally, because macrobands are based on the computational mesh, an effectively finer ray-spacing will automatically be generated due to the fine spatial mesh. This allows for densely spaced tracks where they are necessary, but more coarsely spaced tracks where they are not; this is expected to lead to significant reduction in the number of tracks in such problems.

Another consideration in three-dimensional locally axial extruded geometries is the chord-classification method. In the macroray method, rays are separated into the macrorays, which are guaranteed to be of the same class in the chord-classification method; this macroray classification is depicted in Fig. 4.6

4.4.5 Other Approaches

Giho et al. [68] proposed the axially simplified MoC in three-dimensional calculations, which examines characteristic planes (two-dimensional tracks). Along these characteristic planes, an axially extruded geometry becomes a rectilinear mesh. The angular flux on the edges of these rectilinear cells is averaged, and a transport calculation is performed using the angular-dependent transmission probability method [69]. The Legendre polynomial expansion of angular flux (LEAF) method [64] is an extension of the axially simplified MoC, where the angular flux on cell boundaries is expanded in Legendre polynomials. In the LEAF method, the source is also expanded in terms (up to second order) of Legendre polynomials.

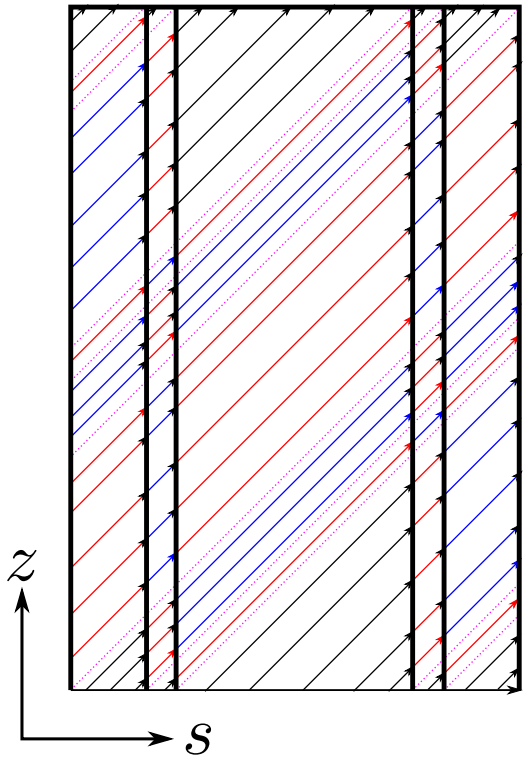

Figure 4.6: 3-D example of chord-classification with Macroray ray-tracing. Colored (red and blue) characteristic tracks represent groups of "V-chords", rays between two vertical surfaces.

4.5 Transport Sweeping with the Method of Characteristics

The MoC is used to iteratively solve the transport equation, the iterations are generally referred to as *transport sweeps*. For given boundary conditions and source, a transport sweep is used to compute estimates of the scalar flux and other moments using equations in the form Eq. (3.31) for FSMoC and Eq. (3.48) for LSMoC. This is an overly generalized description of a transport sweep, and there are considerations that arise from the different ray-tracing techniques discussed.

In global ray-tracking procedures, calculations are most often carried out by examining a ray from end to end. The angular flux at the ends can be found from the boundary conditions. Along each segment, a transmission calculation can be carried out (Eqs. (3.26) and (3.43)), and flux moments can be accumulated. This procedure is shared by the MRT which constructs global rays (long rays) by linking modular rays. This allows for each ray calculation to be carried out in parallel, since each ray calculation is effectively independent [11]; though special considerations must be taken to avoid race-conditions in the accumulation of moments.

However, in the macroband and macroray methods, transport sweeping is carried out in a different manner. It is not possible to generate a continuous characteristic track spanning the global

domain when using MRMB techniques. Thus, transport calculations are carried out in a pin-by-pin (assuming pins are the subsystems on which track data is generated) basis. For each pin calculation, boundary or interface angular flux is loaded, and transmission/accumulation calculations are carried out by sweeping over the tracks. This can be done by considering each track separately, or by considering each macroray which are guaranteed to pass through the same regions. The angular flux on the exiting interface must be approximated, this can be done by interpolation [19], or sub-boundary averaging [29].

Pin-by-pin transport calculations must be carried out in a specific order, by considering the dependencies of angular flux. Figure 4.7 displays the sweeping order for a 2×2 array of pins in 2-D; this order is significantly different than the ray-by-ray order used in traditional MRT-based MoC calculations. Sweeping in this manner limits parallelism, though it may be possible to construct a dependency graph to get an optimal sweeping order considering macrorays individually, rather than on the pin-by-pin basis.

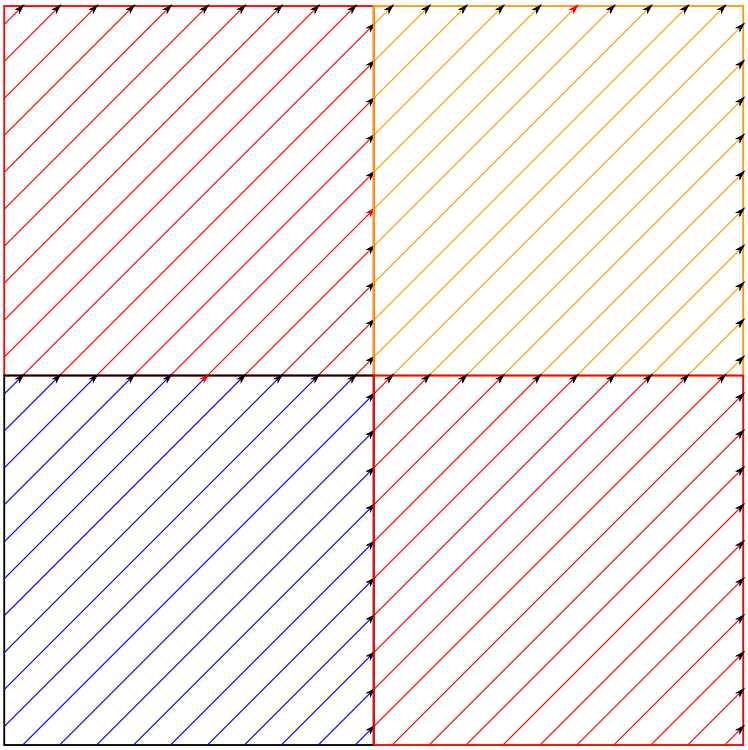

Figure 4.7: Pin-by-pin sweeping order for a 2×2 domain with colors representing the order starting from the bottom left pin.

4.6 Interface Flux Approximations

a

CHAPTER 5

Spatial Decomposition

5.1 Introduction

Until relatively recently, the method of choice for neutronics calculations has been neutron diffusion. Neutron diffusion codes can perform whole-core calculations, on a typical workstation, in relatively short run-times. However, with the recent shift towards higher fidelity methods such as S_N, and MoC [10], more significant computational resources are necessary. These high fidelity methods allow for more detailed analysis, through finer resolution and use of fewer approximations, but typically take far more time to perform calculations; particularly for large calculations. Although processor clock-speeds have significantly improved, in the past several years processors have, for the most part, not gotten faster. To reduce the run-times (real-time) of high fidelity simulations, it is thus necessary to rely on parallelism.

There are many different aspects of parallelism, and thread-based parallelism has been discussed previously Section 3.4. This type of parallelism (thread), is limited to the resources of a single computational node. In order to utilize more resources, it is necessary to use a technique called *domain decomposition*. Even without considerations for run-times, these high-fidelity simulations typically use more memory than is available on a single node, and domain decomposition becomes a necessity. In general, domain decomposition involves splitting up one domain of the problem into smaller subdomains; some typical domains to decompose are space, direction, and energy. Each smaller subdomain is assigned to a separate processor, and these can be run in parallel; although, there is generally some communication between the processors.

In Monte-Carlo simulations, it is common that spatial decomposition involves duplication of some spatial locations [CITATION]. However, in deterministic transport methods, each domain is typically *partitioned*, that is the domain is split without any overlap between subdomains. The MPACT [60] code has the ability to decompose two domains: space and direction. In MPACT, each discrete direction has a calculable amount of work, and the decomposition is trivial; in general, the same cannot be said of the spatial domain. This chapter focuses on improvements to the spatial

decomposition techniques used in MPACT; these techniques, however, can be applied to other transport codes and similar results would be expected. The contents of this chapter are, in large part, adapted from an article published on this work [22].

As diffusion has been the method of choice for so long in the reactor physics field, spatial partitioning techniques common in other fields have, largely, not been applied. Transport codes such as MPACT [60], or OpenMOC [9] used simple spatial partitioning methods that divided the core into uniformly sized blocks. However, the spatial partitioning of a reactor can be abstracted to a graph partitioning problem [21], which has been well studied in computer science [70] and applied to other simulation fields such as computational fluid dynamics [71]. In general, the graph partitioning problem is NP-complete, meaning that a partitioning cannot be easily verified as optimal; therefore, graph partitioning relies on approximate heuristic methods. Many different methods have been developed for graph partitioning, several of which are discussed in Section 5.3.

The remained of this chapter is structured as follows. In Section 5.2, a description of spatial decomposition in MPACT is given. Section 5.3 introduces relevant graph theory concepts, and the methods used for spatial partitioning in this work. Section 5.4 describes the applications of these graph theory methods in MPACT. Section 5.5 compares methods for 2-D and 3-D reactor simulations. Finally, Section 5.7 lists the conclusions that are drawn from this work.

5.2 Spatial Decomposition in MPACT

MPACT is a neutron transport code, based on the MoC. It was originally developed for direct whole-core simulation of LWRs. In the MoC, an approximate transport equation is solved analytically along characteristic rays that traverse the problem. By using many of these characteristic rays, an accurate solution is obtained; however, storing the data of these characteristic rays can use a considerable amount of memory.

In MPACT, the modular ray-tracing technique [39] is used to reduce the memory used for storing characteristic ray information. Modular ray-tracing involves dividing the reactor system into *ray-tracing modules*, which are small geometries that are often repeated in the reactor. Characteristic rays are constructed in each ray-tracing module such that each ray directly links to a ray in an adjacent module. In this method, characteristic ray information is only stored for each *unique* ray-tracing module.

Ray-tracing modules are the smallest unit for spatial decomposition in MPACT [72]. These ray-tracing modules are typically an axial slice of a quarter of a full fuel assembly, as shown in Fig. 5.1 The core consists of a structured grid of these modules in which each module has the same dimensions but may have different numbers of computational cells. Therefore, in MPACT, the spatial decomposition is a structured grid partitioning problem.

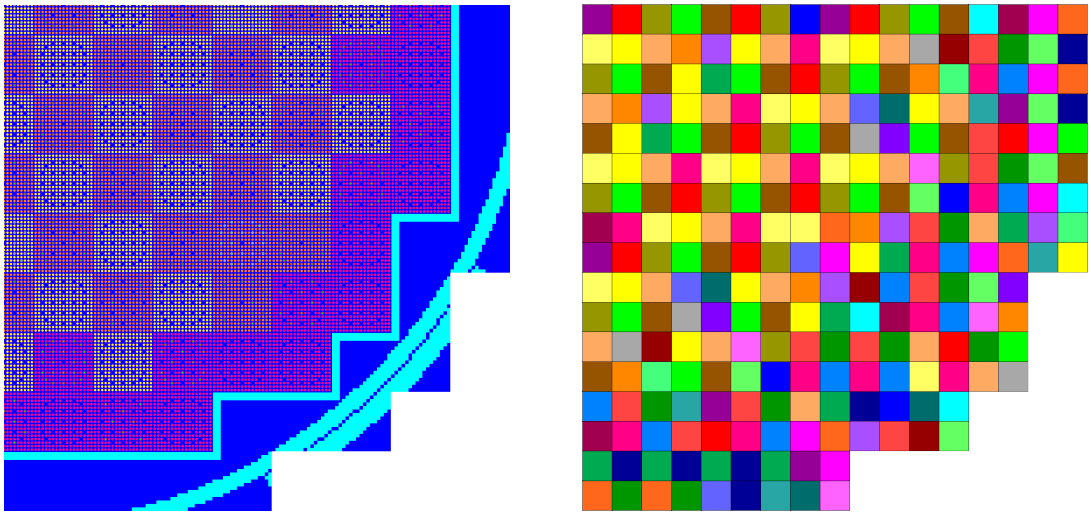

(a) fine mesh (b) ray-tracing module mesh

Figure 5.1: Example quarter core configuration and corresponding ray-tracing modular mesh in MPACT.

In general, it is possible to use the computational cells as the smallest unit in the decomposition. However, this causes the decomposition problem to become an unstructured mesh partitioning problem. This is not done in MPACT because communication would become significantly more complicated. Additionally, there would be more re-entrant rays which would have negative impacts on the rate of convergence.

MPACT has had two spatial decomposition methods in the past: manual decomposition, and assembly-based decomposition. A user may manually enter a decomposition [72], but it is time consuming to construct a balanced decomposition and will likely still be suboptimal to some degree. An automated method exists that recursively bisects the core using Morton-ordering [73] applied to the reactor assembly geometries. While this method is automated, it often yields very imbalanced domains, and also restricts the number of subdomains that can be used.

Previous work has shown that spatial decomposition of reactors can be abstracted to a graph partitioning problem [21]. The use of graph partitioning methods in MPACT is expected to solve the issues encountered in each of the two approaches described above. These methods can be used to decompose into an arbitrary number of domains with high quality results, without user input.

Existing graph partitioning libraries such as METIS [74] partition graphs very efficiently and have very high quality results. To use all given processors, MPACT requires that each spatial subdomain contains at least one module, i.e. no partition can be empty. However, in some cases, particularly when the number of partitions is high, METIS may generate empty partitions. This means METIS cannot be used to decompose the core into an arbitrary number of subdomains without modifying the resulting partitions. For this reason, MPACT does not rely on third-party

libraries for graph partitioning in the spatial decomposition process.

5.3 Applied Graph Theory

The spatial decomposition of a reactor core can be abstracted to the partitioning of a graph. Specifically, this would be a weighted graph, $G(V, E)$, which is comprised of a set of vertices, V, and a set of edges, E, that connect pairs of vertices. In general, these vertices and edges may have weights; a vertex v_i will have weight w_i, and an edge e_i between vertices v_i and v_j will have weight c_{ij}. In MPACT, a vertex represents a ray-tracing module, and the edges represent communication between adjacent modules in the MoC. The graphs are undirected because communication between ray-tracing modules is two-way.

Previous work [21] applied unweighted graph partitioning techniques to the reactor spatial decomposition problem; the work presented here applies generalizations and improvements to the methods used for graphs with weighted vertices and edges. A vertex's weight indicates the amount of computational work that is needed; as one might expect, this is highly correlated with the number of computational cells. This is shown in Section 5.5. In general, the edges may also be weighted to account for different amounts of data transfer. This is discussed in more detail in Section 5.4.

The goal is for each partition to have equal weight, with minimal weight of edges cut by partition boundaries. This is equivalent to each subdomain having the same amount of computational work with minimized communication between processes. If each process has roughly the same amount of work to perform, then less time will be spent waiting for other processes, thus improving parallel efficiency. Also, with less communication, less time will be spent passing data between processes, so the parallel overhead will be reduced.

In this work, methods were separated into two distinct categories: partitioning methods and partition refinement (improvement) methods. Partitioning methods give a near-balanced partitioning for a given graph. Refinement methods attempt to reduce communication between existing partitions in a graph. As applied in MPACT, these refinement methods typically did not significantly reduce communication. These methods and results are presented in **??**.

5.3.1 Graph Partitioning Methods

In this work, recursive partition methods were considered due to their capability to partition into arbitrary numbers of domains. Each of these recursive partitioning methods sorts the graph, using different methods, and then divides or "cuts" the graph into two subgraphs with approximately equal vertex weights. Once a graph's vertices are sorted into a list, V_s, the graph can be bisected using Algorithm 2.

Multi-level partitioning methods are widely used in other fields such as networking, where graphs can become very large; however, in MPACT, the number of ray-tracing modules is on the order of a few hundred to several thousand, which directly correlates to the size of the graph. Additionally, for MPACT, the decomposition problem is static, so the computation time for partitioning is expected to be negligible as it can simply be performed one time at the outset. Due to the small graph size, multi-level methods were not considered as part of this work.

Algorithm 2 The algorithm used to determine how to cut a graph, $G(V, E)$, into two subgraphs based on a sorted vertex list V_s, and that the graph will be recursively partitioned into N groups.

procedure GRAPH CUT($G(V, E), V_s, N$)
  $N_1 \leftarrow \lfloor N/2 \rfloor$ ▷ Desired number of recursive partitions for first subgraph
  $W_1 \leftarrow \frac{N_1}{N} \sum_{v_i \in V} w_i$ ▷ Ideal weight of first subgraph
  Let V_1 be a set of vertices such that:
    - $V_1 \subset V$
    - The vertices V_1 are taken in order from V_s
    - $W_1 - \sum_{v_i \in V_1} w_i$ is minimized
  Let V_2 be the subset $V \setminus V_1$
  Optionally call a refinement method
  Create a graph G_1 from V_1
  Create a graph G_2 from V_2
end procedure

5.3.1.1 Recursive Spectral Bisection

The recursive spectral bisection (RSB) method, originally developed by Pothen et al. [75], has been highly successful and widely used in graph partitioning [76, 77]. This method relies entirely on the connectivity of the graph and not on its geometry. The RSB method has been improved to allow to allow for partitioning of *weighted* graphs into any number of domains [78].

The RSB method makes use of the Laplacian matrix of a graph; specifically the second-smallest eigenvalue of this matrix, referred to by Fiedler as the *algebraic connectivity* [79]. The eigenvector associated with this eigenvalue has also been known as the *Fiedler vector*. For weighted graphs, the weighted Laplacian matrix is used in lieu of the Laplacian matrix; matrix elements are given by

$$L_{ij} = \begin{cases} d_i, & i = j, \\ c_{ij}, & i \neq j, \\ 0, & \text{else}, \end{cases} \tag{5.1}$$

where d_i is the sum of edge weights from vertex v_i, and c_{ij} is the weight of the edge between

vertices v_i and v_j. The Fiedler vector is found from this weighted Laplacian matrix; by sorting the values of the Fiedler vector, the vertices can be reordered in a one-dimensional list V_s. This list of vertices is then divided into two sets, based on weight and total number of partitions needed (see Algorithm 2). The recursive spectral bisection algorithm is listed in Algorithm 3.

Algorithm 3 The recursive spectral bisection (RSB) algorithm.

```
procedure RSB(G(V, E))
    Let L be the weighted Laplacian of G(V, E)
    Compute eigenvectors of L
    Use the Fiedler vector to sort V → V_s        ▷ If tie, use larger eigenvectors
    Cut graph into G_1(V_1, E_1), G_2(V_2, E_2): Algorithm 2
    RSB(G_1(V_1, E_1))
    RSB(G_2(V_2, E_2))
end procedure
```

5.3.1.2 Recursive Inertial Bisection

Another class of recursive partitioning methods are coordinate or geometric methods. There are many different geometric partitioning methods in existence; in this study, the recursive intertial bisection (RIB) method [70, 80] was investigated. This method uses only the geometry of the graph to construct a bisector and does not consider the connectivity (edges) in any way.

The RIB method determines a bisector which cuts the graph into two approximately equally sized subdomains. This is easily generalized for weighted graphs. The bisector should have approximately equal amounts of weight on each side. The RIB makes no assumption of the orientation of the graph in space, unlike some other coordinate partitioning methods. The principle axes of the graph are equivalent to the eigenvectors of the inertial matrix given by

$$\boldsymbol{I} \equiv \sum_{i=1}^{n} w_i \left(\boldsymbol{x}_i - \overline{\boldsymbol{x}}\right)^T \left(\boldsymbol{x}_i - \overline{\boldsymbol{x}}\right), \tag{5.2}$$

where n is the number of vertices, $\boldsymbol{x}_i$ is a row-vector containing coordinates of vertex v_i, and $\overline{\boldsymbol{x}}$ is the mean coordinate vector given by

$$\overline{\boldsymbol{x}} \equiv \frac{\sum_{i=1}^{n} w_i \boldsymbol{x_i}}{\sum_{i=1}^{n} w_i}. \tag{5.3}$$

An approximate bisector is given as passing through the weighted centroid with normal vector given as one of the eigenvectors of $\boldsymbol{I}$.

Other works [70, 80] have used the smallest eigenvalue's eigenvector as a normal vector to

minimize the mean-square distance of vertices from the bisecting line or plane. However, in this work, the largest eigenvalue's eigenvector is used, so a smaller cut-size is typically given while still bisecting the graph into two subdomains of approximately equal weight. This is the case because in the MoC, communication scales with the surface area between adjacent ray-tracing modules. This may not be the case for other computational methods.

In general, a line or plane passing through the weighted centroid with the eigenvector normals will not cut the graph into two equally weighted subdomains. Instead, the vertices will be sorted according to their distance from the approximate bisectors, and then a cut will be made so that near equal amounts of weight are in each set using Algorithm 2. This sorting and cutting based on weights is equivalent to shifting the bisector in the direction of the normal vector. An example is visualized in Fig. 5.2. The RIB algorithm is listed in Algorithm 4.

Algorithm 4 The basic recursive intertial bisection (RIB) algorithm.

procedure RIB($G(V, E)$)
    Compute the weighted centroid of the graph $\overline{\boldsymbol{x}}$, given by Eq. (5.3)
    Shift coordinates relative to centroid: $\boldsymbol{x}_i^c = \boldsymbol{x}_i - \overline{\boldsymbol{x}} \quad \forall i \in V$
    Compute inertial matrix $\boldsymbol{I}$, given by Eq. (5.2)
    Compute eigenvectors of $\boldsymbol{I}$. Largest eigenvalue's eigenvector $\boldsymbol{e}_1$
    Compute distance from largest eigen-pair bisector: $d_i = \boldsymbol{x}_i^c \cdot \boldsymbol{e}_1$
    Sort $V \rightarrow V_s$ based on d_i. ▷ In ties use smaller eigenvalue's eigenvector
    Cut graph into $G_1(V_1, E_1), G_2(V_2, E_2)$: Algorithm 2
    RIB($G_1(V_1, E_1)$)
    RIB($G_2(V_2, E_2)$)
end procedure

5.3.1.3 Recursive Expansion-Based Methods

The recursive expansion bisection (REB) methods comprise the last class of partitioning methods examined in this work. These methods begin a bisection step by selecting a vertex as the starting point of a subdomain. This subdomain is then expanded until it is approximately half the size of the graph [21, 70, 81, 82]. In this work, the method outlined by Fitzgerald et al. [21] was slightly modified and generalized to weighted graphs. For the remainder of this work, the acronym *REB* will be used to denote this specific expansion-based method rather than the entire class of methods.

This REB method considers both the geometry and connectivity of the graph. The method begins by choosing a starting vertex for the subdomain and then expands based on a set of prioritized rules. At each expansion step, the next vertex is chosen so that it is geometrically close to the vertices within the subdomain and to minimize edges between the subdomain and the remaining graph. However, this method makes the assumptions that the mesh is structured, and that every

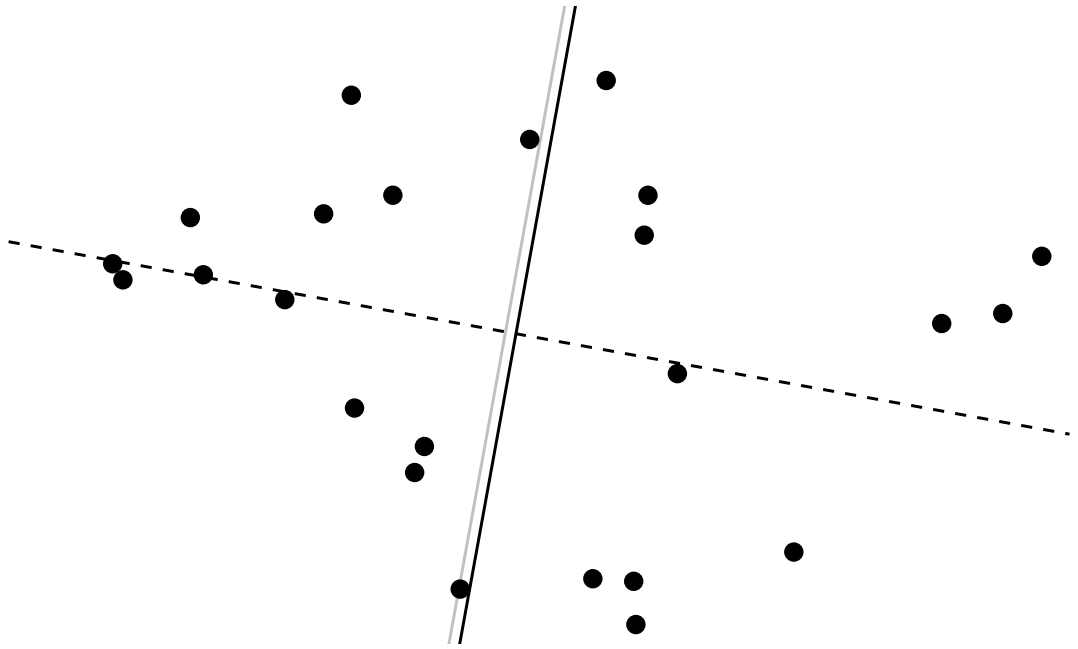

Figure 5.2: Example of an inertial bisection. Vertices are shown as black points, the bisectors of the largest eigen-pair is shown by the black solid, and the bisector of the smallest eigen-pair is shown by the black dashed line. The "shifted" bisector used in the partitioning is shown in grey. While the communication between vertices is not drawn, it is clear that the length (proportional to cut size) of the smallest eigen-pair bisector is larger than that of the largest eigen-pair bisector.

mesh element is the same shape and size. For the application in MPACT, this is always true.

This REB method uses the concept of a *sphere of influence (SOI)* around a vertex. The SOI includes directly neighboring vertices and vertices that neighbor more than one of the direct neighbors or that would if the direct neighbor were present in each structured position around the primary vertex. This is shown for 2-D rectangular structured mesh in Fig. 5.3. For implementation simplicity, the sphere of influence is calculated using distance rather than connectivity.

The starting vertex in this REB method is chosen using a set of prioritized rules:

1. must be on graph boundary, i.e. at least one direct neighbor is not present,
2. must have the lowest summed weight of edges, and
3. must be located furthest from weighted centroid (given by Eq. (5.3)).

Vertices within the expanding subdomain are considered internal vertices, and the remaining vertices are considered to be external vertices. During expansion, the next vertex is determined using a set of prioritized rules:

1. must be neighboring at least one internal vertex,

2. must have the highest summed weight of edges with internal vertices,

3. must have the lowest summed weight of edges with external vertices,

4. must have the largest number of internal SOI vertices,

5. must have the largest number of external SOI vertices, and

6. must have the smallest distance from reference vertex.

The reference vertex is in the expanding subdomain, which begins as the first vertex but changes during expansion; the reference vertex is the most recently added vertex with less external communication than the previously added vertex. An example of the expansion order is shown in Fig. 5.4.

Algorithm 5 The chosen Recursive Expansion Bisection (REB) algorithm.

1: **procedure** REB($G(V, E)$)
2: Compute weighted centroid of the graph
3: Choose a starting vertex for the expanding domain: See rules in **??**
4: Expand the domain from the starting vertex. Let V_s be the list of vertices in order of the expansion: See rules in **??**
5: Cut graph into $G_1(V_1, E_1), G_2(V_2, E_2)$: Algorithm 2
6: REB($G_1(V_1, E_1)$)
7: REB($G_2(V_2, E_2)$)
8: **end procedure**

5.4 Applications for MPACT

Lorem ipsum dolor sit amet, consectetuer adipiscing elit. Etiam lobortis facilisis sem. Nullam nec mi et neque pharetra sollicitudin. Praesent imperdiet mi nec ante. Donec ullamcorper, felis non sodales commodo, lectus velit ultrices augue, a dignissim nibh lectus placerat pede. Vivamus nunc nunc, molestie ut, ultricies vel, semper in, velit. Ut porttitor. Praesent in sapien. Lorem ipsum dolor sit amet, consectetuer adipiscing elit. Duis fringilla tristique neque. Sed interdum libero ut metus. Pellentesque placerat. Nam rutrum augue a leo. Morbi sed elit sit amet ante lobortis sollicitudin. Praesent blandit blandit mauris. Praesent lectus tellus, aliquet aliquam, luctus a, egestas a, turpis. Mauris lacinia lorem sit amet ipsum. Nunc quis urna dictum turpis accumsan semper. Lorem ipsum dolor sit amet, consectetuer adipiscing elit. Etiam lobortis facilisis sem. Nullam nec mi et neque pharetra sollicitudin. Praesent imperdiet mi nec ante. Donec ullamcorper, felis non sodales commodo, lectus velit ultrices augue, a dignissim nibh lectus placerat pede. Vivamus nunc

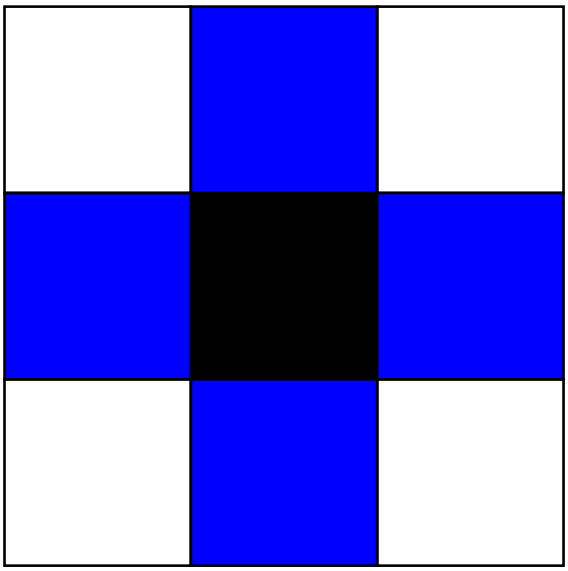

Figure 5.3: “Sphere of influence” example for 2D rectangular structured grid. The primary vertex is shown in black, direct neighbors are blue, and additional vertices in the sphere are white [21].

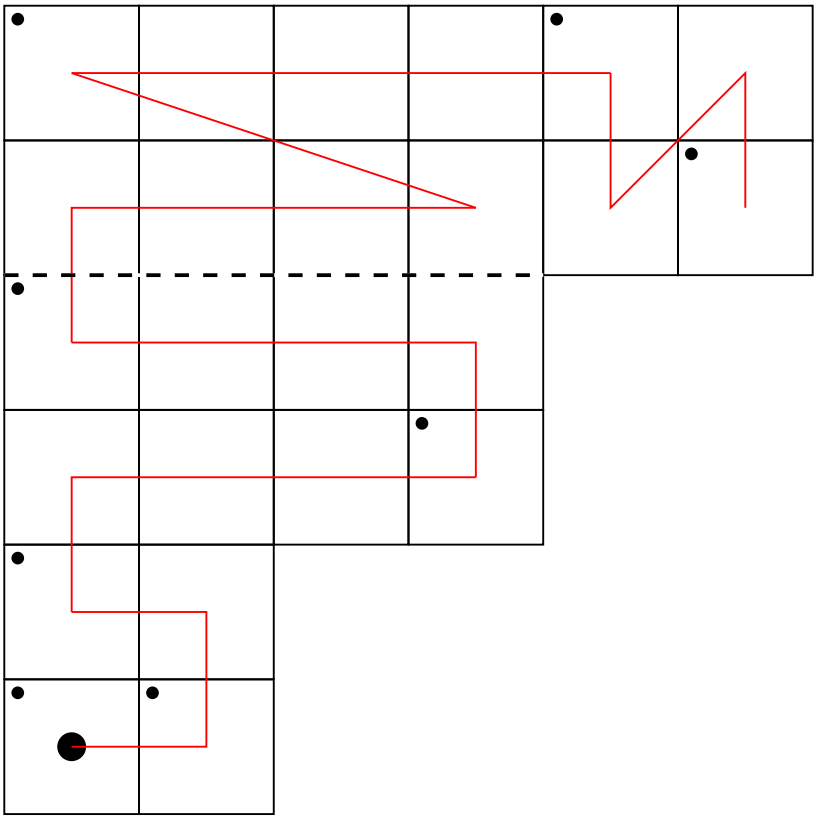

Figure 5.4: An example of the REB method expansion on a small graph. The black lines show the square mesh cells. The expansion begins at the large black point in the center of a cell, and the red line from this shows the expansion’s order. Each small black dot in the upper left of a cell indicates the reference vertices during expansion. The thick black dashed line shows the bisecting cut.

nunc, molestie ut, ultricies vel, semper in, velit. Ut porttitor. Praesent in sapien. Lorem ipsum dolor sit amet, consectetuer adipiscing elit. Duis fringilla tristique neque. Sed interdum libero ut metus. Pellentesque placerat. Nam rutrum augue a leo. Morbi sed elit sit amet ante lobortis sollicitudin. Praesent blandit blandit mauris. Praesent lectus tellus, aliquet aliquam, luctus a, egestas a, turpis. Mauris lacinia lorem sit amet ipsum. Nunc quis urna dictum turpis accumsan semper. Lorem ipsum dolor sit amet, consectetuer adipiscing elit. Etiam lobortis facilisis sem. Nullam nec mi et neque pharetra sollicitudin. Praesent imperdiet mi nec ante. Donec ullamcorper, felis non sodales commodo, lectus velit ultrices augue, a dignissim nibh lectus placerat pede. Vivamus nunc nunc, molestie ut, ultricies vel, semper in, velit. Ut porttitor. Praesent in sapien. Lorem ipsum dolor sit amet, consectetuer adipiscing elit. Duis fringilla tristique neque. Sed interdum libero ut metus. Pellentesque placerat. Nam rutrum augue a leo. Morbi sed elit sit amet ante lobortis sollicitudin. Praesent blandit blandit mauris. Praesent lectus tellus, aliquet aliquam, luctus a, egestas a, turpis. Mauris lacinia lorem sit amet ipsum. Nunc quis urna dictum turpis accumsan semper. Lorem ipsum dolor sit amet, consectetuer adipiscing elit. Etiam lobortis facilisis sem. Nullam nec mi et neque pharetra sollicitudin. Praesent imperdiet mi nec ante. Donec ullamcorper, felis non sodales commodo, lectus velit ultrices augue, a dignissim nibh lectus placerat pede. Vivamus nunc nunc, molestie ut, ultricies vel, semper in, velit. Ut porttitor. Praesent in sapien. Lorem ipsum dolor sit amet, consectetuer adipiscing elit. Duis fringilla tristique neque. Sed interdum libero ut metus. Pellentesque placerat. Nam rutrum augue a leo. Morbi sed elit sit amet ante lobortis sollicitudin. Praesent blandit blandit mauris. Praesent lectus tellus, aliquet aliquam, luctus a, egestas a, turpis. Mauris lacinia lorem sit amet ipsum. Nunc quis urna dictum turpis accumsan semper. Lorem ipsum dolor sit amet, consectetuer adipiscing elit. Etiam lobortis facilisis sem. Nullam nec mi et neque pharetra sollicitudin. Praesent imperdiet mi nec ante. Donec ullamcorper, felis non sodales commodo, lectus velit ultrices augue, a dignissim nibh lectus placerat pede. Vivamus nunc nunc, molestie ut, ultricies vel, semper in, velit. Ut porttitor. Praesent in sapien. Lorem ipsum dolor sit amet, consectetuer adipiscing elit. Duis fringilla tristique neque. Sed interdum libero ut metus. Pellentesque placerat. Nam rutrum augue a leo. Morbi sed elit sit amet ante lobortis sollicitudin. Praesent blandit blandit mauris. Praesent lectus tellus, aliquet aliquam, luctus a, egestas a, turpis. Mauris lacinia lorem sit amet ipsum. Nunc quis urna dictum turpis accumsan semper. Lorem ipsum dolor sit amet, consectetuer adipiscing elit. Etiam lobortis facilisis sem. Nullam nec mi et neque pharetra sollicitudin. Praesent imperdiet mi nec ante. Donec ullamcorper, felis non sodales commodo, lectus velit ultrices augue, a dignissim nibh lectus placerat pede. Vivamus nunc nunc, molestie ut, ultricies vel, semper in, velit. Ut porttitor. Praesent in sapien. Lorem ipsum dolor sit amet, consectetuer adipiscing elit. Duis fringilla tristique neque. Sed interdum libero ut metus. Pellentesque placerat. Nam rutrum augue a leo. Morbi sed elit sit amet ante lobortis sollicitudin. Praesent blandit blandit mauris. Praesent lectus tellus, aliquet aliquam, luctus a, egestas

a, turpis. Mauris lacinia lorem sit amet ipsum. Nunc quis urna dictum turpis accumsan semper. Lorem ipsum dolor sit amet, consectetuer adipiscing elit. Etiam lobortis facilisis sem. Nullam nec mi et neque pharetra sollicitudin. Praesent imperdiet mi nec ante. Donec ullamcorper, felis non sodales commodo, lectus velit ultrices augue, a dignissim nibh lectus placerat pede. Vivamus nunc nunc, molestie ut, ultricies vel, semper in, velit. Ut porttitor. Praesent in sapien. Lorem ipsum dolor sit amet, consectetuer adipiscing elit. Duis fringilla tristique neque. Sed interdum libero ut metus. Pellentesque placerat. Nam rutrum augue a leo. Morbi sed elit sit amet ante lobortis sollicitudin. Praesent blandit blandit mauris. Praesent lectus tellus, aliquet aliquam, luctus a, egestas a, turpis. Mauris lacinia lorem sit amet ipsum. Nunc quis urna dictum turpis accumsan semper. Lorem ipsum dolor sit amet, consectetuer adipiscing elit. Etiam lobortis facilisis sem. Nullam nec mi et neque pharetra sollicitudin. Praesent imperdiet mi nec ante. Donec ullamcorper, felis non sodales commodo, lectus velit ultrices augue, a dignissim nibh lectus placerat pede. Vivamus nunc nunc, molestie ut, ultricies vel, semper in, velit. Ut porttitor. Praesent in sapien. Lorem ipsum dolor sit amet, consectetuer adipiscing elit. Duis fringilla tristique neque. Sed interdum libero ut metus. Pellentesque placerat. Nam rutrum augue a leo. Morbi sed elit sit amet ante lobortis sollicitudin. Praesent blandit blandit mauris. Praesent lectus tellus, aliquet aliquam, luctus a, egestas a, turpis. Mauris lacinia lorem sit amet ipsum. Nunc quis urna dictum turpis accumsan semper.

5.4.1 CMFD Acceleration

Lorem ipsum dolor sit amet, consectetuer adipiscing elit. Etiam lobortis facilisis sem. Nullam nec mi et neque pharetra sollicitudin. Praesent imperdiet mi nec ante. Donec ullamcorper, felis non sodales commodo, lectus velit ultrices augue, a dignissim nibh lectus placerat pede. Vivamus nunc nunc, molestie ut, ultricies vel, semper in, velit. Ut porttitor. Praesent in sapien. Lorem ipsum dolor sit amet, consectetuer adipiscing elit. Duis fringilla tristique neque. Sed interdum libero ut metus. Pellentesque placerat. Nam rutrum augue a leo. Morbi sed elit sit amet ante lobortis sollicitudin. Praesent blandit blandit mauris. Praesent lectus tellus, aliquet aliquam, luctus a, egestas a, turpis. Mauris lacinia lorem sit amet ipsum. Nunc quis urna dictum turpis accumsan semper. Lorem ipsum dolor sit amet, consectetuer adipiscing elit. Etiam lobortis facilisis sem. Nullam nec mi et neque pharetra sollicitudin. Praesent imperdiet mi nec ante. Donec ullamcorper, felis non sodales commodo, lectus velit ultrices augue, a dignissim nibh lectus placerat pede. Vivamus nunc nunc, molestie ut, ultricies vel, semper in, velit. Ut porttitor. Praesent in sapien. Lorem ipsum dolor sit amet, consectetuer adipiscing elit. Duis fringilla tristique neque. Sed interdum libero ut metus. Pellentesque placerat. Nam rutrum augue a leo. Morbi sed elit sit amet ante lobortis sollicitudin. Praesent blandit blandit mauris. Praesent lectus tellus, aliquet aliquam, luctus a, egestas a, turpis. Mauris lacinia lorem sit amet ipsum. Nunc quis urna dictum turpis accumsan semper.

Lorem ipsum dolor sit amet, consectetuer adipiscing elit. Etiam lobortis facilisis sem. Nullam nec mi et neque pharetra sollicitudin. Praesent imperdiet mi nec ante. Donec ullamcorper, felis non sodales commodo, lectus velit ultrices augue, a dignissim nibh lectus placerat pede. Vivamus nunc nunc, molestie ut, ultricies vel, semper in, velit. Ut porttitor. Praesent in sapien. Lorem ipsum dolor sit amet, consectetuer adipiscing elit. Duis fringilla tristique neque. Sed interdum libero ut metus. Pellentesque placerat. Nam rutrum augue a leo. Morbi sed elit sit amet ante lobortis sollicitudin. Praesent blandit blandit mauris. Praesent lectus tellus, aliquet aliquam, luctus a, egestas a, turpis. Mauris lacinia lorem sit amet ipsum. Nunc quis urna dictum turpis accumsan semper.

5.5 Results

5.5.1 2-D Results

Lorem ipsum dolor sit amet, consectetuer adipiscing elit. Etiam lobortis facilisis sem. Nullam nec mi et neque pharetra sollicitudin. Praesent imperdiet mi nec ante. Donec ullamcorper, felis non sodales commodo, lectus velit ultrices augue, a dignissim nibh lectus placerat pede. Vivamus nunc nunc, molestie ut, ultricies vel, semper in, velit. Ut porttitor. Praesent in sapien. Lorem ipsum dolor sit amet, consectetuer adipiscing elit. Duis fringilla tristique neque. Sed interdum libero ut metus. Pellentesque placerat. Nam rutrum augue a leo. Morbi sed elit sit amet ante lobortis sollicitudin. Praesent blandit blandit mauris. Praesent lectus tellus, aliquet aliquam, luctus a, egestas a, turpis. Mauris lacinia lorem sit amet ipsum. Nunc quis urna dictum turpis accumsan semper. Lorem ipsum dolor sit amet, consectetuer adipiscing elit. Etiam lobortis facilisis sem. Nullam nec mi et neque pharetra sollicitudin. Praesent imperdiet mi nec ante. Donec ullamcorper, felis non sodales commodo, lectus velit ultrices augue, a dignissim nibh lectus placerat pede. Vivamus nunc nunc, molestie ut, ultricies vel, semper in, velit. Ut porttitor. Praesent in sapien. Lorem ipsum dolor sit amet, consectetuer adipiscing elit. Duis fringilla tristique neque. Sed interdum libero ut metus. Pellentesque placerat. Nam rutrum augue a leo. Morbi sed elit sit amet ante lobortis sollicitudin. Praesent blandit blandit mauris. Praesent lectus tellus, aliquet aliquam, luctus a, egestas a, turpis. Mauris lacinia lorem sit amet ipsum. Nunc quis urna dictum turpis accumsan semper. Lorem ipsum dolor sit amet, consectetuer adipiscing elit. Etiam lobortis facilisis sem. Nullam nec mi et neque pharetra sollicitudin. Praesent imperdiet mi nec ante. Donec ullamcorper, felis non sodales commodo, lectus velit ultrices augue, a dignissim nibh lectus placerat pede. Vivamus nunc nunc, molestie ut, ultricies vel, semper in, velit. Ut porttitor. Praesent in sapien. Lorem ipsum dolor sit amet, consectetuer adipiscing elit. Duis fringilla tristique neque. Sed interdum libero ut metus. Pellentesque placerat. Nam rutrum augue a leo. Morbi sed elit sit amet ante lobortis sollicitudin. Praesent blandit blandit mauris. Praesent lectus tellus, aliquet aliquam, luctus a, egestas

a, turpis. Mauris lacinia lorem sit amet ipsum. Nunc quis urna dictum turpis accumsan semper. Lorem ipsum dolor sit amet, consectetuer adipiscing elit. Etiam lobortis facilisis sem. Nullam nec mi et neque pharetra sollicitudin. Praesent imperdiet mi nec ante. Donec ullamcorper, felis non sodales commodo, lectus velit ultrices augue, a dignissim nibh lectus placerat pede. Vivamus nunc nunc, molestie ut, ultricies vel, semper in, velit. Ut porttitor. Praesent in sapien. Lorem ipsum dolor sit amet, consectetuer adipiscing elit. Duis fringilla tristique neque. Sed interdum libero ut metus. Pellentesque placerat. Nam rutrum augue a leo. Morbi sed elit sit amet ante lobortis sollicitudin. Praesent blandit blandit mauris. Praesent lectus tellus, aliquet aliquam, luctus a, egestas a, turpis. Mauris lacinia lorem sit amet ipsum. Nunc quis urna dictum turpis accumsan semper. Lorem ipsum dolor sit amet, consectetuer adipiscing elit. Etiam lobortis facilisis sem. Nullam nec mi et neque pharetra sollicitudin. Praesent imperdiet mi nec ante. Donec ullamcorper, felis non sodales commodo, lectus velit ultrices augue, a dignissim nibh lectus placerat pede. Vivamus nunc nunc, molestie ut, ultricies vel, semper in, velit. Ut porttitor. Praesent in sapien. Lorem ipsum dolor sit amet, consectetuer adipiscing elit. Duis fringilla tristique neque. Sed interdum libero ut metus. Pellentesque placerat. Nam rutrum augue a leo. Morbi sed elit sit amet ante lobortis sollicitudin. Praesent blandit blandit mauris. Praesent lectus tellus, aliquet aliquam, luctus a, egestas a, turpis. Mauris lacinia lorem sit amet ipsum. Nunc quis urna dictum turpis accumsan semper. Lorem ipsum dolor sit amet, consectetuer adipiscing elit. Etiam lobortis facilisis sem. Nullam nec mi et neque pharetra sollicitudin. Praesent imperdiet mi nec ante. Donec ullamcorper, felis non sodales commodo, lectus velit ultrices augue, a dignissim nibh lectus placerat pede. Vivamus nunc nunc, molestie ut, ultricies vel, semper in, velit. Ut porttitor. Praesent in sapien. Lorem ipsum dolor sit amet, consectetuer adipiscing elit. Duis fringilla tristique neque. Sed interdum libero ut metus. Pellentesque placerat. Nam rutrum augue a leo. Morbi sed elit sit amet ante lobortis sollicitudin. Praesent blandit blandit mauris. Praesent lectus tellus, aliquet aliquam, luctus a, egestas a, turpis. Mauris lacinia lorem sit amet ipsum. Nunc quis urna dictum turpis accumsan semper. Lorem ipsum dolor sit amet, consectetuer adipiscing elit. Etiam lobortis facilisis sem. Nullam nec mi et neque pharetra sollicitudin. Praesent imperdiet mi nec ante. Donec ullamcorper, felis non sodales commodo, lectus velit ultrices augue, a dignissim nibh lectus placerat pede. Vivamus nunc nunc, molestie ut, ultricies vel, semper in, velit. Ut porttitor. Praesent in sapien. Lorem ipsum dolor sit amet, consectetuer adipiscing elit. Duis fringilla tristique neque. Sed interdum libero ut metus. Pellentesque placerat. Nam rutrum augue a leo. Morbi sed elit sit amet ante lobortis sollicitudin. Praesent blandit blandit mauris. Praesent lectus tellus, aliquet aliquam, luctus a, egestas a, turpis. Mauris lacinia lorem sit amet ipsum. Nunc quis urna dictum turpis accumsan semper. Lorem ipsum dolor sit amet, consectetuer adipiscing elit. Etiam lobortis facilisis sem. Nullam nec mi et neque pharetra sollicitudin. Praesent imperdiet mi nec ante. Donec ullamcorper, felis non sodales commodo, lectus velit ultrices augue, a dignissim nibh lectus placerat pede. Vivamus nunc

nunc, molestie ut, ultricies vel, semper in, velit. Ut porttitor. Praesent in sapien. Lorem ipsum dolor sit amet, consectetuer adipiscing elit. Duis fringilla tristique neque. Sed interdum libero ut metus. Pellentesque placerat. Nam rutrum augue a leo. Morbi sed elit sit amet ante lobortis sollicitudin. Praesent blandit blandit mauris. Praesent lectus tellus, aliquet aliquam, luctus a, egestas a, turpis. Mauris lacinia lorem sit amet ipsum. Nunc quis urna dictum turpis accumsan semper.

5.5.2 3-D Results

Lorem ipsum dolor sit amet, consectetuer adipiscing elit. Etiam lobortis facilisis sem. Nullam nec mi et neque pharetra sollicitudin. Praesent imperdiet mi nec ante. Donec ullamcorper, felis non sodales commodo, lectus velit ultrices augue, a dignissim nibh lectus placerat pede. Vivamus nunc nunc, molestie ut, ultricies vel, semper in, velit. Ut porttitor. Praesent in sapien. Lorem ipsum dolor sit amet, consectetuer adipiscing elit. Duis fringilla tristique neque. Sed interdum libero ut metus. Pellentesque placerat. Nam rutrum augue a leo. Morbi sed elit sit amet ante lobortis sollicitudin. Praesent blandit blandit mauris. Praesent lectus tellus, aliquet aliquam, luctus a, egestas a, turpis. Mauris lacinia lorem sit amet ipsum. Nunc quis urna dictum turpis accumsan semper. Lorem ipsum dolor sit amet, consectetuer adipiscing elit. Etiam lobortis facilisis sem. Nullam nec mi et neque pharetra sollicitudin. Praesent imperdiet mi nec ante. Donec ullamcorper, felis non sodales commodo, lectus velit ultrices augue, a dignissim nibh lectus placerat pede. Vivamus nunc nunc, molestie ut, ultricies vel, semper in, velit. Ut porttitor. Praesent in sapien. Lorem ipsum dolor sit amet, consectetuer adipiscing elit. Duis fringilla tristique neque. Sed interdum libero ut metus. Pellentesque placerat. Nam rutrum augue a leo. Morbi sed elit sit amet ante lobortis sollicitudin. Praesent blandit blandit mauris. Praesent lectus tellus, aliquet aliquam, luctus a, egestas a, turpis. Mauris lacinia lorem sit amet ipsum. Nunc quis urna dictum turpis accumsan semper. Lorem ipsum dolor sit amet, consectetuer adipiscing elit. Etiam lobortis facilisis sem. Nullam nec mi et neque pharetra sollicitudin. Praesent imperdiet mi nec ante. Donec ullamcorper, felis non sodales commodo, lectus velit ultrices augue, a dignissim nibh lectus placerat pede. Vivamus nunc nunc, molestie ut, ultricies vel, semper in, velit. Ut porttitor. Praesent in sapien. Lorem ipsum dolor sit amet, consectetuer adipiscing elit. Duis fringilla tristique neque. Sed interdum libero ut metus. Pellentesque placerat. Nam rutrum augue a leo. Morbi sed elit sit amet ante lobortis sollicitudin. Praesent blandit blandit mauris. Praesent lectus tellus, aliquet aliquam, luctus a, egestas a, turpis. Mauris lacinia lorem sit amet ipsum. Nunc quis urna dictum turpis accumsan semper. Lorem ipsum dolor sit amet, consectetuer adipiscing elit. Etiam lobortis facilisis sem. Nullam nec mi et neque pharetra sollicitudin. Praesent imperdiet mi nec ante. Donec ullamcorper, felis non sodales commodo, lectus velit ultrices augue, a dignissim nibh lectus placerat pede. Vivamus nunc nunc, molestie ut, ultricies vel, semper in, velit. Ut porttitor. Praesent in sapien. Lorem ipsum dolor

sit amet, consectetuer adipiscing elit. Duis fringilla tristique neque. Sed interdum libero ut metus. Pellentesque placerat. Nam rutrum augue a leo. Morbi sed elit sit amet ante lobortis sollicitudin. Praesent blandit blandit mauris. Praesent lectus tellus, aliquet aliquam, luctus a, egestas a, turpis. Mauris lacinia lorem sit amet ipsum. Nunc quis urna dictum turpis accumsan semper.

5.6 Partition Refinement

Lorem ipsum dolor sit amet, consectetuer adipiscing elit. Etiam lobortis facilisis sem. Nullam nec mi et neque pharetra sollicitudin. Praesent imperdiet mi nec ante. Donec ullamcorper, felis non sodales commodo, lectus velit ultrices augue, a dignissim nibh lectus placerat pede. Vivamus nunc nunc, molestie ut, ultricies vel, semper in, velit. Ut porttitor. Praesent in sapien. Lorem ipsum dolor sit amet, consectetuer adipiscing elit. Duis fringilla tristique neque. Sed interdum libero ut metus. Pellentesque placerat. Nam rutrum augue a leo. Morbi sed elit sit amet ante lobortis sollicitudin. Praesent blandit blandit mauris. Praesent lectus tellus, aliquet aliquam, luctus a, egestas a, turpis. Mauris lacinia lorem sit amet ipsum. Nunc quis urna dictum turpis accumsan semper. Lorem ipsum dolor sit amet, consectetuer adipiscing elit. Etiam lobortis facilisis sem. Nullam nec mi et neque pharetra sollicitudin. Praesent imperdiet mi nec ante. Donec ullamcorper, felis non sodales commodo, lectus velit ultrices augue, a dignissim nibh lectus placerat pede. Vivamus nunc nunc, molestie ut, ultricies vel, semper in, velit. Ut porttitor. Praesent in sapien. Lorem ipsum dolor sit amet, consectetuer adipiscing elit. Duis fringilla tristique neque. Sed interdum libero ut metus. Pellentesque placerat. Nam rutrum augue a leo. Morbi sed elit sit amet ante lobortis sollicitudin. Praesent blandit blandit mauris. Praesent lectus tellus, aliquet aliquam, luctus a, egestas a, turpis. Mauris lacinia lorem sit amet ipsum. Nunc quis urna dictum turpis accumsan semper. Lorem ipsum dolor sit amet, consectetuer adipiscing elit. Etiam lobortis facilisis sem. Nullam nec mi et neque pharetra sollicitudin. Praesent imperdiet mi nec ante. Donec ullamcorper, felis non sodales commodo, lectus velit ultrices augue, a dignissim nibh lectus placerat pede. Vivamus nunc nunc, molestie ut, ultricies vel, semper in, velit. Ut porttitor. Praesent in sapien. Lorem ipsum dolor sit amet, consectetuer adipiscing elit. Duis fringilla tristique neque. Sed interdum libero ut metus. Pellentesque placerat. Nam rutrum augue a leo. Morbi sed elit sit amet ante lobortis sollicitudin. Praesent blandit blandit mauris. Praesent lectus tellus, aliquet aliquam, luctus a, egestas a, turpis. Mauris lacinia lorem sit amet ipsum. Nunc quis urna dictum turpis accumsan semper. Lorem ipsum dolor sit amet, consectetuer adipiscing elit. Etiam lobortis facilisis sem. Nullam nec mi et neque pharetra sollicitudin. Praesent imperdiet mi nec ante. Donec ullamcorper, felis non sodales commodo, lectus velit ultrices augue, a dignissim nibh lectus placerat pede. Vivamus nunc nunc, molestie ut, ultricies vel, semper in, velit. Ut porttitor. Praesent in sapien. Lorem ipsum dolor sit amet, consectetuer adipiscing elit. Duis fringilla tristique neque. Sed interdum libero

ut metus. Pellentesque placerat. Nam rutrum augue a leo. Morbi sed elit sit amet ante lobortis sollicitudin. Praesent blandit blandit mauris. Praesent lectus tellus, aliquet aliquam, luctus a, egestas a, turpis. Mauris lacinia lorem sit amet ipsum. Nunc quis urna dictum turpis accumsan semper. Lorem ipsum dolor sit amet, consectetuer adipiscing elit. Etiam lobortis facilisis sem. Nullam nec mi et neque pharetra sollicitudin. Praesent imperdiet mi nec ante. Donec ullamcorper, felis non sodales commodo, lectus velit ultrices augue, a dignissim nibh lectus placerat pede. Vivamus nunc nunc, molestie ut, ultricies vel, semper in, velit. Ut porttitor. Praesent in sapien. Lorem ipsum dolor sit amet, consectetuer adipiscing elit. Duis fringilla tristique neque. Sed interdum libero ut metus. Pellentesque placerat. Nam rutrum augue a leo. Morbi sed elit sit amet ante lobortis sollicitudin. Praesent blandit blandit mauris. Praesent lectus tellus, aliquet aliquam, luctus a, egestas a, turpis. Mauris lacinia lorem sit amet ipsum. Nunc quis urna dictum turpis accumsan semper. Lorem ipsum dolor sit amet, consectetuer adipiscing elit. Etiam lobortis facilisis sem. Nullam nec mi et neque pharetra sollicitudin. Praesent imperdiet mi nec ante. Donec ullamcorper, felis non sodales commodo, lectus velit ultrices augue, a dignissim nibh lectus placerat pede. Vivamus nunc nunc, molestie ut, ultricies vel, semper in, velit. Ut porttitor. Praesent in sapien. Lorem ipsum dolor sit amet, consectetuer adipiscing elit. Duis fringilla tristique neque. Sed interdum libero ut metus. Pellentesque placerat. Nam rutrum augue a leo. Morbi sed elit sit amet ante lobortis sollicitudin. Praesent blandit blandit mauris. Praesent lectus tellus, aliquet aliquam, luctus a, egestas a, turpis. Mauris lacinia lorem sit amet ipsum. Nunc quis urna dictum turpis accumsan semper. Lorem ipsum dolor sit amet, consectetuer adipiscing elit. Etiam lobortis facilisis sem. Nullam nec mi et neque pharetra sollicitudin. Praesent imperdiet mi nec ante. Donec ullamcorper, felis non sodales commodo, lectus velit ultrices augue, a dignissim nibh lectus placerat pede. Vivamus nunc nunc, molestie ut, ultricies vel, semper in, velit. Ut porttitor. Praesent in sapien. Lorem ipsum dolor sit amet, consectetuer adipiscing elit. Duis fringilla tristique neque. Sed interdum libero ut metus. Pellentesque placerat. Nam rutrum augue a leo. Morbi sed elit sit amet ante lobortis sollicitudin. Praesent blandit blandit mauris. Praesent lectus tellus, aliquet aliquam, luctus a, egestas a, turpis. Mauris lacinia lorem sit amet ipsum. Nunc quis urna dictum turpis accumsan semper. Lorem ipsum dolor sit amet, consectetuer adipiscing elit. Etiam lobortis facilisis sem. Nullam nec mi et neque pharetra sollicitudin. Praesent imperdiet mi nec ante. Donec ullamcorper, felis non sodales commodo, lectus velit ultrices augue, a dignissim nibh lectus placerat pede. Vivamus nunc nunc, molestie ut, ultricies vel, semper in, velit. Ut porttitor. Praesent in sapien. Lorem ipsum dolor sit amet, consectetuer adipiscing elit. Duis fringilla tristique neque. Sed interdum libero ut metus. Pellentesque placerat. Nam rutrum augue a leo. Morbi sed elit sit amet ante lobortis sollicitudin. Praesent blandit blandit mauris. Praesent lectus tellus, aliquet aliquam, luctus a, egestas a, turpis. Mauris lacinia lorem sit amet ipsum. Nunc quis urna dictum turpis accumsan semper.

5.7 Conclusions

Lorem ipsum dolor sit amet, consectetuer adipiscing elit. Etiam lobortis facilisis sem. Nullam nec mi et neque pharetra sollicitudin. Praesent imperdiet mi nec ante. Donec ullamcorper, felis non sodales commodo, lectus velit ultrices augue, a dignissim nibh lectus placerat pede. Vivamus nunc nunc, molestie ut, ultricies vel, semper in, velit. Ut porttitor. Praesent in sapien. Lorem ipsum dolor sit amet, consectetuer adipiscing elit. Duis fringilla tristique neque. Sed interdum libero ut metus. Pellentesque placerat. Nam rutrum augue a leo. Morbi sed elit sit amet ante lobortis sollicitudin. Praesent blandit blandit mauris. Praesent lectus tellus, aliquet aliquam, luctus a, egestas a, turpis. Mauris lacinia lorem sit amet ipsum. Nunc quis urna dictum turpis accumsan semper. Lorem ipsum dolor sit amet, consectetuer adipiscing elit. Etiam lobortis facilisis sem. Nullam nec mi et neque pharetra sollicitudin. Praesent imperdiet mi nec ante. Donec ullamcorper, felis non sodales commodo, lectus velit ultrices augue, a dignissim nibh lectus placerat pede. Vivamus nunc nunc, molestie ut, ultricies vel, semper in, velit. Ut porttitor. Praesent in sapien. Lorem ipsum dolor sit amet, consectetuer adipiscing elit. Duis fringilla tristique neque. Sed interdum libero ut metus. Pellentesque placerat. Nam rutrum augue a leo. Morbi sed elit sit amet ante lobortis sollicitudin. Praesent blandit blandit mauris. Praesent lectus tellus, aliquet aliquam, luctus a, egestas a, turpis. Mauris lacinia lorem sit amet ipsum. Nunc quis urna dictum turpis accumsan semper. Lorem ipsum dolor sit amet, consectetuer adipiscing elit. Etiam lobortis facilisis sem. Nullam nec mi et neque pharetra sollicitudin. Praesent imperdiet mi nec ante. Donec ullamcorper, felis non sodales commodo, lectus velit ultrices augue, a dignissim nibh lectus placerat pede. Vivamus nunc nunc, molestie ut, ultricies vel, semper in, velit. Ut porttitor. Praesent in sapien. Lorem ipsum dolor sit amet, consectetuer adipiscing elit. Duis fringilla tristique neque. Sed interdum libero ut metus. Pellentesque placerat. Nam rutrum augue a leo. Morbi sed elit sit amet ante lobortis sollicitudin. Praesent blandit blandit mauris. Praesent lectus tellus, aliquet aliquam, luctus a, egestas a, turpis. Mauris lacinia lorem sit amet ipsum. Nunc quis urna dictum turpis accumsan semper. Lorem ipsum dolor sit amet, consectetuer adipiscing elit. Etiam lobortis facilisis sem. Nullam nec mi et neque pharetra sollicitudin. Praesent imperdiet mi nec ante. Donec ullamcorper, felis non sodales commodo, lectus velit ultrices augue, a dignissim nibh lectus placerat pede. Vivamus nunc nunc, molestie ut, ultricies vel, semper in, velit. Ut porttitor. Praesent in sapien. Lorem ipsum dolor sit amet, consectetuer adipiscing elit. Duis fringilla tristique neque. Sed interdum libero ut metus. Pellentesque placerat. Nam rutrum augue a leo. Morbi sed elit sit amet ante lobortis sollicitudin. Praesent blandit blandit mauris. Praesent lectus tellus, aliquet aliquam, luctus a, egestas a, turpis. Mauris lacinia lorem sit amet ipsum. Nunc quis urna dictum turpis accumsan semper.

CHAPTER 6

Initial Results

6.1 2-D Linear Source

The LSMoC method has been a significant part of this thesis work. The method, as described by Ferrer and Rhodes [14], was implemented in MPACT [8], and has been significantly improved for cases with near-void regions [16], and multiphysics calculations [17]. So far, detailed analysis has only been done for 2-D calculations; in this section, the results from a conference paper on the improved formulation are presented. Work done by others has indicated that for single physics (neutronics) calculations, significantly coarser meshes can be used with the LSA as compared to the FSA [7, 9, 14], resulting in faster computations; the goal of this conference paper was to present a reformulation of the method, that is more efficient in multi-physics calculations, as well as present results to indicate that coarser meshes could still be used [17]. At the current time, all results are presented using TCP0 cross sections and odCMFD acceleration [35].

In this work, two additional physics are considered: isotopic depletion, and T/H feedback. Typical LWRs use UO_2 fuel; however, a significant fraction of power comes from plutonium fission events. As a fuel rod is depleted during reactor operation, plutonium builds up in the outer rim of the fuel rods. In calculations with isotopic depletion, it is necessary to accurately capture this radial distribution of plutonium. In MPACT-CTF coupling, fuel temperatures are averaged radially. Since there is no radial dependence, it is not necessary to consider additional radial meshing to account for this physics. However, there is current work to add radially dependence to T/H feedback quantities in the coupling between MPACT and CTF, and this is common in other high fidelity neutronics codes. This may affect the number of rings needed in fuel meshes, for both the FSMoC and LSMoC solvers.

To help determine optimal default meshing parameters for the LSMoC solver in MPACT, a parametric study was done on a pin cell with isotopic depletion up to 70 MWD/kgHM. Using the default FSMoC mesh as a starting point, the meshing parameters were coarsened; for each parameter, the coarsest option, that did not cause significant change in the eigenvalue over the

depletion, was selected. The resulting coarse mesh has two fuel rings (inner radius at 87.5% of outer), a single ring in the cladding, a single ring in the gap, and four azimuthal divisions in all regions. However, in the lattice and assembly test cases, a single azimuthal region was found to be sufficient in the fuel, clad, and gap material regions when using the LSMoC solver. The inner fuel radius at 87.5% of the outer radius is consistent with measured radial distributions of plutonium in irradiated UO_2 fuel rods [83]. This mesh, along with the default FSMoC mesh, is shown in Fig. 6.1.

Results from three cases are presented in the following subsections: 2D zero-power lattice cases, 2D lattice depletion cases, and a 3D fuel assembly with T/H feedback.

6.1.1 Pin Cell Isotopic Depletion

As reactors operate, interactions of the fuel with neutrons causes isotopic changes within the fuel, over long periods this can lead to significant changes in the fuel composition. Changes in the fuel composition play an important role in the power distribution as a reactor operates, and is thus a key additional physics to consider in reactor simulations. A parametric mesh-refinement study are presented for a single UO_2 pin cell depletion up to 70 MWD/kgHM.

During depletion, it is important to accurately capture the radial distribution of Plutonium due to self-shielding effects. However, Plutonium is primarily concentrated in the outer rim of the pin, this is the well known rim-effect. The expectation is that a single additional fuel ring can be used to capture this rim effect. This was found to be the case, with an inner ring with radius fraction 0.875 that of the outer fuel radius [17]. This seems to be consistent with measured radial Plutonium distributions [83].

6.1.2 2-D Zero-Power Lattice Cases

Initial tests were run on a series of zero-power 2-D lattices: the Virtual Environment for Reactor Analysis (VERA) problem 2 cases [84]. By doing so, it can be verified that the LSMoC solvers are as accurate on this coarse mesh as the FSMoC solver on the current default mesh parameters in MPACT. These cases cover a variety of lattice configurations as different temperatures, with and without burnable absorbers or other inserts. Each case is described in detail in the reference [84].

Each lattice case was run with default and coarse meshes with the FSMoC and LSMoC solvers. Each of these cases used a Tabuchi-Yamamoto angular quadrature set [25] with 64 azimuthal angles, 4 polar angles over 4π, and 0.05 cm ray-spacing. However, due to thin regions from IFBA and WABA rods in cases L, M, and N, a ray-spacing of 0.01 cm was used. The results are compared against a very finely meshed case run using the LSMoC solver with 128 azimuthal angles, 4 polar angles, and 0.01 cm ray-spacing. Results are summarized in Table 6.1.

On average, the LSMoC solver on the coarse mesh is more accurate than the FSMoC solver on the current default mesh. Additionally, the largest differences for both eigenvalue and RMS pin power differences are smaller than those for the FSMoC solver. This indicates that, for these cases, the LSMoC solver on the coarse mesh is sufficiently accurate. On average, the LSMoC solver on the coarse mesh took 12% less time per iteration, and used approximately 12% less memory.

Table 6.1: Results for 2D zero-power lattice cases in terms of eigenvalue difference and RMS pin power difference from the very finely meshed LSMoC solution.

Case	Δk_{eff} (pcm)			RMS Pin Power Difference (%)		
	FS default	FS coarse	LS coarse	FS default	FS coarse	LS coarse
A	-17.37	43.98	-36.00	0.04	0.12	0.02
B	-14.88	46.21	-33.83	0.04	0.12	0.02
C	-17.37	43.98	-36.00	0.04	0.12	0.02
D	-25.47	38.95	-40.97	0.04	0.12	0.02
E	-49.02	-51.80	-26.93	0.06	0.18	0.02
F	-74.17	-119.73	-25.68	0.05	0.18	0.02
G	-98.35	-210.38	-42.52	0.08	0.26	0.04
H	-77.90	-206.12	18.40	0.11	0.32	0.07
I	2.36	82.42	-23.56	0.04	0.14	0.03
J	-74.18	-119.45	-25.86	0.05	0.17	0.02
K	-61.48	-97.41	-18.86	0.05	0.19	0.03
L	60.38	104.64	52.02	0.06	0.17	0.05
M	74.48	123.69	71.36	0.05	0.12	0.05
N	-0.96	-44.92	42.85	0.11	0.32	0.04
O	-21.26	-109.47	7.11	0.06	0.20	0.03
P	-115.03	-311.33	-64.06	0.09	0.28	0.05
Q	-12.26	53.68	-30.41	0.04	0.13	0.03
Avg.	46.88	106.36	35.08	0.06	0.18	0.03
Max.	115.03	311.33	71.36	0.11	0.32	0.07

6.1.3 2-D Lattice Depletion

In Section 6.1.2, the LSMoC on the coarse mesh was shown to be sufficiently accurate for an array of lattice problems at zero-power. Two of these problems, 2a and 2p, were selected for further study by performing isotopic depletion up to 70 MWD/kgHM at HFP conditions. Problem 2A represents a typical lattice configuration consisting only of fuel rods and empty guide-tubes. Problem 2P contains several gadolinia rods that act as burnable absorbers; reactivity is significantly damped at beginning of cycle, but increases as gadolinia is burned. The gadolinia rods require significant radial meshing to accurately capture the complicated distribution throughout the depletion (it is

an effectively a *moving boundary layer*); the default meshing for the FSMoC solver has 10 equal volume rings in the fuel. Due to this complicated distribution, the LSMoC solver can only eliminate two of the additional radial rings while maintaining the same level of accuracy as the FSMoC solver on the current default mesh. However, similar azimuthal coarsening is possible on these rods, with a single azimuthal region in all but the surrounding moderator, which has 4 azimuthal regions. Overall, a significant reduction in the lattice mesh is still possible, as shown in Fig. 6.1.

As shown in Fig. 6.2, the LSMoC solver on a coarse mesh has similar accuracy as the FSMoC solver on the current default mesh. However, the coarse mesh LSMoC calculation took took 23% and 18% less time for cases A and P, respectively, than the corresponding default mesh FSMoC calculations. Although the LSMoC method was intended, primarily, to increase efficiency in the MoC calculation, much of the time saved is actually from reduced time in the isotopic depletion routines. 21% and 18% less memory was used by MPACT in cases A and P, respectively.

(a) Default fuel rod mesh (56 cells)

(b) Coarse fuel rod mesh (20 cells)

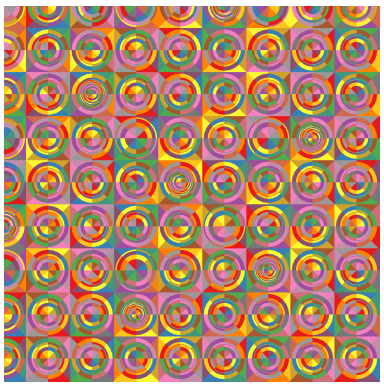

(c) Default lattice (2p) mesh (4282 cells)

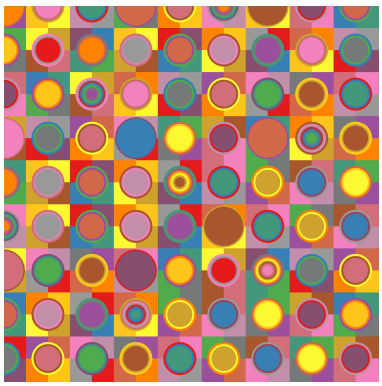

(d) Coarse lattice (2p) mesh (637 cells)

Figure 6.1: Current default and coarse meshes for pin and lattice (2P) calculations.

6.1.4 3-D Assembly with T/H Feedback

The final case examined in this work was a single 3D assembly with T/H feedback: VERA problem 6 [84]. This case demonstrates that a coarser mesh can be used with the LSMoC solver in problems with T/H feedback and in the 2D/1D framework [8]. Meshing parameters from the previous results were used in fuel and guide-tube elements. The lower and upper plates and nozzles are meshed as rectilinear grids in MPACT; these were able to be coarsened to 0.42×0.42 cm^2 sized elements.

This case was run with the default and coarse meshes with the FSMoC and LSMoC solvers. Each calculation was compared against a finely meshed case run with the LSMoC solver. The same angular quadratures were used in these assembly cases as the lattice cases, but a ray-spacing of 0.03 cm was used for the cases on the default and coarse meshes. Results are summarized in Table 6.2.

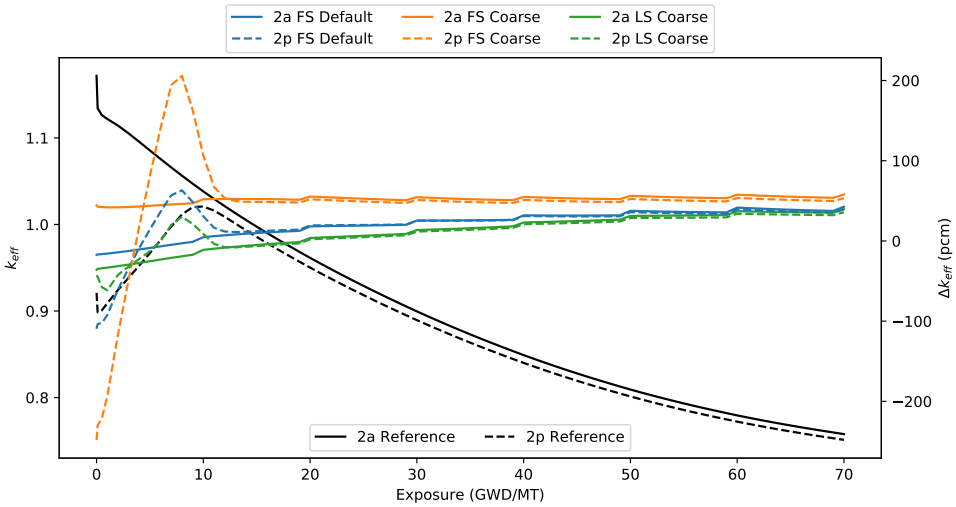

Figure 6.2: Eigenvalue reference values and differences for default, and coarse mesh calculations throughout isotopic depletion of VERA problems 2A and 2P up to 70 MWD/kgHM.

Table 6.2 shows that the LSMoC solver on the coarse mesh is at least as accurate as the FSMoC solver on the current default mesh. Although the LSMoC has lower total run-times, by about 6.5%, these times cannot be directly compared due to the difference in number of outer iterations. This difference in iterations is likely caused by false convergence due to the oscillatory convergence observed in problems with T/H feedback and CMFD acceleration [36]. Scaling times by the number of outer iterations is also not a fair comparison because CMFD acceleration and CTF take significantly longer during the first several iterations. A fairer comparison is to instead compare the time of the default FSMoC solver at 9 outer iterations to the LSMoC solver: 392.99 seconds. This still indicates that the LSMoC solver decreases run-times by about 4%, and reduces memory usage by 21%. This increased efficiency is significantly lower than in the previous results, though this is not surprising, as MoC accounts for less than 5% of the total run-time in this case.

Table 6.2: Eigenvalue and pin power comparison results for VERA problem 6.

	FS Default	FS Coarse	LS Coarse
Δk_{eff} (pcm)	33.54	108.74	13.22
RMS Pin Power Diff. (%)	0.19	0.45	0.03
Max Pin Power Diff. (%)	0.43	0.91	0.10
Time (s)	403.7	388.1	376.2
Outer Iterations	11	11	9
Memory (MB)	8398.4	6507.6	6583.0

6.1.5 Summary

Results have indicated that in multiphysics calculations (isotopic depletion and T/H feedback) LSMoC solvers still allow for significant reduction in the computational mesh. In cases with isotopic depletion, the reformulated LSMoC [17] leads to significant runtime and memory advantages of FSMoC solvers. However, in cases with T/H feedback, runtime is dominated by the T/H feedback solve; use of the LSMoC leads to significant reduction in memory, but not runtime.

Previous studies have indicated that the LSMoC solvers allow for coarser meshes in 3-D single-physics (neutronics) calculations, leading to significant runtime advantages over the FSA [7, 9]. The initial results of this work have indicated that the reformulated method allows for coarser meshes in multiphysics calculations in 2-D; this leads to the expectation that the reformulated LSMoC will lead to runtime and memory advantages in 3-D multiphysics calculations. This remains as future work to be included as part of this thesis.

Additionally, these initial results only present results for isotropic scattering cases, and should be generalized to include anisotropic sources. 2-D and 3-D core-depletion calculations should also be performed to verify the mesh parameters found from this work.

6.2 2-D Macroband

Part of this thesis work is the extension of the macroband (Section 4.3) ray-tracing method to three-dimensional transport problems. While 2-D macroband has been implemented and tested in previous studies [19, 20, 48, 62], to the best of the author's knowledge, no study has been performed for 3-D calculations. In 2-D, the macroband method allows for coarser ray-spacing with maintained accuracy leading to more efficient MoC calculations; the expectation is that by extending this method to 3-D, ray-spacing can be reduced in both radial and axial directions, leading to a more significant increase in efficiency.

As part of this thesis work, development of a macroray (Section 4.4.4) MoC transport solver library is being implemented in MPACT. As GPUs have become more prevalent in parallelizable scientific computation, this MoC library is being implemented with the Kokkos library [85]; the Kokkos library allows for performant-portable code to run efficiently on both CPU and GPU. This has been the focus of recent work, and the MoC library is still in early stages. The current form of the library uses the angle-dependent sub-boundary averaging technique for approximating angular flux on subsystem boundaries, as described by Liu et al. [29]. Some initial results have been generated for a 2-D pin-cell, in order to help verify previous results on the macroband method.

Initial tests have been performed on a single 2-D UO_2 pin-cell from the c5g7 benchmark. Calculations were run using a range of ray-spacings, on a coarse mesh, with the linear source solver.

Each calculation was run with the MRT, Macroband with uniform spacing, and Macroband with Gauss-Legendre spacing. Initial results are shown in Figs. 6.3 to 6.5.

One interesting thing to note, is that the MRT ray-tracing methods converge to a different result as the ray-spacing is refined. This is likely due to the perturbation of the azimuthal quadrature caused by the DNPL requirement of MRT. It is also interesting to note, that the macroband method with Gauss-Legendre spacing seems to have better accuracy than the MRT method; though in this case error is small, it will be useful to see results for a more realistic (51-group) pin-cell calculation. However, as previous studies have indicated [19], the macroband method with uniform ray-spacing within each band seems to perform worse than the traditional ray-tracing techniques.

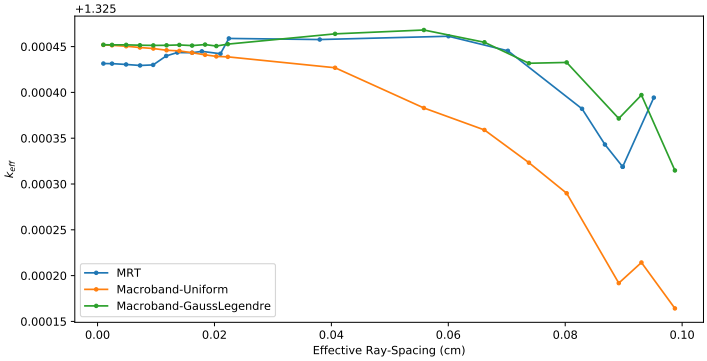

Figure 6.3: Eigenvalue comparisons for the different ray-tracing methods over a range of ray-spacings.

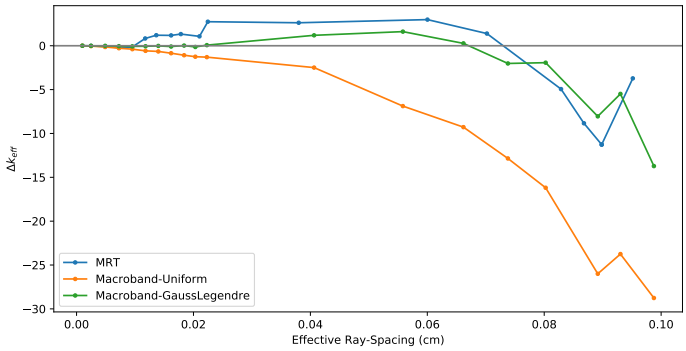

Figure 6.4: Eigenvalue errors (relative to finest ray-spacing of that ray-tracing method) for each ray-tracing method over a range of ray-spacings.

A visualization of generated rays for this pin-cell are shown in Fig. 6.6. Each of the macroband methods has obvious "clustering" effects near the small surfaces in the computational mesh, this is obvious in the azimuthal divisions in the moderator region outside the pin. This clustering is

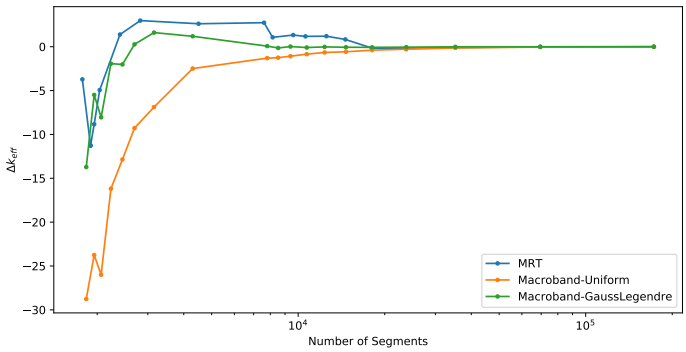

Figure 6.5: Eigenvalue errors (relative to finest ray-spacing of that ray-tracing method) for each ray-tracing method as a function of the number of track-segments.

expected, as the macroband method will guarantee rays to pass through these surfaces, unlike the MRT. Although this may not have significant effect in this case, it may when larger lattice cases are considered, particularly with respect to finely meshed strong absorbers. It is also interesting to observe that in the macroband with uniform spacing method, there seem to be concentric patterns where many rays intersect; it may be possible to remove these patterns by using a mobile-chord method within each macroband.

6.3 Future work

The main contributions of this thesis work are the improved LSMoC, the macroray ray-tracing techniques, and an improved spatial decomposition scheme, with application toward improving the efficiency of three-dimensional MoC calculations. Thus far, 2-D studies have been performed on the LSMoC with and without multiphysics [14, 17], and 3-D studies have been performed without multiphysics [9]. Future work in this thesis requires larger 2-D multiphysics calculations to be run to verify new default mesh parameters, as well as 3-D multiphysics calculations.

Work on the spatial decomposition scheme has largely been completed. Studies have been performed for 2-D transport calculations, and load-balance has been analyzed for 3-D problems [22]. The 2-D transport calculations revealed that some alignment of the spatial domains will have benefits in iteration convergence due to re-entrant flux. This indicates that for 3-D calculations, the axially and radially aligned decomposition schemes are likely to have an additional advantage not observed from load-balance results.

Finally, implementation of the macroray based MoC library is currently in progress. Several steps are still required for this implementation to be completed: calculations of current for CMFD calculations, generalization to 3-D rays, multi-pin calculations, and anisotropic scattering. Studies

should be performed on two-dimensional transport problems. A repetition of the lattice cases run in Section 6.1 should be run with each of the ray-tracing methods in 2-D calculations; this is to verify our treatment of interface conditions, as well as demonstrate the advantage in cases with strong absorbers. Additionally, as the methods are extended to three-dimensional problems, a scaling study of ray and segment requirements vs accuracy should be performed on a small problem. This study shall require investigation into the effect of directional quadrature modularization.

An approximate outline of future activities is outlined in Fig. 6.7.

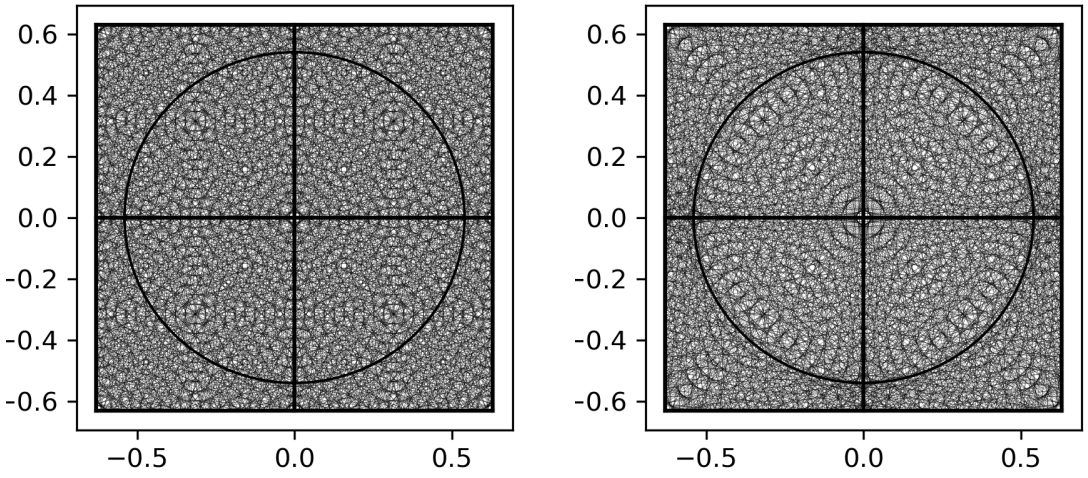

(a) MRT

(b) Macroband-Uniform

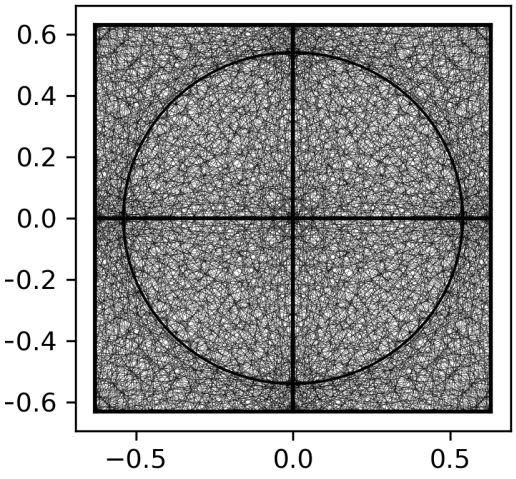

(c) Macroband-Gauss-Legendre

Figure 6.6: Visualization of generated rays for an input spacing of 0.05 cm for each ray-tracing method.

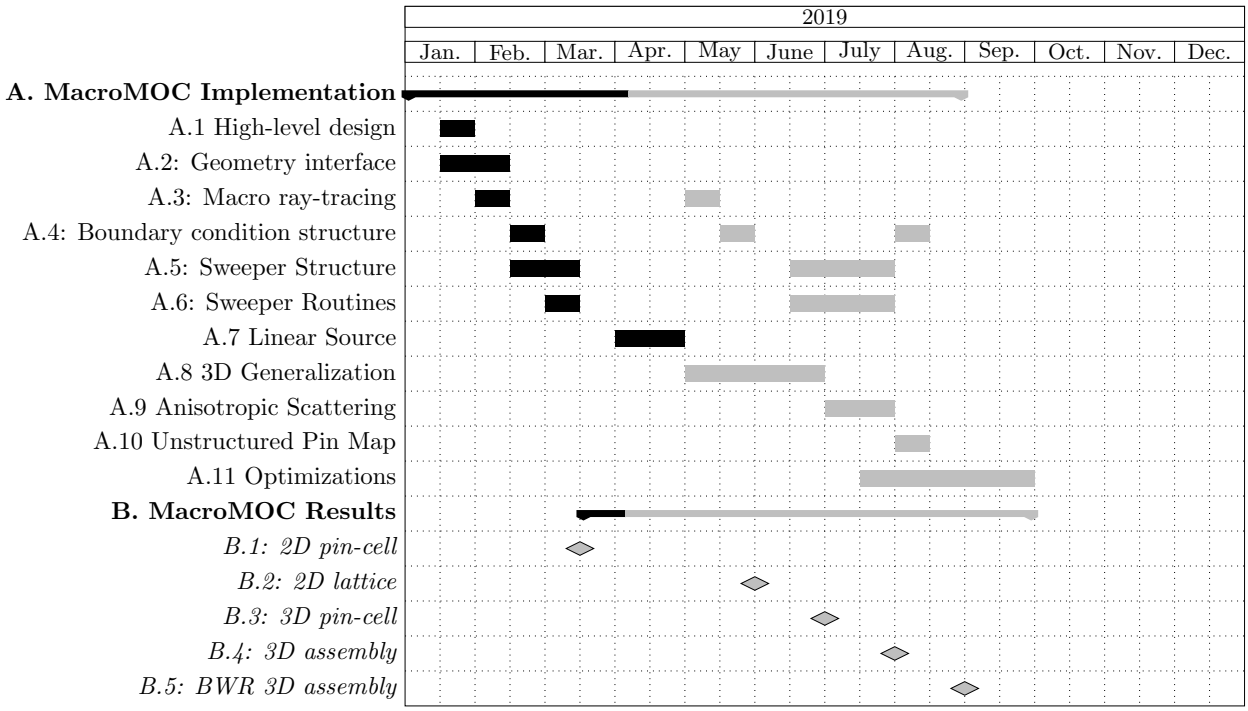

Figure 6.7: Possible plan for implementation of macroray MoC library.

Bibliography

[1] G. C. Bilodeau et al. *PDQ: An IBM-704 Code to Solve the Two-dimensional Few-group Neutron-Diffusion Equations*. Tech. rep. Bettis Plant, Westinghouse Electrice Corporation, 1957.

[2] Kord Smith and Joel D. Rhodes. "CASMO-4 Characteristic Methods for Two-Dimensional PWR and BWR Core Calculations". In: *Transactions of the American Nuclear Society*. 2000.

[3] Richard Sanchez et al. "APOLLO2 Year 2010". In: *Journal of Nuclear Engineering and Technology* 42.5 (2010), pp. 474–499.

[4] Han Gyu Joo et al. "Methods and performance of a three-dimensional whole-core transport code DeCART". In: *PHYSOR 2004*. 2004, pp. 21–34. ISBN: 0894486837. URL: http://www.scopus.com/inward/record.url?eid=2-s2.0-22344449157{\&}partnerID=tZOtx3y1.

[5] Thomas M. Evans et al. "Denovo: A New Three-Dimensional Parallel Discrete Ordinates Code in SCALE". In: *Nuclear Technology* 171.2 (2010), pp. 171–200. ISSN: 0029-5450. DOI: 10.13182/nt171-171.

[6] W. S. Yang et al. "Neutronics modeling and simulation of sharp for fast reactor analysis". In: *Nuclear Engineering and Technology* 42.5 (2010), pp. 520–545. ISSN: 17385733. DOI: 10.5516/NET.2010.42.5.520.

[7] William Boyd et al. "The OpenMOC method of characteristics neutral particle transport code". In: *Annals of Nuclear Energy* 68 (2014), pp. 43–52. ISSN: 03064549. DOI: 10.1016/j.anucene.2013.12.012.

[8] Benjamin Collins et al. "Stability and accuracy of 3D neutron transport simulations using the 2D/1D method in MPACT". In: *Journal of Computational Physics* 326 (2016), pp. 612–628. ISSN: 10902716. DOI: 10.1016/j.jcp.2016.08.022.

[9] Geoffrey Alexander Gunow. "Full Core 3D Neutron Transport Simulation Using the Method of Characteristics with Linear Sources". Doctoral. Massachusetts Institute of Technology, 2018.

[10] J.R. Askew. *A Characteristics Formulation of the Neutron Transport Equation in Complicated Geometries*. 1972.

[11] Brendan Matthew Kochunas. "A Hybrid Parallel Algorithm for the 3-D Method of Characteristics Solution of the Boltzmann Transport Equation on High Performance Compute Clusters". Doctoral. University of Michigan, 2013, pp. 1–194.

[12] Daniele Sciannandrone, Simone Santandrea, and Richard Sanchez. "Optimized tracking strategies for step MOC calculations in extruded 3D axial geometries". In: *Annals of Nuclear Energy* 87 (2016), pp. 49–60. ISSN: 18732100. DOI: 10.1016/j.anucene.2015.05.014.

[13] Geoffrey Gunow et al. "Reducing 3D MOC Storage Requirements with Axial On- the-fly Ray Tracing". In: *Physics of Reactors 2016, PHYSOR 2016: Unifying Theory and Experiments in the 21st Century*. Sun Valley: American Nuclear Society, 2016. URL: http://hdl.handle.net/1721.1/109864{\%}0ACreative.

[14] Rodolfo M. Ferrer and Joel D. Rhodes. "A Linear Source Approximation Scheme for the Method of Characteristics". In: *Nuclear Science and Engineering* 182.2 (2016), pp. 151–165. ISSN: 0029-5639. DOI: 10.13182/NSE15-6.

[15] Rodolfo M. Ferrer and Joel D. Rhodes. "The linear source approximation and particle conservation in the Method of Characteristics for isotropic and anisotropic sources". In: *Annals of Nuclear Energy* 115 (2018), pp. 209–219. ISSN: 03064549. DOI: 10.1016/j.anucene.2018.01.023.

[16] Andrew Fitzgerald and Brendan Kochunas. "Fast Exponential Function Approximations for the Method of Characteristics with Linear Source". In: *Transactions of the American Nuclear Society*. Orlando, USA, 2018, pp. 645–648.

[17] Andrew Fitzgerald, Brendan Kochunas, and Thomas Downar. "Improved Formulation of the Method of Characteristics with Linear Source for 2D/1D and Multiphysics Calculations". In: *M&C 2019*. Portland.

[18] Eduardo A. Villarino et al. "HELIOS: Angularly Dependent Collision Probabilities". In: *Nuclear Science and Engineering* 112.1 (1992), pp. 16–31. ISSN: 0029-5639. DOI: 10.13182/NSE112-16.

[19] Akio Yamamoto et al. "Non-Equidistant Ray Tracing for the Method of Characteristics". In: *M&C 2005* (2005), pp. 1–10.

[20] François Févotte, Simone Santandrea, and Richard Sanchez. "Advanced Transverse Integration for the Method of Characteristics". In: *M&C 2007*. 2007, pp. 1–12. ISBN: 0894480596.

[21] Andrew Fitzgerald et al. “Automated Decomposition of a Structured Grid”. In: *Transactions of the American Nuclear Society*. Vol. 117. Washington D.C., 2017, pp. 731–734.

[22] Andrew Fitzgerald et al. “Spatial Decomposition of Structured Grids for Nuclear Reactor Simulations”. In: *Annals of Nuclear Energy* ().

[23] D. A. Brown et al. “ENDF/B-VIII.0: The 8th Major Release of the Nuclear Reaction Data Library with CIELO-project Cross Sections, New Standards and Thermal Scattering Data”. In: *Nuclear Data Sheets* 148 (2018), pp. 1–142. ISSN: 00903752. DOI: 10.1016/j.nds.2018.02.001.

[24] Dave Knott and Akio Yamamoto. “Lattice Physics Computations”. In: *Handbook of Nuclear Engineering* (2010), pp. 913–1239. DOI: 10.1007/978-0-387-98149-9_9.

[25] Akio Yamamoto et al. “Derivation of optimum polar angle quadrature set for the method of characteristics based on approximation error for the bickley function”. In: *Journal of Nuclear Science and Technology* 44.2 (2007), pp. 129–136. ISSN: 00223131. DOI: 10.1080/18811248.2007.9711266.

[26] M.J. Halsall. “CACTUS, a characteristics solution to the neutron transport equations in complicated geometries”. In: *Transactions of the American Nuclear Society*. 1980. URL: https://inis.iaea.org/search/search.aspx?orig{_}q=RN:12592444.

[27] Alain Hébert. “Multigroup Neutron Transport and Diffusion Computations”. In: *Handbook of Nuclear Engineering* (2010), pp. 751–911. DOI: 10.1007/978-0-387-98149-9_8.

[28] Ser Gi Hong and Nam Zin Cho. “Method of Characteristic Direction Probabilities for Heterogeneous Lattice Calculation”. In: *Nuclear Science and Engineering* 132.1 (2017), pp. 65–77. ISSN: 0029-5639. DOI: 10.13182/nse99-a2049.

[29] Zhouyu Liu et al. “Theory and analysis of accuracy for the method of characteristics direction probabilities with boundary averaging”. In: *Annals of Nuclear Energy* 77 (2015), pp. 212–222. ISSN: 0306-4549. DOI: 10.1016/J.ANUCENE.2014.11.016.

[30] Alain Hébert. “Acceleration of step and linear discontinuous schemes for the method of characteristics in DRAGON5”. In: *Nuclear Engineering and Technology* 49.6 (2017), pp. 1135–1142. ISSN: 2234358X. DOI: 10.1016/j.net.2017.07.004.

[31] K.S. Smith and J.D. Rhodes III. “Full-Core, 2-D, LWR Core Calculations with CASMO-4E”. In: *Physor* 1 (2002), pp. 1–13.

[32] Kord S. Smith. “Nodal method storage reduction by nonlinear iteration”. In: *Transactions of the American Nuclear Society*. Vol. 44. 1983, pp. 265–266.

[33] Dmitriy Y Anistratov. “Multi-level nonlinear diffusion acceleration method for multigroup transport k-eigenvalue problems”. In: *International Conference on Mathematics and Computational Methods Applied to Nuclear Science and Engineering, Rio de Janeiro, RJ, Brazil, May* 2 (2011), pp. 8–12.

[34] Nam Zin Cho. “Fusion of method of characteristics and nodal method for 3-D whole-core transport calculation”. In: *American Nuclear Society*. 2002, p. 322.

[35] Ang Zhu et al. “An optimally diffusive Coarse Mesh Finite Difference method to accelerate neutron transport calculations”. In: *Annals of Nuclear Energy* 95 (2016), pp. 116–124. ISSN: 18732100. DOI: 10.1016/j.anucene.2016.05.004.

[36] Brendan Kochunas, Andrew Fitzgerald, and Edward Larsen. “Fourier analysis of iteration schemes for k-eigenvalue transport problems with flux-dependent cross sections”. In: *Journal of Computational Physics* 345 (2017), pp. 294–307. ISSN: 10902716. DOI: 10.1016/j.jcp.2017.05.028.

[37] Ben C. Yee, Brendan Kochunas, and Edward W. Larsen. “A Multilevel in Space and Energy Solver for 3-D Multigroup Diffusion and Coarse-Mesh Finite Difference Eigenvalue Problems”. In: *Nuclear Science and Engineering* 00.00 (2019), pp. 1–24. ISSN: 0029-5639. DOI: 10.1080/00295639.2018.1562777.

[38] Ser Gi Hong and Nam Zin Cho. “CRX: A code for Rectangular and Hexagonal Lattices Based on the Method of Characteristics”. In: *Annals of Nuclear Energy* 25.97 (1998), pp. 547–565.

[39] Shinya Kosaka and Etsuro Saji. “Transport theory calculation for a heterogeneous multi-assembly problem by characteristics method with direct neutron path linking technique”. In: *Journal of Nuclear Science and Technology* 37.12 (2000), pp. 1015–1023. ISSN: 00223131. DOI: 10.1080/18811248.2000.9714987.

[40] Naoki Sugimura et al. “Neutron Transport Models of AEGIS: An Advanced Next-Generation Neutronics Design System”. In: *Nuclear Science and Engineering* 155.2 (2006), pp. 276–289. ISSN: 0029-5639. DOI: 10.13182/nse155-276.

[41] Emiliano Masiello, Richard Sanchez, and Igor Zmijarevic. “New Numerical Solution with the Method of Short Characteristics for 2-D Heterogeneous Cartesian Cells in the APOLLO2 Code: Numerical Analysis and Tests”. In: *Nuclear Science and Engineering* 161.3 (2008), pp. 257–278. ISSN: 0029-5639. DOI: 10.13182/nse161-257.

[42] R. Le Tellier and A. Hébert. “Anisotropy and Particle Conservation for Trajectory-Based Deterministic Methods”. In: *Nuclear Science and Engineering* 158.1 (2008), pp. 28–39. ISSN: 0029-5639. DOI: 10.13182/NSE08-A2736.

[43] Akio YAMAMOTO, Yasunori KITAMURA, and Yoshihiro YAMANE. “Simplified Treatments of Anisotropic Scattering in LWR Core Calculations”. In: *Journal of Nuclear Science and Technology* 45.3 (2008), pp. 217–229. ISSN: 0022-3131. DOI: 10.1080/18811248.2008.9711430.

[44] Petko Petkov, Toshikazu Takeda, and Takamasa Mori. “Comparison of the Flat and Linear Source Variants of the Method of Characteristics”. In: *Annals of Nuclear Energy* 26.10 (1999), pp. 935–942. ISSN: 03064549. DOI: 10.1016/S0306-4549(98)00109-1.

[45] Edward W. Larsen and Warren F. Miller. “Convergence Rates of Spatial Difference Equations for the Discrete-Ordinates Neutron Transport Equations in Slab Geometry”. In: *Nuclear Science and Engineering* 73.1 (1980), pp. 76–83. ISSN: 0029-5639. DOI: 10.13182/nse80-3.

[46] M. J. Halsall. “Neutron Transport in WIMS by the Characteristics Methods”. In: *Transactions of the American Nuclear Society1*. 1993, pp. 454–455.

[47] Chuntao Tang and Shaohong Zhang. “Development and verification of an MOC code employing assembly modular ray tracing and efficient acceleration techniques”. In: *Annals of Nuclear Energy* 36.8 (2009), pp. 1013–1020. ISSN: 03064549. DOI: 10.1016/j.anucene.2009.06.007.

[48] Petko T. Petkov and Toshikazu Takeda. “Transport calculations of MOX and UO2 pin cells by the method of characteristics”. In: *Journal of Nuclear Science and Technology* 35.12 (1998), pp. 874–885. ISSN: 00223131. DOI: 10.1080/18811248.1998.9733960.

[49] C Rabiti et al. “Quasi Linear Representation of the Isotropic Scattering Source for the Method of Characteristics”. In: *International Conference on Mathematics, Computational Methods & Reactor Physics* January (2009), pp. 3–7.

[50] S Santandrea and R Sanchez. “POSITIVE LINEAR AND NONLINEAR SURFACE CHARACTERISTIC SCHEMES FOR THE NEUTRON TRANSPORT EQUATION IN UNSTRUCTURED GEOMETRIES”. In: *Physor*. 2002.

[51] Simone Santandrea, Richard Sanchez, and Pietro Mosca. “A linear surface characteristics approximation for neutron transport in unstructured meshes”. In: *Nuclear Science and Engineering* 160.1 (2008), pp. 23–40. ISSN: 00295639. DOI: 10.13182/NSE07-69.

[52] Romain Le Tellier and Alain Hébert. “On the integration scheme along a trajectory for the characteristics method”. In: *Annals of Nuclear Energy* 33.14-15 (2006), pp. 1260–1269. ISSN: 03064549. DOI: 10.1016/j.anucene.2006.07.010.

[53] Alain Hébert. “High-Order Linear Discontinuous and Diamond Differencing Schemes Along Cyclic Characteristics”. In: *Nuclear Science and Engineering* 184.4 (2016), pp. 591–603. ISSN: 0029-5639. DOI: 10.13182/nse16-82.

[54] Emiliano Masiello, Roberto Clemente, and Simone Santandrea. “High-Order Method of Characteristics for 2-D Unstructured Meshes”. In: *International Conference on Mathematics, Computational Methods & Reactor Physics* June 2015 (2009). URL: http://mathematicsandcomputation.cowhosting.net/MC09/pdfs/202865.pdf{\%}5Cnpapers3://publication/uuid/217E92CC-587D-4349-843B-58B5693D625C.

[55] X. M. Chai, K. Wang, and D Yao. “The linear source approximation in three dimension characteristics method”. In: *International Conference on Mathematics, Computational Methods \& Reactor Physics (M\&C 2009)* February (2009), pp. 1–14.

[56] W. L. Filippone, S. Woolf, and R. J. Lavigne. “Particle Transport Calculations with the Method of Streaming Rays”. In: *Nuclear Science and Engineering* 77.2 (1980), pp. 119–136. ISSN: 0029-5639. DOI: 10.13182/nse81-a21346.

[57] G. J. Wu and R. Roy. “A new characteristics algorithm for 3D transport calculations”. In: *Annals of Nuclear Energy* 30.1 (2003), pp. 1–16. ISSN: 03064549. DOI: 10.1016/S0306-4549(02)00046-4.

[58] Yeon Sang Jung and Han Gyu Joo. “Decoupled Planar MOC Solution for Dynamic Group Constant Generation in Direct Three-Dimensional Core”. In: *M&C 2009* (2009).

[59] Franck Gabriel et al. “APOLLO3: CEA/DEN DETERMINISTIC MULTI-PURPOSE CODE FOR REACTOR PHYSICS ANALYSIS”. In: May 2016. 2016.

[60] MPACT Team. *MPACT Theory Manual v2.2.0*. Tech. rep. Consortium for Advanced Simulation of Light Water Reactors, 2016.

[61] Alain Hébert. “Acceleration of Step and Linear Discontinuous Schemes for the Method of Characteristics in DRAGON5”. In: *M&C 2017*. Jeju, Korea, 2017.

[62] Akio Yamamoto. “Reduction in spatial discretization error in the method of characteristics by using the mobile-chord ray tracing method”. In: *Annals of Nuclear Energy* 35.5 (2008), pp. 783–789. ISSN: 03064549. DOI: 10.1016/j.anucene.2007.09.018.

[63] John R. Tramm et al. “A task-based parallelism and vectorized approach to 3D Method of Characteristics (MOC) reactor simulation for high performance computing architectures”. In: *Computer Physics Communications* 202 (2016), pp. 141–150. ISSN: 00104655. DOI: 10.1016/j.cpc.2016.01.007.

[64] Akio Yamamoto et al. “GENESIS: A Three-Dimensional Heterogeneous Transport Solver Based on the Legendre Polynomial Expansion of Angular Flux Method”. In: *Nuclear Science and Engineering* 49.6 (2017), pp. 1143–1156. ISSN: 2234358X. DOI: 10.1016/j.net.2017.06.016.

[65] Laurent Graziano et al. “Polynomial Characteristics Method for Neutron Transport in 3D extruded geometries”. In: *M&C 2017*. Jeju, Korea, 2017.

[66] Geoffrey Gunow et al. “Accuracy and Performance of 3D MOC for Full-Core PWR Problems”. In: *M&C 2017*. Jeju, Korea, 2017.

[67] S. Shaner et al. “Theoretical analysis of track generation in 3D method of characteristics”. In: *Mathematics and Computations, Supercomputing in Nuclear Applications and Monte Carlo International Conference, M&C+SNA+MC 2015* 4.Mc (2015), pp. 2667–2681.

[68] Akinori Giho et al. “Development of Axially Simplified Method of Characteristics in Three-Dimensional Geometry”. In: *Journal of Nuclear Science and Technology* 45.10 (2008), pp. 985–996. ISSN: 0022-3131. DOI: 10.3327/jnst.45.985.

[69] Akio Yamamoto et al. “Angular Dependent Transmission Probability Method for Fast Reactor Core Transport Analysis”. In: *Transactions of the American Nuclear Society*. 2015, pp. 736–738.

[70] Ulrich Elsner. *Graph partitioning A Survey*. Tech. rep. Technische Universitat Chemnitz, 1997, p. 52. URL: http://citeseerx.ist.psu.edu/viewdoc/summary?doi=10.1.1.54.2060.

[71] Y.F. Yao and B.E. Richards. “Parallel CFD Computation on Unstructured Grids”. In: *Parallel Computational Fluid Dynamics*. Elsevier, 1998, pp. 289–296. DOI: 10.1016/B978-044482849-1/50035-X.

[72] Shane Stimpson and Benjamin Collins. “Flexible Spatial Partitions in MPACT Through Module-Based Data Passing”. In: *Transactions of the American Nuclear Society*. Vol. 116. San Francisco, 2017, pp. 654–657.

[73] G. M. Morton. *A computer Oriented Geodetic Data Base; and a New Technique in File Sequencing*. Tech. rep. Ottawa, Canada: IBM Ltd., 1966.

[74] George Karypis and Vipin Kumar. “A fast and high quality multilevel scheme for partitioning irregular graphs”. In: *SIAM Journal on Scientific Computing* 20.1 (1998), pp. 359–392.

[75] Alex Pothen, Horst D. Simon, and Kang-Pu Paul Liu. “Partitioning Sparse Matrices with Eigenvectors of Graphs”. In: *SIAM Journal on Matrix Analysis and Applications* 11.3 (1989), pp. 430–452.

[76] H. D. Simon. “Partitioning of unstructured problems for parallel processing”. In: *Computing Systems in Engineering* 2.2-3 (1991), pp. 135–148. ISSN: 09560521. DOI: 10.1016/0956-0521(91)90014-V.

[77] Daniel A. Spielman and Shang Hua Teng. “Spectral partitioning works: Planar graphs and finite element meshes”. In: *Linear Algebra and Its Applications* 421.2-3 SPEC. ISS. (2007), pp. 284–305. ISSN: 00243795. DOI: 10.1016/j.laa.2006.07.020.

[78] Shang Hsien Hsieh, Glaucio H. Paulino, and John F. Abel. “Recursive spectral algorithms for automatic domain partitioning in parallel finite element analysis”. In: *Computer Methods in Applied Mechanics and Engineering* 121.1-4 (1995), pp. 137–162. ISSN: 00457825. DOI: 10.1016/0045-7825(94)00704-Q.

[79] Miroslav Fiedler. “Algebraic Connectivity of Graphs”. In: *Czechoslovak Mathematical Journal* 23.2 (1973), pp. 298–305.

[80] N. Floros et al. “Comparative efficiencies of domain decompositions”. In: *Parallel Computing* 21.11 (1995), pp. 1823–1835. ISSN: 01678191. DOI: 10.1016/0167-8191(95)00031-7.

[81] Charbel Farhat. “A simple and efficient automatic fem domain decomposer”. In: *Computers and Structures* 28.5 (1988), pp. 579–602. ISSN: 00457949. DOI: 10.1016/0045-7949(88)90004-1.

[82] M A Nasra and D T Nguyen. “An algorithm for domain decomposition in finite element analysis”. In: *Computers & Structures* 39.3/4 (1991), pp. 277–289.

[83] K Lassmann et al. “The radial distribution of plutonium in high burnup UO2 fuels”. In: *Journal of Nuclear Materials* 208.3 (1994), pp. 223–231. ISSN: 00223115. DOI: 10.1016/0022-3115(94)90331-X.

[84] A. T. Godfrey. *VERA Core Physics Benchmark Progression Problem Specifications*. Tech. rep. 4. 2014, pp. 1–173. URL: https://www.casl.gov/sites/default/files/docs/CASL-U-2012-0131-004.pdf.

[85] H. Carter Edwards, Christian R. Trott, and Daniel Sunderland. “Kokkos: Enabling many-core performance portability through polymorphic memory access patterns”. In: *Journal of Parallel and Distributed Computing* 74.12 (2014), pp. 3202–3216. ISSN: 07437315. DOI: 10.1016/j.jpdc.2014.07.003.